The End of the Rhodium:
Synthesis, Characterization, and Redox Chemistry of Manganese and Rhodium Complexes Supported by Unorthodox Diimine Ligands

Thesis by:

Jonah Philip Stiel

Submitted to the Faculty of the Department of Chemistry in Partial Fulfillment of the Requirements for Departmental Honors in Chemistry

Lawrence, Kansas
May 2022

Table of Contents

Acknowledgements

I have always been a firm believer that change tends to happen gradually. I have been asked many times through applications, thought experiments, ice breakers, and more about defining moments in my life. Moments when I suddenly realized something, moments when I overcame a challenge, or moments that changed the trajectory of my life. The truth is that there have not been so many moments in my life that I would describe as causing radical change. Change tends to happen gradually.

It is with that in mind that I am floored by the profound impact that meeting Professor James Blakemore has had on my life. James took a chance on me when I was just a high school student. He was busy setting up a research laboratory, but he took me under his wing and let me shadow in his lab the summer after my junior year. His generosity then, and his mentorship in the years following have forever changed the course of my life. James is an exceptional scientist, a natural leader, a talented teacher, and a true mensch. It has been my distinct privilege to be his student, and I could not have gotten to this point without him. As I leave to begin my graduate studies, I am reminded that it was James who first made me realize graduate school was an option for me. Thank you, James, for everything.

Another person whose help has been absolutely invaluable is my graduate student mentor, Dr. Wade Henke. As far back as that first summer in high school when he was just an undergraduate, Wade has been my in-lab mentor in the Blakemore Group. I derive great joy and satisfaction from chemical synthesis, and I will always be grateful to Wade for showing me how it is done. Wade is a tremendous synthetic chemist, and I have been incredibly lucky to have the opportunity to learn from him. On top of teaching me the ropes of chemical synthesis, Wade taught

me how to think like a lab safety officer. The entire Blakemore Group has a strong safety culture, for which I have always been grateful. Yet, I am particularly grateful to Wade for firmly implanting a safety-first mindset within me. For a synthetic chemist, it is a skill that can quite literally save your life.

Outside of the lab, Wade has taught me a great deal about how to be a good scientific writer, to make impactful presentations, to defend your conclusions with data, and more. It is thanks to Wade that I hope to have the opportunity to mentor an undergraduate or undergraduates of my own during my time in graduate school. Wade, you have been a compassionate, patient, and generous mentor. Over the past six years you have challenged me to become a better scientist, and I have become a better scientist because of it. Thank you.

I am additionally grateful to my other current and former co-workers in the Blakemore Group: Erin Arnold, Emily Boyd, Emma Cosner, Dr. Chelsea Comadoll, Davis "Not Thomas" Curry, Claire Dopp, Alex Ervin, Riddhi Golwankar, Joseph Karnes, Shaun Kelsey, Tyler Kerr, Dr. Amit Kumar, Dr. Julie Leseberg, Prof. Davide Lionetti, Emily Mikeska, Will Moore, Christian Nilles, Dr. Yun Peng, Keaton Prather, and Dr. David Sconyers. Research has been a huge part of my undergraduate career, and each and every one of these people has been a part of making undergraduate research the unforgettable experience that it has been for me. Their friendship, advice, help, and again friendship deserve so much more recognition than a mention in my acknowledgements can afford. Thank you all.

Two of my current and former lab mates who deserve special thanks are Will Moore and Emma Cosner. Will was the mastermind who first envisioned the mono-substituted bipyridine project described in the second chapter of my thesis. He laid the groundwork, developed the

synthetic pathway, and first demonstrated the viability of the project. Thank you, Will, for allowing me to finish the fantastic project that you started and contributed so much work towards. While Emma has not let me finish any of her projects, she has become one of my closest friends in the time since we first started working together. Her continual friendship and support mean the world to me. Between working in the Blakemore Group, being on the Chemistry Club's Executive Board, scholarship applications, and graduate school applications we have been through a lot together. It has been a pleasure to travel this path side-by-side with a friend as true as Emma. I am thrilled that we are going to graduate school close enough together to stay connected.

My committee is composed of some of my greatest supporters and mentors at KU. First and foremost being my outstanding research advisor, Prof. James Blakemore, who was mentioned above. I also want to extend my great thanks to Prof. Misha Barybin and Prof. Jon Tunge. Although I missed out on taking Prof. Barybin's Honors General Chemistry class, I had the great privilege to take his course on Nuclear Magnetic Resonance (NMR) Spectroscopy. In addition to teaching me a great deal about NMR, Prof. Barybin has been a fantastic sounding board at times of indecision and a veritable wellspring of good advice. My third committee member, Prof. Jon Tunge, welcomed me into his Honors Organic Chemistry II class despite the fact that I was a freshman and not yet a member of the University Honors Program. Prof. Tunge's class opened my eyes to a whole new world of chemistry that I immediately fell in love with. Had I not already been introduced to the exciting work of the Blakemore Group, I may have ended up as an organic chemist as a result. All three members of my committee have had central roles in my undergraduate chemical education and in fostering my growth as a young professional in the chemical sciences. Through their teaching, mentorship, and encouragement, I have accomplished more during my undergraduate career than I ever imagined possible.

Someone who has not been involved directly in my pursuit of science yet is deserving of great thanks is Dr. Kelly Sartorius. Taking her Honors seminar was the best possible introduction to the University Honors Program I could have had. In the years following, she has been instrumental in providing advice and feedback on countless essays I have written for scholarships and applications. Written communication is an invaluable skill in any field and arguably of even greater importance in the sciences, where the abundance of technical detail can detract from clarity. Dr. Sartorius has been a primary driving force behind bringing my writing ability to the collegiate level. She has also been a true friend and treated me like a member of her own family, even going so far as to welcome me to her family's Thanksgiving dinner when I had no family left in town to celebrate with. The impact of her kindness cannot be overstated.

Finally, I would like to express my sincere gratitude to my family. I am mindful every day of how lucky I am to be part of a family that loves me and helps me to reach my goals. Growing up, I was never told what I could or could not become. There was no expectation that I follow either of my parents' career paths. When I showed interest in scientific reading material as a kid, my parents made sure to get more books to suit my interests. When I prematurely decided in the 2nd grade that I wanted to become a rainforest conservationist, I was encouraged to pursue what was important to me rather than being told I should stick to a more conventional career. And in high school, when I decided that I wanted to consider chemistry as a potential career, my parents helped me formulate a plan to see if chemistry research was something I might enjoy doing. That plan led me to reach out to James, and the rest is history. My family gifted me the freedom to discover who I am, what is important to me, and what career would be fulfilling to me. For that, as well as for 23 years of unwavering love and support, I am eternally grateful.

To my family,

My dad, who taught me there is no adversity in life which cannot be overcome with a smile, and no circumstance which justifies compromising one's principles.

My mom, who is too selfless to rest and too humble to notice that she leads entire communities through the example set by her strength of ruach.

My brother, who is my oldest friend and role model. Little brothers always look up to their older brothers, and I am blessed to have an older brother deserving of admiration.

My sister-in-law, whose boundless kindness and generosity is slowly filling her house with diabetic cats.

My cats Atticus and Scout, for alternately keeping me sane and driving me up the wall.

Abstract

Economical storage of the large quantities of energy that could be generated by intermittent renewable sources, such as solar and wind, remains one of the largest unmet technical challenges hindering the widespread adoption of such technologies. Storing renewable energy in chemical bonds by means of molecular electrocatalysis represents a promising potential solution to this pressing issue. The 2,2′-bipyridyl (bpy) moiety is ubiquitous among the current generation of fuel production molecular electrocatalysts, yet a fundamental understanding of the properties which make it exceptionally attractive for enabling redox catalysis is lacking. In this thesis, model systems supported by unconventional analogues of bpy were investigated in order to elucidate the influence of steric and electronic effects on catalyst candidates supported by bpy-type ligands. In Chapter 2, the synthesis and characterization of manganese and ruthenium complexes supported by 4,5-diazafluorene and 9,9′-dimethyl-4,5-diazafluorene are discussed. These ligands were found to enforce wider bite angles and act as weaker sigma-donors in the complexes than bpy in analogous species. In Chapter 3, our work focusing on half-sandwich rhodium complexes supported by non-symmetrically mono-substituted bpy ligands bearing either a chloro (−Cl) or nitro ($-NO_2$) substituent is detailed. Non-symmetric mono-substitution of the bpy ligand system was found to be an effective strategy for engendering new redox behavior at the metal center. Furthermore, the redox properties of the complexes supported by the mono-substituted bpy ligands were found to be intermediate between those of the parent complex supported by bpy and the symmetrically di-substituted complex supported by 4,4′-dinitro-2,2′-bipyridyl. Taken together, the findings reported in this thesis highlight the power of seemingly subtle ligand modifications in facilitating new redox chemistry with transition metal complexes.

Chapter 1: Motivations

Anthropogenic climate change driven by greenhouse gas emission is an issue with far-reaching consequences for all members of society. Warming temperatures, increasingly destructive weather events, rising oceans, forest fires, food shortages, and extinction events have all been linked to rising concentrations of greenhouse gases in the Earth's atmosphere.

One of the most significant greenhouse gases is carbon dioxide (CO_2), a product of complete combustion of the carbon-containing fossil fuels that are currently used to produce over 84% of the energy used for humanity's activities on the planet.[1] Displacing hundreds of billions of metric tons of carbon from the Earth's crust to the atmosphere has profoundly disrupted Earth's natural carbon cycle, which is a key part of the planet's natural climate regulation.[2]

In search of less environmentally destructive power sources for society, attention has turned to hydrogen as a potential replacement for fossil fuels. However, despite the hype surrounding hydrogen economies, a successful hydrogen economy will still need to ameliorate extant atmospheric carbon dioxide. Given the prodigious quantity of carbon dioxide already released into the atmosphere and the amount that will be released in the time it will take for humanity to transition away from fossil fuel sources, it is a distinct possibility that atmospheric carbon capture and sequestration will be necessary in order to prevent the worst effects of climate change. Additionally, many organic commodities cannot be replaced. Pharmaceuticals, plastics, and solvents that are currently made from petroleum products do not necessarily have suitable non-petroleum-derived organic replacements. In order to offset the effects of continuing to produce organic commodities on industrially-relevant scales, it will likely be necessary to form a closed, artificial carbon cycle. Already, this endeavor and the social conflict surrounding it have proven to be defining characteristics of the 21st century.

One of the primary hurdles that must be overcome in order to create an economically viable artificial carbon cycle is developing a cost-effective means of reducing CO_2. Catalysts driven by electricity, also known as electrocatalysts, constitute a promising means of generating fuels and carbon-based chemical feedstocks from CO_2. Electrocatalysis facilitates the conversion of CO_2 or H_2O to fuels by means of electricity generated from renewable sources such as solar and wind.

The primary barrier to the implementation of electrocatalysts in fuel production is the difficulty in tuning the energetics and selectivity of a given candidate catalyst.[3] Catalysts exist which facilitate the reduction of CO_2 and H_2O to useful fuels such as carbon monoxide (CO) and hydrogen (H_2). However, the current generation of fuel production catalysts have two major problems: they require large overpotentials and lack selectivity. An overpotential is the difference between the voltage thermodynamically required to perform a process and the experimentally required voltage. Essentially, large overpotentials lead to energy being wasted as heat. The second problem, lack of selectivity, arises from the fact that the electrons and protons used in the conversion of CO_2 to CO are practically the same as those used in the conversion of H_2O to H_2. Due to the high stability of CO_2, strong thermodynamic driving forces are required to facilitate conversion to reduced products. Under such forcing conditions, mitigating unwanted side reactions such as H_2 production is challenging. For fuel production catalysts to be industrially useful they must be selective.

My work in the Blakemore Group over the past six years has been centered around this important concept of modulating the energetics and selectivity of organometallic candidate catalysts. Despite the longstanding interest in this topic within the field of chemistry, relatively little is known about how to design a catalyst for a given purpose. Trial and error still play

significant roles in catalyst development. Given that the phase space of possible chemical structures is nearly limitless, the trial-and-error approach is inefficient for developing chemical solutions to problems. Our group seeks to circumvent the need for a trial-and-error approach by developing a deeper understanding of the fundamental factors and mechanisms driving reactivity in organometallic complexes. By developing structure-function models, it may be possible to better understand how to design organometallic complexes for a given purpose, such as CO_2 reduction catalysis.

In particular, my research with the Blakemore Group has sought to investigate the impact of ligand modification on metal complexes supported by bidentate diimine ligands. In this thesis, efforts to use analogues of the ubiquitous 2,2´-bipyridyl (bpy) ligand to engender new redox behavior in organometallic model systems relevant to the field of electrocatalytic fuel production are detailed.

In Chapter 2, the synthesis and characterization of manganese and ruthenium complexes supported by 4,5-diazafluorene and 9,9´-dimethyl-4,5-diazafluorene are discussed. Diazafluorene-type ligands could be of great utility in the field because of their structural similarities to bpy type ligands. Both diazafluorene and bpy are diimine systems containing two $6e^-$ aromatic rings and tend to bind to metals in a bidentate fashion. On the other hand, diazafluorene-type ligands contain a methylene bridge that enforces a wider bite angle at the metal center compared to bpy-type ligands. Given the structural similarities between bpy and diazafluorene ligands, comparison of metal complexes supported by these ligand platforms provides especially useful insight on the relationship between chelate angle and the redox properties of diimine metal complexes.

In Chapter 3, our work focusing on half sandwich rhodium complexes supported by non-symmetrically mono-substituted bpy ligands bearing either a chloro (−Cl) or nitro ($-NO_2$) substituent is detailed. Considerable prior work has been performed with symmetrically di-substituted bpy complexes; di-substitution of bpy ligands has become well established as an effective means of modulating the redox properties of the resulting metal complexes. Through the work described in Chapter 3, we sought to determine whether non-symmetrically mono-substituted bpy ligands could similarly be utilized to tune the redox properties of metal complexes, and whether mono-substitution could enable more delicate control than di-substitution. Fortunately, we found that these tuning effects are indeed achievable, and that even mono-substitution of the bpy core, particularly with a nitro group, can drive quite significant changes in the redox chemistry accessible to systems of this general type.

Chapter 2: 4,5-Diazafluorene and 9,9´-Dimethyl-4,5-Diazafluorene as Ligands Supporting Redox-Active Mn and Ru Complexes

This chapter is adapted from two published manuscripts:

Henke, W.C., Hopkins, J.A., Anderson, M.L., Stiel, J.P., Day, V.W., and Blakemore, J.D.* 4,5-Diazafluorene and 9,9´-Dimethyl-4,5-Diazafluorene as Ligands Supporting Redox-Active Mn and Ru Complexes, *Molecules*, **2020**, *25*, 3189; doi: 10.3390/molecules25143189.

and

Henke, W.C., Stiel, J.P., Day, V.W., and Blakemore, J.D.* Evidence for Charge Delocalization in Diazafluorene Ligands Supporting Low-Valent [Cp*Rh] Complexes, *Chem. Eur. J.*, **2022**, *28*, e202200292; doi: 10.1002/chem.202103970.

Abstract

4,5-diazafluorene (daf) and 9,9´-dimethyl-4,5-diazafluorene (Me_2daf) are structurally similar to the important ligand 2,2´-bipyridine (bpy), but significantly less is known about the redox and spectroscopic properties of metal complexes containing Me_2daf as a ligand than those containing bpy. New complexes $Mn(CO)_3Br$(daf) (**2**), $Mn(CO)_3Br$(Me_2daf) (**3**), and $[Ru(Me_2daf)_3](PF_6)_2$ (**5**) have been prepared and fully characterized to understand the influence of the Me_2daf framework on their chemical and electrochemical properties. Structural data for **2**, **3**, and **5** from single-crystal X-ray diffraction analysis reveal a distinctive widening of the daf and Me_2daf chelate angles in comparison to the analogous $Mn(CO)_3$(bpy)Br (**1**) and $[Ru(bpy)_3]^{2+}$ (**4**) complexes. Electronic absorption data for these complexes confirm the electronic similarity of daf, Me_2daf, and bpy, as spectra are dominated in each case by metal-to-ligand charge transfer bands in the visible region. However, the electrochemical properties of **2**, **3**, and **5** reveal that the redox-active Me_2daf frameworks in **3** and **5** undergo reduction at slightly more negative potentials than the bpy ligands in **1** and **4**. Taken together, the results indicate that Me_2daf could be useful for preparation of a variety of new redox-active compounds, as it retains the useful redox-active nature of bpy but lacks the acidic, benzylic C–H bonds that can induce secondary reactivity in complexes bearing daf.

Introduction

2,2´-bipyridyl (bpy) is among the most ubiquitous ligands in inorganic and organometallic chemistry. As a chelating ligand, bpy often binds to transition metals in a bidentate (κ^2) mode and can support a variety of compounds with useful photophysical, redox, and/or catalytic

properties.[4,5,6,7,8,9,10] Metal complexes and catalysts bearing bpy-type ligands can be tuned by appending electron-donating groups (EDG) and electron-withdrawing groups (EWG) to the bpy ligand; such groups primarily modulate the π-accepting ability of the conjugated framework and, to a lesser extent, the σ-donating ability of the nitrogen donor atoms. For example, we have recently used 4,4´-disubstituted-2,2´-bipyridyl (^{R}bpy) ligands to tune the photophysical properties and light-induced reactivity of $Mn(CO)_3X(^{R}bpy)$ complexes[11] as well as to modulate the accessible pathways and efficiency of dihydrogen production by [Cp*Rh] complexes bearing ^{R}bpy ligands.[12] Such modifications have also been used to tune catalysis of carbon dioxide (CO_2) reduction to carbon monoxide (CO) by $[Re(CO)_3]$ and $[Mn(CO)_3]$ complexes.[13,14] With these observations and many others from the field, ^{R}bpy ligands have been found to be uniquely suited to systematic investigation of transition metal complexes. Furthermore, the wide range of accessible ^{R}bpy ligands makes them attractive for efforts in rational design of new metal complexes and molecular catalysts.

Ligands based upon 4,5-diazafluorene (daf) have several features in common with the workhorse ^{R}bpy ligands, and thus offer a notable alternative for development of new metal complexes and catalysts.[15] In particular, both daf and bpy have $12e^-$ π systems and both commonly bind to metals in a κ^2 fashion. However, daf is distinguished from bpy by its more rigid structure, attributed to the linking inter-ring sp^3-hybridized carbon present in the fused five-membered ring. Photochemical studies of metal complexes supported by daf and bpy have mapped the importance of these features, including involvement of the daf π-system in metal-to-ligand charge transfer behavior.[15,16] Furthermore, the constrained chelate angle of daf has been implicated in giving rise to more significant excited-state reactivity than that encountered for bpy.[17]

Unfunctionalized daf features two doubly benzylic C–H bonds at the 9-position, opening further possibilities for ligand-centered acid/base reactivity that cannot occur with simple 2,2´-bipyridyl derivatives. Along these lines, Song and co-workers have explored the coordination chemistry of daf and substituted diazafluorenes, including significant work aimed at leveraging this unique acid/base chemistry.[18] In their work, Song and co-workers have found that the acidic C–H bonds of daf can undergo deprotonation that results in follow-up reactivity.[19,20,21,22,23] More broadly, Stahl[24,25,26] and several other groups[27,28,29] have developed a number of catalyst systems supported by diazafluorene ligands. In all these cases, daf and its derivatives seem to play a decisive role in enabling unique chemistry, confirming the usefulness of the ligands as a counterpoint to the more common ^{R}bpy family.

As we have found in our own work that redox-active compounds and catalysts can be readily tuned by substituent effects with ^{R}bpy ligands,[11,12] 4,5-diazafluorene-based ligands could be useful in modulating the structural, electronic, and electrochemical properties of redox-active compounds more commonly supported by ^{R}bpy derivatives. In particular, the coordination chemistry of the ligand 9,9´-dimethyl-4,5-diazafluorene (Me_2daf) has received less attention than it deserves,[26] as this ligand avoids the acidic C–H bonds present in daf that can readily engage in non-innocent behavior. Furthermore, reliable methods from Schmidt and co-workers[30] and Tetsuya and co-workers[31] are available for preparation of Me_2daf, encouraging further exploration of its chemistry.

In this chapter, we describe the synthesis, characterization, and electrochemical properties of $Mn(CO)_3Br(daf)$ (**2**), $Mn(CO)_3Br(Me_2daf)$ (**3**), and $[Ru(Me_2daf)_3](PF_6)_2$ (**5**), and compare their properties to the more common analogues $Mn(CO)_3(bpy)Br$ (**1**) and $[Ru(bpy)_3]^{2+}$ (**4**), respectively (see Chart 1 for structures of all compounds). We find that the use of daf and Me_2daf ligands in

the complexes leads to unique spectroscopic features in the NMR and electronic absorption spectra, as well as a characteristic shift in the C–O vibrational frequencies found in the infrared (IR) spectra of **2** and **3** compared to that of **1**. Consistent with these spectroscopic observations, results from single-crystal X-ray diffraction analysis of **2**, **3**, and **5** reveal wider chelate angles and elongated M-N bond lengths in comparison with the analogous bpy complexes. The new complexes exhibit electrochemical profiles that are akin to those of their bpy analogues, confirming the similar redox-active natures of bpy, daf, and Me_2daf. However, related tests shows that complexes **2** and **3** are not catalysts for the reduction of CO_2 to CO, contrasting with the robust catalytic behavior of **1.**[7] Taken together, these results suggest that Me_2daf is an attractive ligand for development of new coordination compounds for use in studies of redox chemistry and catalysis.

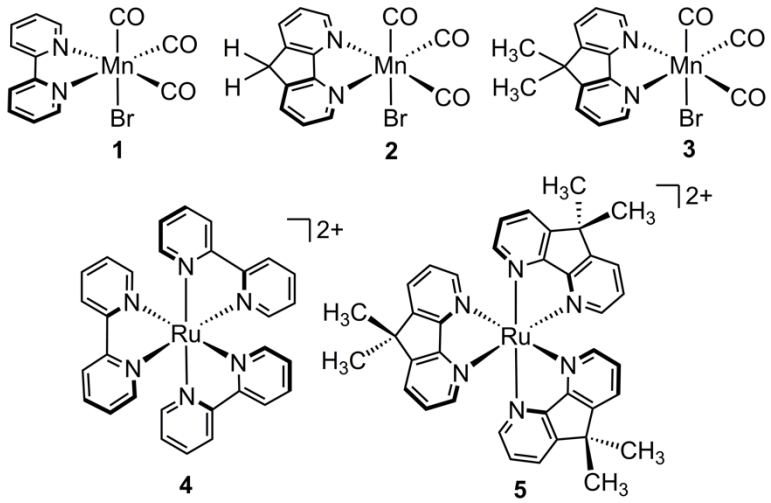

Chart 1. Manganese tricarbonyl and ruthenium complexes supported by bpy, daf, and Me_2daf discussed in this study.

Results and Discussion

*Synthesis and NMR characterization of complexes **2**, **3**, and **5***

In order to synthesize the new compounds **2**, **3**, and **5**, we first prepared the daf and Me_2daf ligands according to literature procedures starting from 1,10-phenanthroline (phen). Oxidation of the unique olefinic functionality within phen results in the production of 4,5-diazafluoren-9-one (dafone); Wolf-Kishner reduction of dafone with hydrazine hydrate results in the generation of the desired daf.[30] To generate Me_2daf, we initially attempted deprotonation of the daf methylene protons using *n*–butyllithium, but in our hands this resulted in decomposition. Instead, we utilized a milder, sterically hindered base, potassium *tert*-butoxide (tBuOK), to deprotonate daf, followed by the addition of iodomethane, to generate the anticipated Me_2daf ligand.[31]

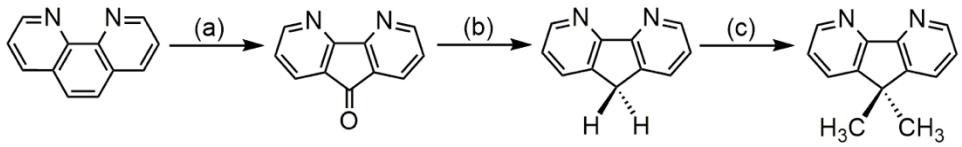

Scheme 1. The synthetic pathway for the generation of daf and Me_2daf. (**a**) 1. KOH, $KMNO_4$; H_2O, 16 h, 100 °C (**b**) $NH_2NH_2{\cdot}H_2O$; diethylene glycol, 170 °C, (**c**) 1. tBuOK 2. MeI; THF, –10 °C to rt.

Considering the straightforward synthesis of Me_2daf using iodomethane as an electrophile, we anticipated other electrophiles might be useful for generation of daf-type ligands. Unfortunately, use of benzyl bromide (BnBr) as an electrophile in this reaction sequence results in the apparent preferential formation of 9,9´-dibenzyl-1-*N*-benzyl-4,5-diazafluorenium bromide (**Bn_3daf**), an off-target compound that was confirmed using ^{1}H-NMR, mass spectrometry, and single crystal X-ray diffraction analysis (see Appendix 1 and Figures S49, S50, and S51). Thus, the use of BnBr here provides a contrasting result to what occurs when using iodomethane as the electrophile and was not pursued further.

With the desired ligands in hand, we next moved to prepare **2** and **3** with synthetic chemistry developed earlier by Wrighton, Meyer, and others for related bpy and phen derivatives.[32,33,34] Suspension of the appropriate ligand with $Mn(CO)_5Br$ in diethyl ether at 38 °C results in the generation of complexes **2** and **3** in moderate yields, 62% and 73%, respectively. Previously, Cherry and co-workers have reported the synthesis of the complex $[Ru(daf)_3](PF_6)_2$ to examine its structural properties and photophysical properties.[15] By adapting this literature procedure, the Me_2daf analogue of $[Ru(bpy)_3]^{2+}$ could be prepared in a relatively low yield of ca. 17%. As an aside, we anticipate that the modest yield is likely due to differences in solubility between $[Ru(daf)_3](PF_6)_2$ and **5** engendered by the methyl groups of Me_2daf. Notably, all the compounds in this study supported by daf-type ligands were found to be acutely light sensitive and were handled in the dark or under red light to the extent possible. Following successful generation of the complexes they were each fully characterized (see Appendix 1 and Figures S1-S9).

To begin characterization of the newly synthesized complexes, we turned to nuclear magnetic resonance (NMR) spectroscopy. Complexes **2**, **3**, and **5** each exhibit three resonances in the aromatic region of their ^{1}H-NMR spectra with splitting patterns arising from $^3J_{H,H}$ and $^4J_{H,H}$ coupling; these signals correspond to the hydrogen atoms on the pyridyl rings of the daf and Me_2daf ligands coordinated to their respective Mn and Ru centers (see Figure 1). Notably, complexes **2**, **3**, and **5** exhibit unique resonances for their daf-methylene and Me_2daf-methyl protons. While complexes **2** and **3** exhibit C_s symmetry in solution, complex **5** shows D_3 symmetry. Correspondingly, the six methyl groups belonging to the three Me_2daf ligands coordinated to the Ru center give rise to a singlet at 1.68 ppm (integrating to 18 H) confirming the successful preparation of complex **5**. The assignment of D_3 symmetry suggests that complex **5** is chiral and thus should be present as a 50:50 racemic mixture (of Δ and Λ isomers; *vide infra*). However,

enantiomers have identical chemical and physical properties and thus we observe no additional resonances in the NMR spectra for the material isolated here.

Considering the change in symmetry from D_3 for **5** to C_s symmetry for **2** and **3**, unique NMR resonance in the latter two cases can be readily interpreted. Complex **2** possesses C_s symmetry in solution and, as a result, the chemical environment of the two protons on the methylene bridge (9-position) become chemically distinct from each other and are diastereotopic. This results in a distinctive signal centered at 4.29 ppm. The geminal coupling between the two methylene protons on daf might be anticipated to give rise to two unique doublets. However, when the frequency of the coupling constant (^2J = 22.6 Hz) is on the same order of magnitude as the chemical shift difference (25 Hz) between the two expected resonances, the usual one-to-one value for the resonance intensities is not observed.[35,36] Instead, a multiplet with intense inner peaks and weaker outer peaks is obtained, providing a diagnostic signal for the generation of complex **2** (in general, a phenomenon known in the field as 'roofing'). The identity of this signal was further confirmed by ^{13}C-Distortionless Enhancement Polarization Transfer (DEPT-135) and 2D ^{1}H-^{13}C Heteronuclear Single Quantum Coherence (HSQC) NMR techniques (see Figures S10-11). Similarly, complex **3** exhibits C_s symmetry in solution; the methyl groups on the apical carbon are diastereotopic, with one methyl oriented toward the axial CO ligand and the other oriented toward the bromide ligand. The difference in the chemical environment between the methyl group protons gives rise the anticipated diastereotopic resonances; these were observed using ^{1}H and ^{13}C NMR, providing two signals for the protons (δ 1.58 and 1.66 ppm, each integrating to 3 H) and two signals for the carbons (δ 24.4 and 25.3 ppm), confirming the expected structure of **3** in solution.

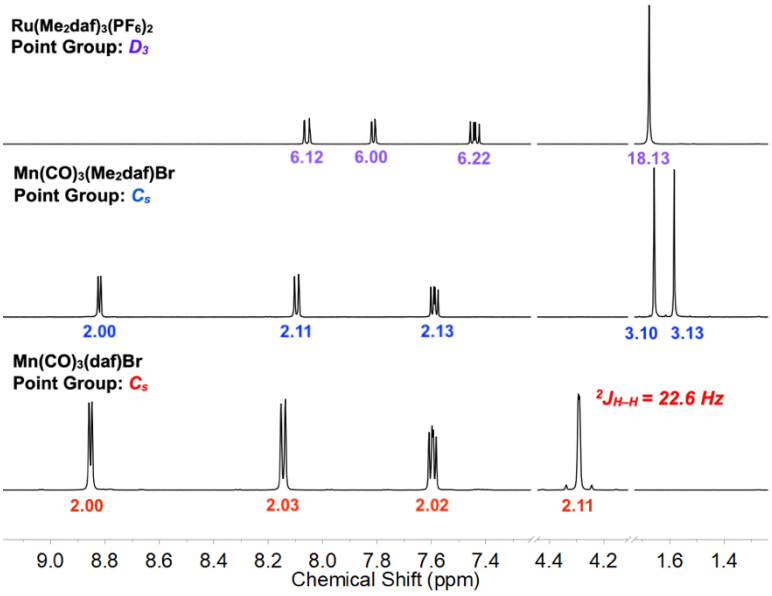

Figure 1. Partial ^{1}H NMR spectra of **2** (bottom), **3** (middle), and **5** (top) in CD_3CN. Peak integrations are given beneath each resonance or multiplet in colored text.

Electronic Absorption, IR, and X-ray Diffraction Studies

Complexes **1**–**5** are all highly colored and thus we next turned to electronic absorption (EA) spectroscopy to interrogate the electronic properties of the complexes. The EA spectrum for complex **5** exhibits a strong transition at 445 nm with a molar absorptivity of 13,000 $M^{-1}cm^{-1}$ (see Figures S17-S25). The value of the molar absorptivity and the remarkable similarity of the spectrum to that of complex **4** enables assignment of this transition as a metal-to-ligand charge transfer (MLCT).[37,38] This assignment is also consistent with known ability of daf ligands to enable visible-light induced charge transfer transitions at transition metal centers, similar to what is observed for complexes bearing bpy.[15,16] The observation of an MLCT transition for **5** supported by Me_2daf is also reasonable, since the two methyl groups installed at the 9 position of daf do not perturb the conjugated system of the two aromatic rings. The EA spectra for complexes **2** and **3** reveal transitions in the visible region at 410 nm and 411 nm with molar absorptivities of 2,200

$M^{-1}cm^{-1}$ and 3,300 $M^{-1}cm^{-1}$, respectively (see Figure 2). Notably, these EA spectra are very similar to complex **1**,[11] and based on this similarity, we are confident that these transitions can also be attributed to MLCT events.

However, a distinguishing feature of the EA spectra of complexes **2** and **3** compared to that of complex **1** is the presence of four, relatively narrow absorption bands in the UV region between 250 and 350 nm. Based on their wavelengths and molar absorptivities, these absorption bands can be assigned as π-π^* excitations displaying marked vibronic coupling. Such vibronic coupling has previously been observed for titanium complexes bearing diazafluorenide ligands,[39] suggesting that vibronic coupling may be a common feature of the spectral profiles ligated by daf or substituted diazfluorenes. As expected, the spacing between the sharp transitions is uniform in a progression from approximately 700 cm^{-1} to 900 cm^{-1}. This common observation for **2** and **3** suggests that the vibronic couplings engendered by daf and Me_2daf are similar in these compounds. Based on this rich spectroscopic profile, we anticipate that **2** and **3** may behave differently in the presence of light than the bpy analogue **1**, encouraging further work in the future to gain insight into how these complexes behave following exposure to visible and/or UV light.[11]

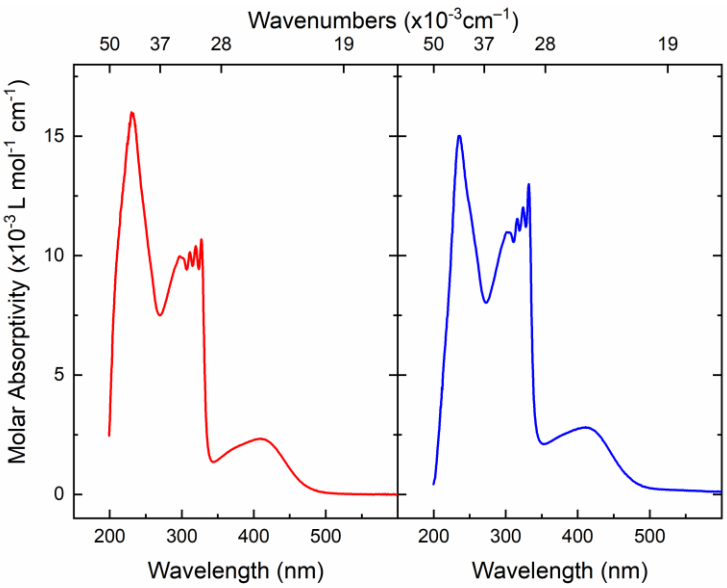

Figure 2. Electronic absorption spectra for **2** (left panel) and **3** (right panel) in MeCN.

The IR spectra of complexes **1**, **2**, and **3** confirm that the starting material, $Mn(CO)_5Br$ (associated with absorption bands at 2004 cm^{-1}, 2046 cm^{-1}, and 2083 cm^{-1}) was consumed during the synthetic reactions and is not present in the products. The C_s symmetry of a *fac*-tricarbonyl complex is expected to give rise to three distinct C–O stretches in IR spectra based on group theory analysis. Upon examination of the experimental data, a three-band spectrum is observed, confirming the expected *fac*-tricarbonyl geometry for the complexes in THF solution (see Figure 3). The complexes have rather similar C–O stretching, likely a consequence of the similar environment at Mn in all three cases. In particular, C–O stretching frequencies are primarily affected by π-bonding effects, and as the π-character of bpy, daf, and Me_2daf are not significantly different, a large shift in the vibrational frequencies for the CO ligands among **1**, **2**, and **3** is not expected. On the other hand, the modest shifts that are observable likely arise from the increased chelate bite angle of daf (**2**, 82.14(10)°) and Me_2daf (**3**, 82.2(3)°) compared to bpy (78.80(7)°, *vide infra*).[40] As a result of the increased bite angle, the σ-donor power of the nitrogen donor atoms to

the manganese center should be decreased, resulting in a correspond increase in the C–O stretching frequency due to decreased Mn-to-CO backbonding. In accord with this model, the vibrational frequencies for **2** and **3** are virtually identical, confirming that the addition of distal methyl groups at the ligand 9 position does not substantially perturb the structure of Me_2daf in comparison with daf. To gain further structural insights into the properties of the new compounds, we next turned to X-ray diffraction analysis (XRD).

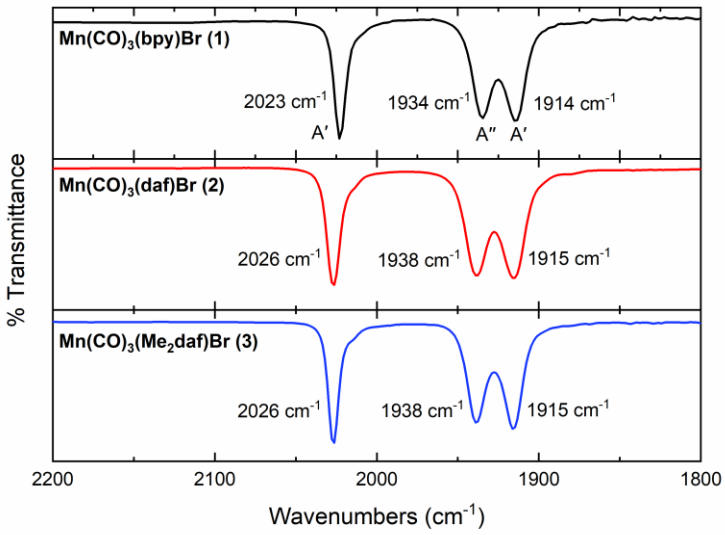

Figure 3. FTIR spectra of **1**–**3** in THF solution.

Vapor diffusion of diethyl ether into a concentrated THF solution of **2**, or vapor diffusion of diethyl ether into a concentrated acetonitrile (MeCN) solution of **3**, resulted in yellow crystals suitable for single crystal X-ray diffraction studies (see Figure 4). The results confirm the expected *fac*-geometry of the complexes with two equatorial CO ligands, an axial CO ligand, an axial bromide, and a κ^2-daf ligand surrounding the manganese center. Although this is the first example of a formally Mn(I) complex chelated by daf or Me_2daf, the octahedral geometries of **2** and **3** resemble those of the analogous $Mn(CO)_3(^{R}bpy)Br$ complexes.[11,40] However, there is a significant

increase in the diimine ligand bite angle for complexes **2** (82.14(10)°) and **3** (82.2(3)°) compared to **1** (78.80(7)°, *vide supra*). Additionally, the average Mn–N distances for **2** and **3** are significantly longer than those of complex **1** (2.118(4) Å and 2.109(5) Å vs. 2.047(3) Å, respectively).[40] This is attributable to the rigid polycyclic structure of the daf framework, enforced by the inter-ring methylene group at the 9 position, which presumably drives poorer orbital overlap between the metal center and the ligand in the cases of **2** and **3**, and results in an overall increase in the M–N bond distances.

Complex **5** is chiral and possesses D_3 symmetry in solution, on the basis of NMR spectra (*vide supra*). No measures were taken to obtain enantiomerically pure material, and thus we isolated **5** as the 50:50 racemic mixture of delta (Δ) and lambda (Λ) isomers. Vapor diffusion of pentane into a concentrated acetone solution and vapor diffusion of pentane into a concentrated 50:50 acetone/THF solution resulted in two separate sets of orange crystals of **5** that were suitable for single-crystal XRD studies (see Figure 4). These two structures, named v74e and q36k respectively, both provide data confirming the successful synthesis of the $[Ru(Me_2daf)_3]^{2+}$ core and reveal bond distances and angles that are within error of each other (see the Supporting Information, Table S3 and S4 for comparisons. On the other hand, q36k represents a higher quality structure and will be discussed here. As expected, the average chelate angle (N-Ru-N) and corresponding average Ru–N distances for complex **5** (data from q36k) are larger than in the case of the famous $[Ru(bpy)_3]^{2+}$ (82.9(3)° vs. 78.9(2)°; 2.117(13) Å vs. 2.063(6) Å).[41,42,43] Gratifyingly, these values align with structural data previously available for $[Ru(daf)_3]^{2+}$, confirming that use of daf or Me_2daf to form homoleptic Ru(II) complexes results in wider chelate angles and longer Ru–N distances in both cases.[44]

Overall, observing the increased bite angles of the daf and Me_2daf ligands in complexes **2**, **3**, and **5** was gratifying, since these changes should influence the electronic properties and reactivity at the metal centers in comparison with their bpy-supported analogues. Therefore, we next turned to electrochemical methods to probe the redox properties of these systems, with a particular focus on identifying features that distinguish the daf and Me_2daf compounds from their bpy-supported analogues.

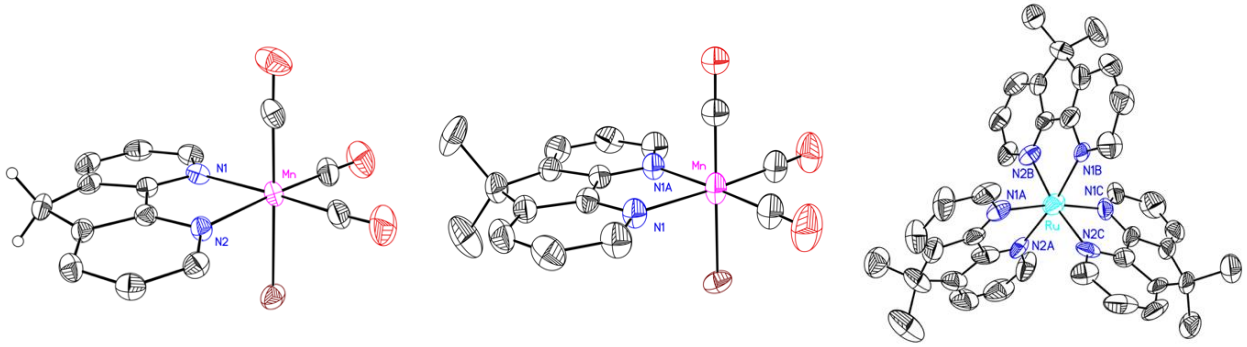

Figure 4. Solid-state structures (from XRD) of **2** (left), **3** (middle), and **5** (right, from structure v74e). Displacement ellipsoids are shown at the 50% probability level. Hydrogen atoms (except H14A and H14B for **2**) and outer-sphere hexafluorophosphate counter-anions and disordered co-crystallized solvent (for **5**, from structure v74e) are omitted for clarity.

Electrochemical Studies

Initial cyclic voltammetry experiments were performed with **4** and **5** to interrogate how Me_2daf behaves under electrochemical conditions in comparison to bpy (see Figure 5). As one scans cathodically, the cyclic voltammetry of the parent bpy-complex **4** exhibits three quasi-reversible reductions centered at –1.73 V, –1.92 V, and –2.17 V respectively (all potentials are quoted versus ferrocenium/ferrocene, denoted $Fc^{+/0}$). Based on previous electrochemical studies, these reductive features can be confidently assigned to ligand-centered events; the complex is progressively reduced from $[Ru^{II}(bpy)_3]^{2+}$, to $[Ru^{II}(bpy)_2(bpy^{\cdot-})]^{+}$, to $[Ru^{II}(bpy)(bpy^{\cdot-})_2]$, and

finally to $[Ru^{II}(bpy^{\cdot-})_3]^{-}$.[45,46,47] This rich manifold of accessible ground-state reductions for **4** highlights the redox non-innocence of the bpy ligand; redox non-innocent ligands continue to grow in popularity[4,26,48,49] because of their wide-ranging applications in redox chemistry and small-molecule activation.

We were excited to find that the cyclic voltammetric profile of **5** is remarkably similar to that of **4**. As scanning cathodically with **5** reveals three quasi-reversible reductions at –1.79 V, –1.99 V, and –2.24 V, respectively; each is centered at a slightly more negative potential than the corresponding event associated with bpy-complex **4**. The more negative reduction potentials likely arise from the inductive effect of the additional fused five-membered ring and methyl groups of Me_2daf, resulting in a structure that is overall more electron-rich and thus slightly increasing the reduction potentials associated with Me_2daf-centered reductions of **5**. Based on the electronic similarities of bpy and Me_2daf, we can reliably implicate redox non-innocence of the Me_2daf ligand as giving rise to the manifold of reductions observed for **5**, similar to the case of bpy in **4**. Considering this situation, we anticipate that **5** could have significant photochemical reactivity, and might be useful to investigate as a photosensitizer in future work.

Consistent with the ligand-centered nature of the reductive events measured for **4** and **5**, the difference in the bite angle between Me_2daf and bpy does not strongly affect the reductive cyclic voltammetry of these compounds. However, confirmation that that Me_2daf behave as a redox-active ligand suggests that similar processes may be accessible in the tricarbonyl compounds **2** and **3**.

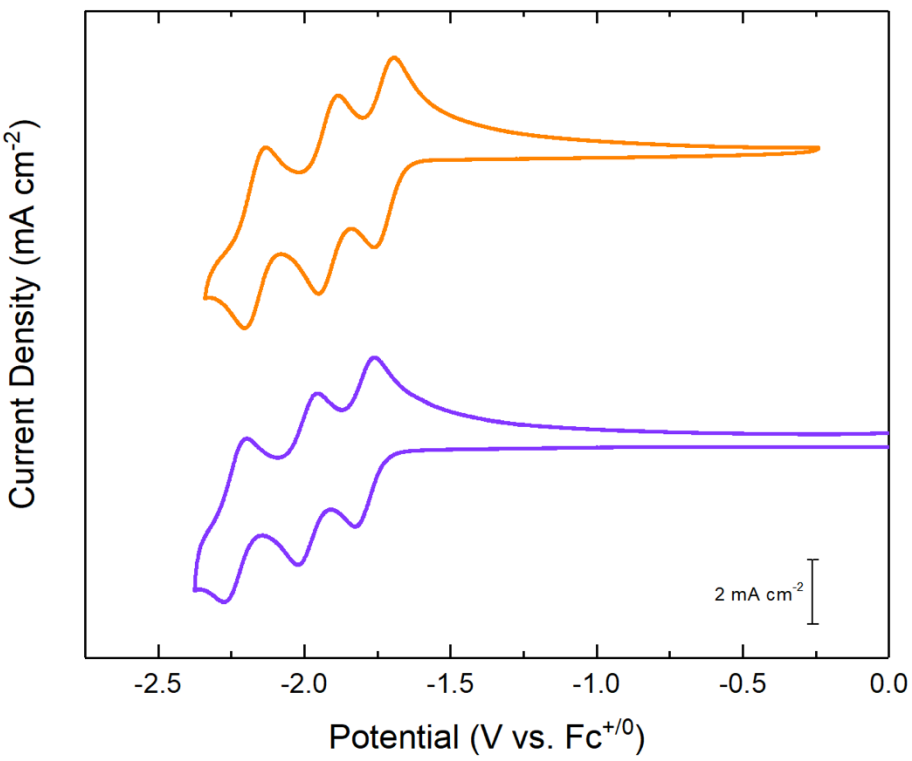

Figure 5. Cyclic voltammetry of **4** (orange) and **5** (purple) in MeCN solution with 0.1 M $TBAPF_6$ supporting electrolyte (working electrode: highly-oriented pyrolytic graphite; pseudo-reference electrode: $Ag^{+/0}$; counter electrode: Pt wire). Ferrocene was used as an internal potential reference.

The electrochemical behavior of **1** was previously established by Deronzier, Chardon-Noblat and co-workers.[7] We have confirmed their findings here for comparison purposes (see Figure 6); scanning cathodically with **1** in solution, we observe two irreversible reductions with cathodic peak potentials ($E_{p,c}$) at –1.61 V and –1.83 V, followed by an oxidation at a more positive potential ($E_{p,a}$ = –0.61 V). Based upon extensive mechanistic work from prior studies, the first reduction of **1** is associated with formation of a 19 e^- complex (an electron transfer or E process) which is coupled to the loss of bromide that generates a 17 e^- species (a chemical reaction or C process). This 17 e^- complex then dimerizes with itself (C process), forming $[Mn(CO)_3(bpy)]_2$ in an overall ECC-type process. $[Mn(CO)_3(bpy)]_2$ itself can then undergo reduction at the more

negative potential, breaking the dimer to form $[Mn(CO)_3(bpy)]^-$ in an EC-type process. Finally, scanning anodically, oxidation of $[Mn(CO)_3(bpy)]_2$ can regenerate the starting material **1**.

The cyclic voltammetric profiles of **2** and **3** are very similar to that associated with **1** (see Figure 6). Scanning cathodically with **2** or **3**, two irreversible reductions and followed by an oxidation at more positive potentials during the paired anodic sweep (for **2**, $E^{(1)}_{p,c} = -1.75$ V, $E^{(2)}_{p,c} = -2.04$ V, $E_{p,a} = -0.62$ V; for **3**, $E^{(1)}_{p,c} = -1.71$ V, $E^{(2)}_{p,c} = -2.02$ V, $E_{p,a} = -0.67$ V). Qualitatively, these results suggest that the irreversible reductions corresponding to the ECC and EC processes exhibited by **1** also occur with **2** and **3**. Notably, however, the reduction events associated with **2** and **3** appear significantly broader than those associated with **1**, suggesting that heterogeneous electron transfer is slower with the diazafluorene derivatives. Furthermore, as $E^{(1)}_{p,c}$ and $E^{(2)}_{p,c}$ are both more negative for **2** than **3**, we anticipate that electron transfer kinetics dominate the potentials measured for these reductions; Me_2daf might have been expected to engender a more negative reduction potential for **3** over the case of daf in **2**, but the opposite is in fact observed here; this may be attributable to the influence of the disparate electron-transfer kinetics, which push the reduction potential ($E^{(1)}_{p,c}$) of **2** to a more negative potential than **3**, contrary to the thermodynamic trend that would be predicted on the basis of the inductive effect of the methyl groups of Me_2daf.

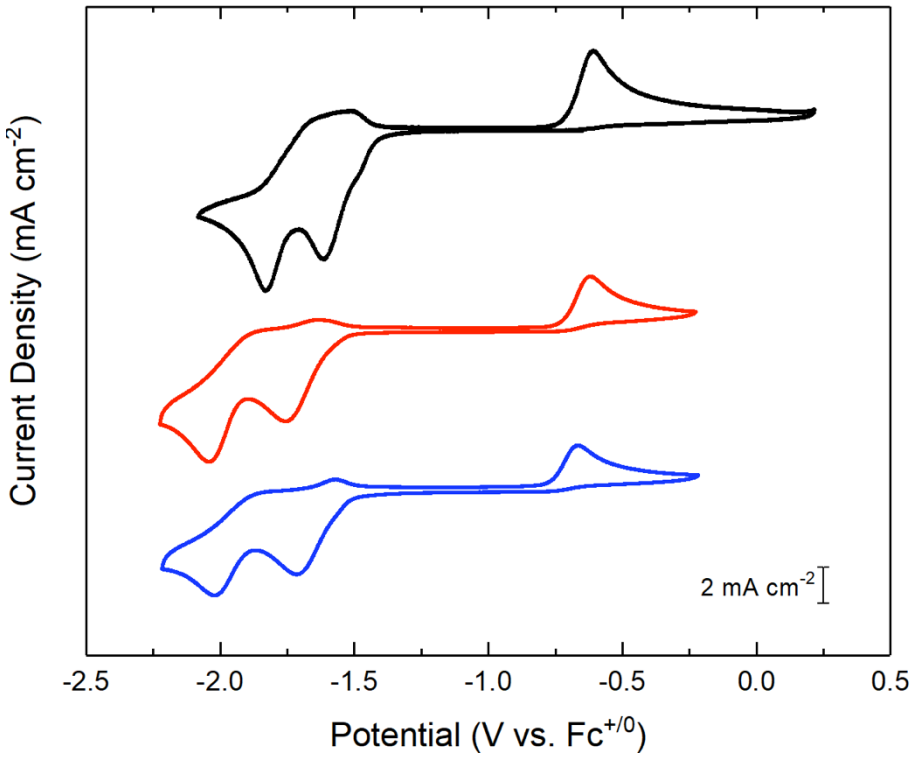

Figure 6. Cyclic voltammogram of complexes **1** (black), **2** (red), and **3** (blue) in MeCN solution with 0.1 M $TBAPF_6$ electrolyte (WE: HOPG, Psuedo Ref: $Ag^{+/0}$, CE: Pt, internal Ref: $Fc^{+/0}$).

Encouraged by the similar cyclic voltammetry (CV) behavior displayed by **1**, **2**, and **3**, we also tested the new compounds for activity towards CO_2 reduction (see Figures S34–S39) since the known **1** has been demonstrated to be a robust catalyst for CO generation from CO_2.[7] For this testing, water was added as a proton source (similar to the prior work with **1** described in reference 7) and CO_2 was sparged through the working solution and electrochemical cell to fully saturate the atmosphere and solution. Voltammograms collected immediately following these additions reveal enhancements in the current that flows at both the first and second irreversible reductions associated with **2** and **3**. The observed current enhancement suggests that significant reduction-induced reactivity is taking place at the electrode surface. Notably, the overall catalytic enhancement encountered with **2** is significantly greater than that with **3**, suggesting a unique role of the acidic protons on the methylene bridge of daf in promoting reactivity.

However, controlled potential electrolysis (CPE) coupled to product detection does not suggest effective catalytic reduction of CO_2 is taking place with **2** and **3**. Results from controlled potential electrolyses at –2.05 V vs $Fc^{+/0}$ for 90 min (see Figures S40 and S41) in a custom two-compartment electrochemical cell do show that experiments with **2** and **3** produce less H_2 and more CO during the 90 min electrolysis (see Table S1). However, **2** and **3** give low Faradic efficiencies (27% and 34%) and sub-stoichiometric yields (turnovers of 0.82 and 0.62, respectively) of CO, on the basis of total charge passed and initial loading of **2** or **3**, respectively. As analysis of working solutions with NMR spectroscopy following electrolysis did not reveal the presence of alternative products, including formate, we conclude that electrochemical reduction of **2** or **3** in the presence of H_2O and CO_2 leads primarily to decomposition rather that effective CO_2 conversion.

On a final note, we wish to highlight that the chronoamperogram associated with electrolysis of **2** is considerably different than that of **3**. The current passed as a function of time widely fluctuated during the course of the electrolysis (see Figure S40); in particular, the initial current is rather large but becomes attenuated over the course of the experiment, suggesting undesirable chemical reactivity may be taking place with the daf ligand. These results suggest that further work is needed to reveal the precise role of the acidic methylene protons in the daf framework during conditions of redox catalysis, like those explored here. It should also be noted that both metal- and bpy-centered reductions have been implicated in effective catalysis of CO_2 reduction with **1**.[50] As incoming CO_2 might therefore be required to interact with both the metal and the ligand, the enhanced steric profile of Me_2daf ligand in **3** could negatively impact the approach of CO_2 and deactivate the catalyst. Consequently, future work could focus on revealing the influence of the functionalization pattern of the 9-position of daf on redox chemistry and catalysis with these platforms.

Conclusions

We have described the synthesis, characterization, and electrochemical properties of the new daf- or Me_2daf-supported complexes **2**, **3**, and **5** and compared the properties of these compounds to their bpy-supported analogues **1** and **4**. When daf and Me_2daf are bound to Mn or Ru centers, we observe characteristic spectra that confirm the formation and symmetry of the desired complexes. In particular, comparisons of bond lengths and geometric parameters confirm that daf and Me_2daf enforce wider chelate angles and offer weaker σ-donation than bpy. Electrochemical studies of **5** reveal that Me_2daf is a non-innocent redox active ligand at modestly reducing potentials, and related electrochemical work with **2** and **3** shows that this ligand-centered reduction behavior is also accessible in **2** and **3**, albeit with apparently slower heterogeneous electron transfer kinetics that those encountered with analogous **1**. Despite the facile synthesis of daf- and Me_2daf-supported complexes, we have demonstrated that the synthesis described herein cannot be applied to benzylated derivatives. Taken together, these studies demonstrate that daf and Me_2daf could be useful for preparation of a variety of new redox-active compounds, building on the significant body of findings for the workhorse bpy and ^{R}bpy ligands.

Acknowledgments

The authors thank Javier Concepcion (Brookhaven National Laboratory) for helpful discussions regarding the synthesis of **5**, and Justin Douglas and Sarah Neuenswander for assistance with NMR spectroscopy. This work was supported by the US National Science Foundation through award OIA-1833087. Synthesis and preliminary characterization of **5** was supported by the US National Science Foundation through the NSF REU Program in Chemistry at

the University of Kansas (CHE-1560279). J.P.S. was supported by the Beckman Scholars Program at the University of Kansas, funded by the Arnold & Mabel Beckman Foundation, as well as by an Undergraduate Research Award from the Center for Undergraduate Research. W.C.H. was supported by the US National Institutes of Health Graduate Training Program in the Dynamic Aspects of Chemical Biology (T32 GM008545- 25) as well as by a Graduate Student Research Grant from the Kansas Academy of Science. Support for the NMR instrumentation was provided by the NIH (S10OD016360, S10RR024664) and the NSF (CHE-1625923), and support for EPR instrumentation was provided by the NSF (CHE-0946883).

Author Contributions

Conceptualization: J.D.B., W.C.H., J.P.S., J.A.H.; Synthesis and characterization of Mn and Ru complexes: W.C.H., J.A.H., M.L.A., and V.W.D.; Synthesis of dafone and daf: J.P.S., W.C.H., and M.L.A.; Synthesis of Me_2daf: W.C.H.; Synthesis and characterization of Bn_3daf: J.P.S., W.C.H., and V.W.D.; Supervision: W.C.H., J.A.H. and J.D.B.; Writing—original draft: W.C.H.; J.D.B.; Writing—review and editing: J.P.S., J.D.B., W.C.H., V.W.D. and J.A.H..

Chapter 3: Redox Properties of [Cp*Rh] Complexes Supported by Monosubstituted Bipyridyl Ligands

This chapter is based upon work that is in preparation for publication.

Abstract

Half-sandwich rhodium complexes supported by bidentate chelating ligands are a useful class of compounds for study of molecular electrochemistry and electrocatalysis. Here, the synthesis and characterization of two new [Cp*Rh] complexes (where Cp* is η^5-pentamethylcyclopentadienyl) supported by the uncommon ligands 4-chloro-2,2′-bipyridyl (mcbpy) and 4-nitro-2,2′-bipyridyl (mnbpy) are reported. Single-crystal X-ray diffraction studies and related spectroscopic experiments confirm installation of the single substituents (–Cl and –NO_2, respectively) on the bipyridyl ligands; the precursor monosubstituted ligands were prepared via a divergent route from the inexpensive, unsubstituted starting material 2,2′-bipyridine (bpy). Electrochemical studies reveal that each of the complexes undergo an initial net two-electron reduction at potentials more positive than that associated with the parent unsubstituted complex of bpy, and that the complex supported by mnbpy can undergo an unusual, chemically reversible third reduction event at –1.62 V vs. ferrocenium/ferrocene. This redox behavior is consistent with inductive influences from the substituent groups on the supporting ligands, although the nitro group uniquely enables reduction by a third electron. Spectrochemical studies carried out with UV-visible detection confirm the redox stoichiometry of these platforms. These findings highlight the rich redox chemistry and tuneable behavior of [Cp*Rh] complexes supported by monosubstituted bpy ligands.

Introduction

Understanding and, ultimately, controlling the redox properties of well-defined metal complexes are important goals in the fields of redox chemistry and molecular catalysis.

Organometallic complexes in particular attract significant attention in these realms, due to their important roles as catalysts and redox mediators. Control over the redox properties of metal complexes can be exercised with a variety of strategies; these include ligand modifications with inductive groups, use of "non-innocent" ligands that are redox-active or proton-responsive, formation of multimetallic species, and surface immobilization, among others.[12,57,62] However, determining the precise origin of modified redox chemistry within even closely related families of complexes is often challenging; even small changes to ligands supporting organometallic complexes can result in significant changes in their chemical properties.

The 2,2′-bipyridyl (bpy) ligand platform is ubiquitous in organometallic chemistry and is perhaps the most well-studied type of bidentate ligand.[51] The useful catalytic, photophysical, and redox properties of such compounds, in addition to the modular nature of the platform, have led to intense interest in tuning the properties of these systems. The installation of electron donating groups (EDG) or electron withdrawing groups (EWG) enables the tuning of the redox properties of the parent complex.[12] Such modifications primarily alter the π-accepting ability of the conjugated framework, and to a lesser extent alter the σ-donating ability of the imine nitrogens. Additionally, we have recently shown (as in Chapter 1 of this thesis) that modifying the bite angle of the ligand provides an alternative means of tuning the electronic properties by adjusting the degree of orbital overlap between the metal center and donor nitrogens.

Systems bearing ligands analogous to bpy-type species have also been extensively studied. In our own group, diphosphines have been especially useful for comparison to bpy.[52] Rhodium half-sandwich diphosphine compounds have drawn particular interest due to their propensity to form stable metal hydrides upon protonation. These isolable hydrides are notable for their structural similarity to transient, reactive hydrides formed by their half sandwich diimine

analogues. In principle, backbonding from the metal center to the phosphorous donor atoms can be envisioned to remove electron density from the metal center, thereby resulting in diminished hydricity and limited reactivity. Characterization of these diphosphine analogues has served as a useful strategy for elucidation of the electronic influences over the hydride generating step in the catalytic cycle for H_2 evolution by some half-sandwich rhodium bpy complexes.

Most such studies of half-sandwich rhodium bpy complexes have been conducted using symmetrically di-substituted bpy ligands. However, to the best of our knowledge, no half-sandwich rhodium complexes bearing non-symmetrically substituted bpy ligands have been used for chemical and electrochemical studies aimed at characterizing the precise role of ligand substituents in modulating the reduction potentials associated with rhodium complexes of these ligands. Toward this goal, we describe here the synthesis, characterization, and electrochemical properties of two previously unreported half-sandwich rhodium complexes supported by non-symmetrically mono-substituted bpy ligands bearing either a chloro (−Cl) or nitro ($-NO_2$) substituent.

Results and Discussion

*Divergent Synthesis of **Rh(mcbpy)** and **Rh(mnbpy)***

A divergent synthesis of **Rh(mcbpy)** and **Rh(mnbpy)** was previously developed and studied by William Moore (B.S., U. Kansas, 2019) and other members of the Blakemore Group based on a combination[53,54,55,56] of reported literature procedures that had not been considered together previously; this synthetic route was used here and found to produce quantities of pure material suitable for further studies. The synthesis begins with the oxidation of inexpensive and

readily available 2,2′-bipyridine (bpy) to 2,2′-bipyridine-1-oxide (bpy-*N*-oxide) by treatment with concentrated hydrogen peroxide and trifluoroacetic acid (see Figure 1). The mono-*N*-oxide product, being lower symmetry than the parent bpy, can engage in further non-symmetric reactivity that was previously inaccessible. Specifically, the position *para* to the *N*-oxide is activated to electrophilic aromatic substitution, while the second pyridine ring is unaffected. This allows for selective nitration at the 4-position to generate mono-nitrobipyridine-*N*-oxide (mnbpy-*N*-oxide). At this point, the synthesis diverges. Reaction with acetyl chloride in acetic acid replaces the nitro group with a chloride substituent to form mono-chlorobipyridine-*N*-oxide (mcbpy-*N*-oxide). Reaction of either *N*-oxide species with excess phosphorous(III) chloride results in the removal of the *N*-oxide to form mnbpy or mcbpy, respectively.

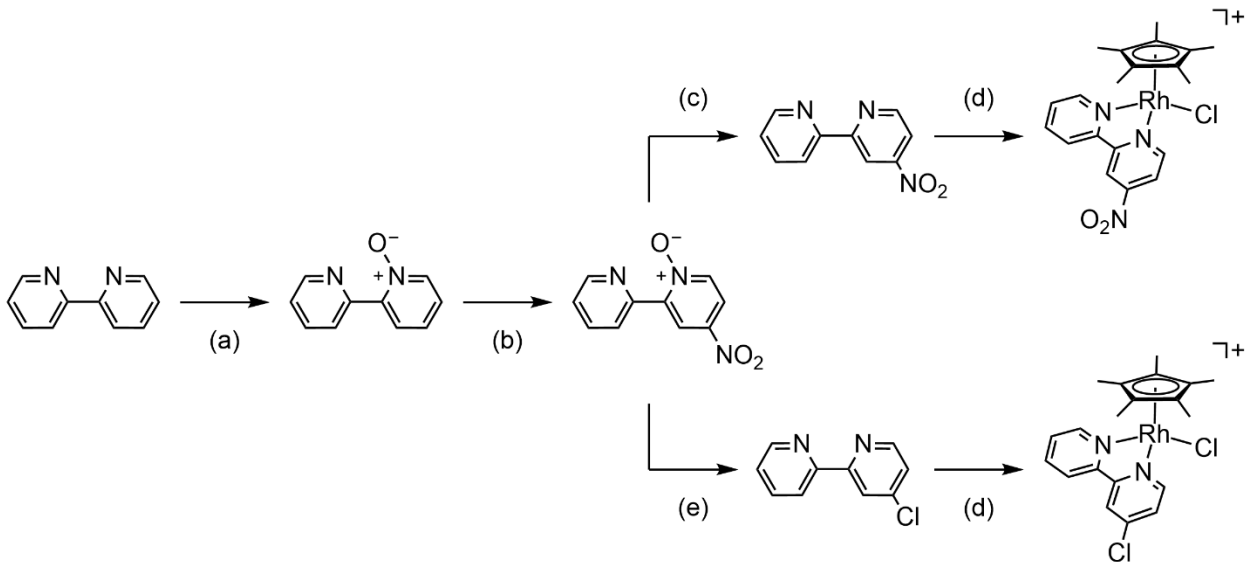

Figure 1. Divergent synthesis of **Rh(mnbpy)** and **Rh(mcbpy)**. A. Trifluoroacetic acid, 30% H_2O_2; 25 °C. B. Red fuming nitric acid, conc. H_2SO_4; 100 °C. C. PCl_3; 65 °C. D. $[Cp^*RhCl_2]_2$, $AgPF_6$; 25 °C. E. 1. Acetic acid, acetyl chloride; 100 °C. 2. PCl_3; 65 °C.

The rhodium complexes of both isolated ligands, **Rh(mnbpy)** and **Rh(mcbpy)**, were synthesized by identical procedures that were found to be applicable to both complexes.[57] First,

$RhCl_3 \cdot nH_2O$ was refluxed with pentamethylcyclopentadiene (Cp*H) in isopropanol to form $[Cp^*RhCl_2]_2$. [58,59] This brick red solid, after being isolated and dried, was suspended in a solution of dichloromethane and acetonitrile. One equivalent per rhodium center of $AgPF_6$ was added to the suspension to activate the chloride bridged dimer by abstracting chloride. This formed a precipitate of AgCl and a bright orange solution. This reaction was protected from light due to the propensity for Ag^+ to act as a photooxidant.[60] After the AgCl was removed by filtration, **mnbpy** or **mcbpy** was added to the solution. Following two hours of stirring at room temperature, a yellow to orange precipitate of **Rh(mnbpy)** or **Rh(mcbpy)**, respectively, was formed. The solid was isolated by suction filtration followed by washing with diethyl ether.

During synthesis of the new complexes, it was found to be vital that elevated temperatures be avoided, as the complexes were found to be extremely heat sensitive. For example, when removing solvent from solutions of the complexes *in vacuo*, even as little as 40 °C for 30 minutes caused the complexes to decompose into a viscous oil containing a mixture of products which could not be identified by NMR. Additionally, the complexes were found to be unstable in solution over moderate timescales. Solutions of the complexes stored at room temperature demonstrated significant decomposition after less than 24 hours, as judged by NMR. Therefore, all work with the complexes was performed with freshly made solutions at room temperature or below.

To confirm the successful isolation of the new complexes, we utilized NMR spectroscopy. Figures 2-5 and Figures 6-9 show the ^1H, $^{13}C\{^1H\}$, ^{19}F, and ^{31}P NMR spectra of **Rh(mnbpy)** and **Rh(mcbpy)**, respectively. The ^1H NMR spectrum of **Rh(mnbpy)** contains the expected seven aromatic signals as well as a single signal integrating to fifteen, which is indicative of the five equivalent methyl groups of the Cp* ligand. However, the ^1H NMR spectrum of **Rh(mcbpy)** contains only six aromatic signals, with one of the aromatic signals integrating to two because of

coincidental overlap of two distinct aromatic signals. The $^{13}C\{^{1}H\}$ NMR spectrum of **Rh(mnbpy)** exhibits eight resonances rather than the expected twelve. This can be explained through the slow relaxation times typical of quaternary carbon atoms preventing their detection in this case. Conversely, the $^{13}C\{^{1}H\}$ NMR spectrum of **Rh(mcbpy)** exhibits thirteen resonances, one more than the expected twelve. This is a result not only of the quaternary carbon resonances being detected, but also of a singlet resonance being split into a doublet by the presence of the spin-1/2 rhodium atom. In the ^{19}F and ^{31}P NMR spectra, no significant difference was detectable between **Rh(mnbpy)** and **Rh(mcbpy)**. All fluorine and phosphorous atoms present in the new complexes are contained within the hexafluorophosphate counter anion. As an outer sphere anion, the electron distribution in the hexafluorophosphate ion is unaffected by rhodium ligand substitution. Based on these spectra, the complexes were determined to be free of NMR active impurities.

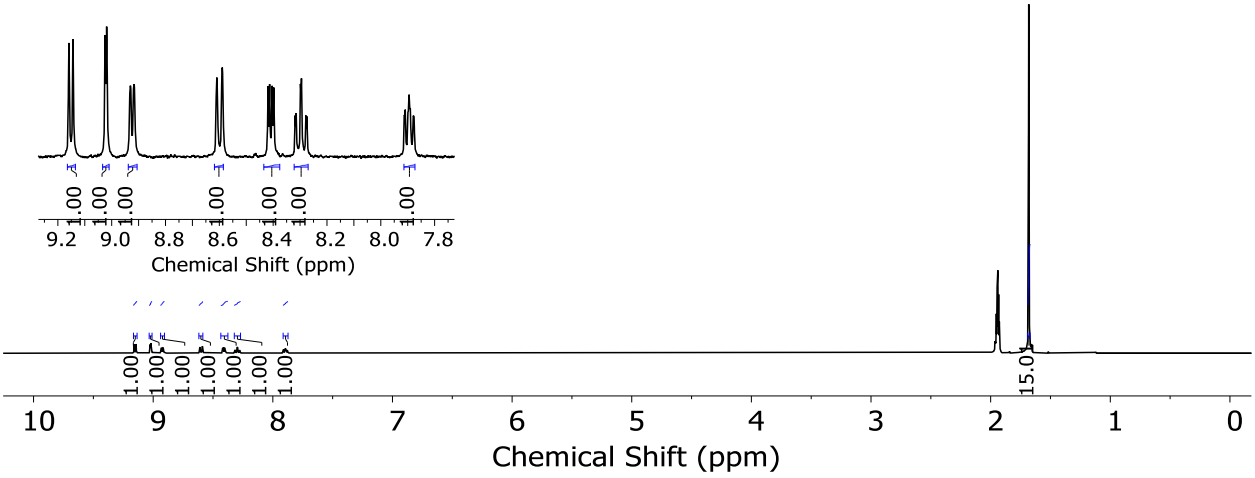

Figure 2. ^{1}H NMR spectrum of **Rh(mnbpy)** (400 MHz, CD_3CN).

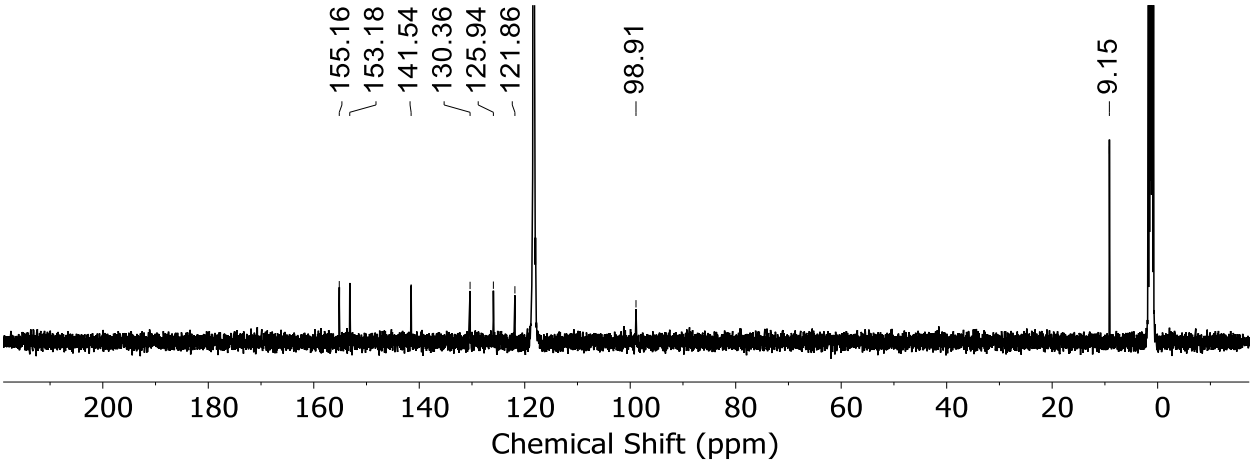

Figure 3. $^{13}C\{^{1}H\}$ NMR spectrum of **Rh(mnbpy)** (126 MHz, CD_3CN).

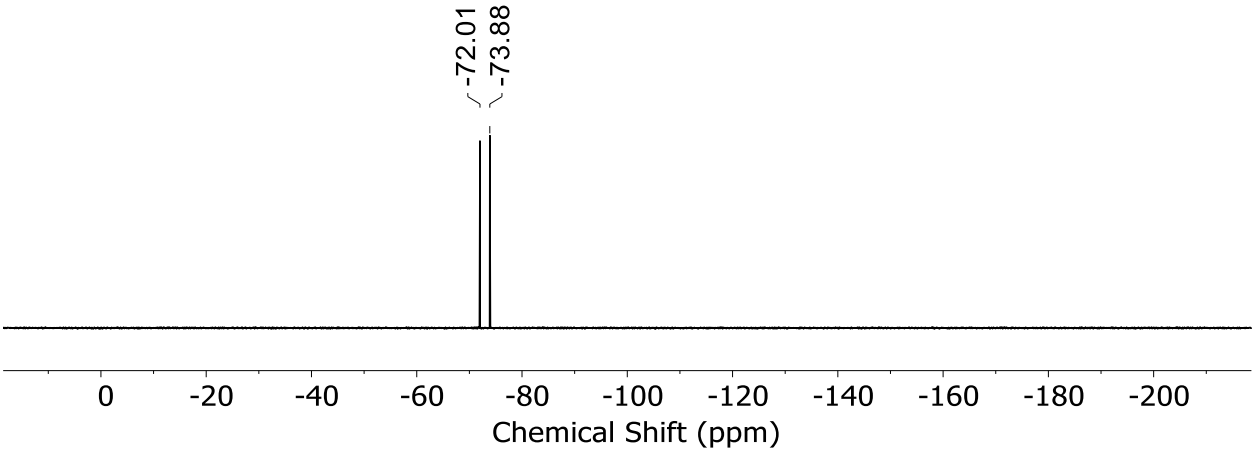

Figure 4. ^{19}F NMR spectrum of **Rh(mnbpy)** (376 MHz, CD_3CN).

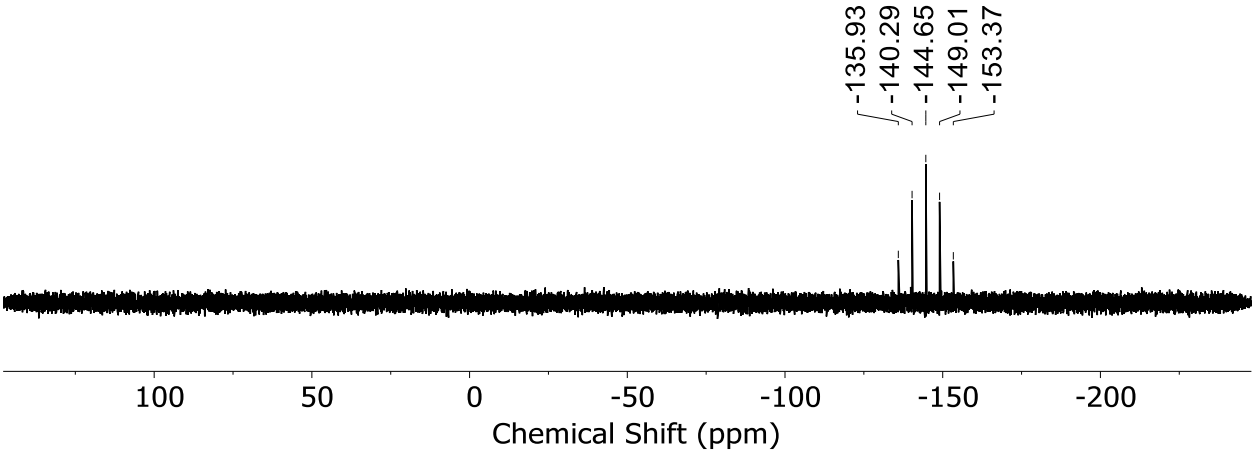

Figure 5. ^{31}P NMR spectrum of **Rh(mnbpy)** (162 MHz, CD_3CN).

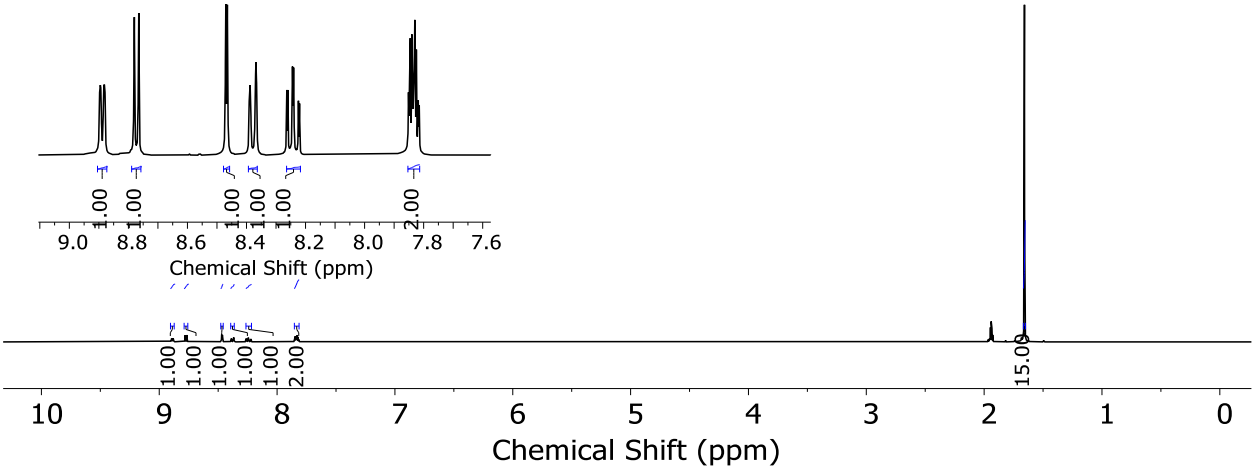

Figure 6. ^{1}H NMR spectrum of **Rh(mcbpy)** (400 MHz, CD_3CN).

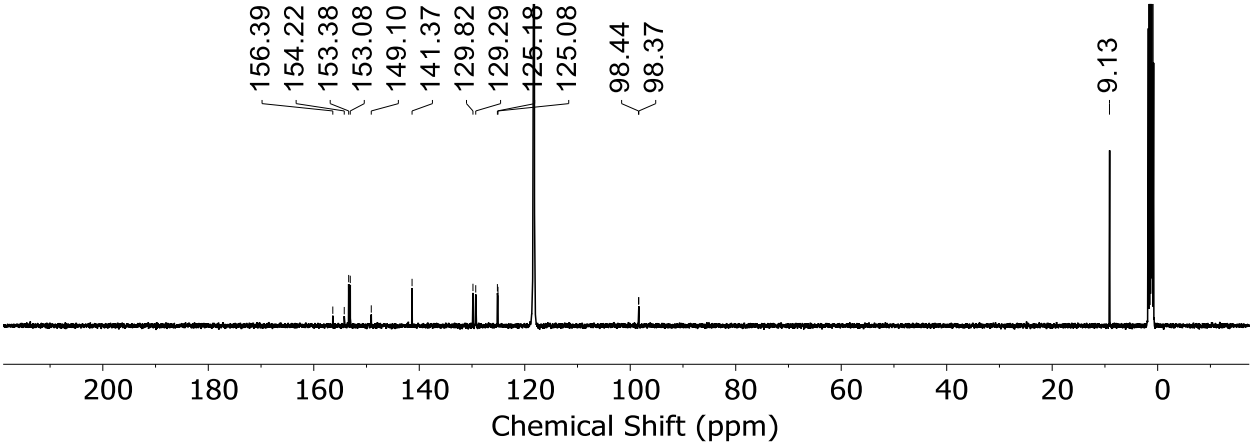

Figure 7. $^{13}C\{^{1}H\}$ NMR spectrum of **Rh(mcbpy)** (126 MHz, CD_3CN).

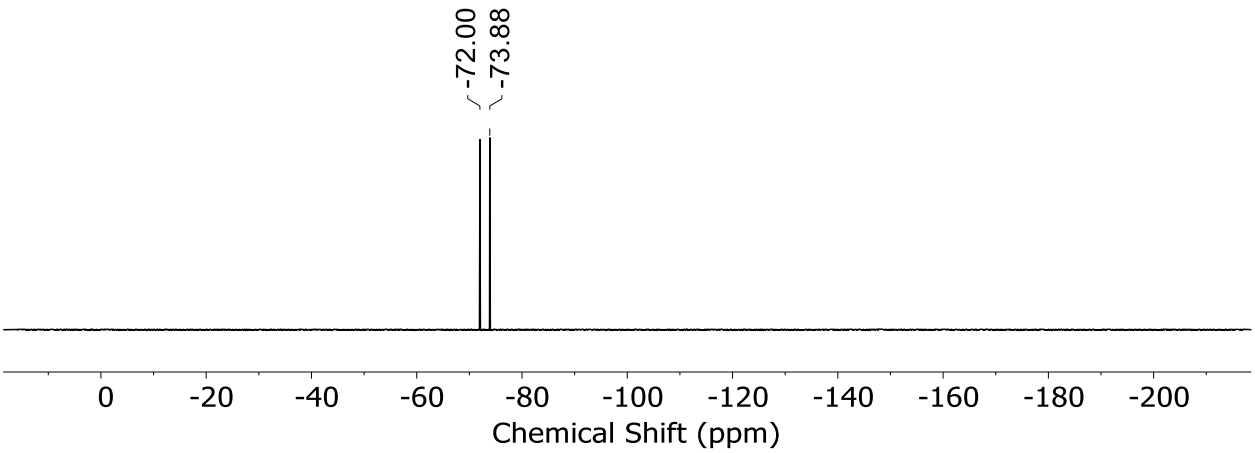

Figure 8. ^{19}F NMR spectrum of **Rh(mcbpy)** (376 MHz, CD_3CN).

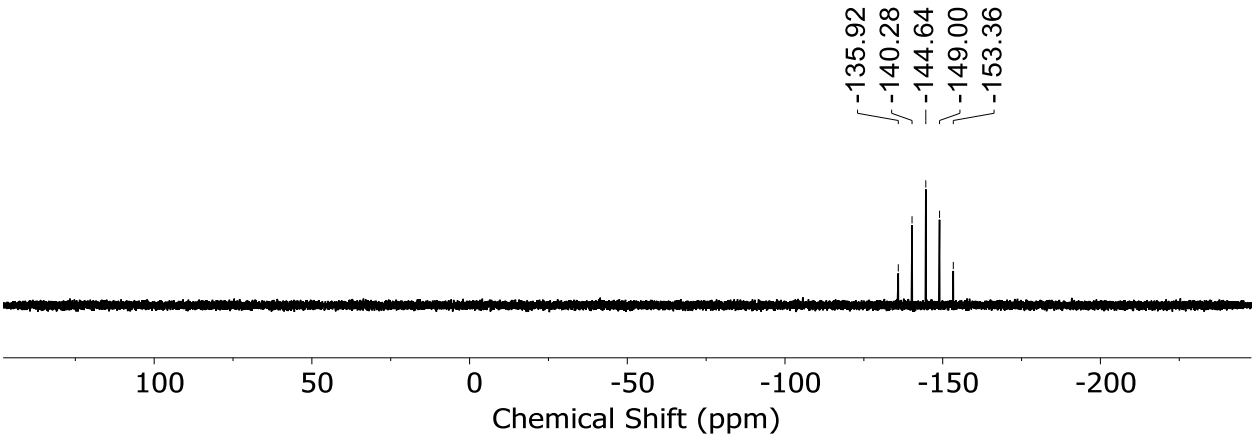

Figure 9. ^{31}P NMR spectrum of **Rh(mcbpy)** (162 MHz, CD_3CN).

*Electrochemical and Spectrochemical Studies of **Rh(mnbpy) and Rh(mcbpy)***

To interrogate the electrochemical properties of the new complexes, cyclic voltammetry was performed. Since water and oxygen could potentially interfere with reductive chemistry by reacting with the reduced complexes or by themselves being reduced at the electrode through direct electron transfer, all electrochemical and spectrochemical studies were performed in an inert atmosphere glovebox. Thoroughly dried samples of the new complexes were dissolved in a dry electrolyte of 0.1 M tetrabutylammonium hexafluorophosphate ($TBAPF_6$) in acetonitrile to form

solutions that were 2 mM in the desired complex. Cyclic voltammetry was performed on these solutions using the basal plane of a highly oriented pyrolytic graphite (HOPG) block as the working electrode (WE; 0.09 cm^2), a platinum wire counter electrode (CE), and a silver wire immersed in electrolyte in a separate fritted chamber as a pseudo-reference electrode (RE). Ferrocene (~2 mM) was added at the conclusion of each experiment and the ferrocene/ferrocenium couple (denoted as $Fc^{+/0}$) was used as an external standard.

Under these same conditions, prior work has demonstrated that the parent Rh(bpy) complex displays a single, 2 e^- reduction event centered at −1.21 V vs $Fc^{+/0}$.[61] This redox couple is assigned as rhodium(III)/rhodium(I) with associated loss of the chloride ligand. With a peak-to-peak separation (ΔE_p) of ~250 mV, this reduction shows significant electrochemical irreversibility, consistent with the chemical changes associated with the reduction of rhodium(III) to rhodium(I). Similarly, **Rh(mcbpy)** has a single, 2 e^- reduction event centered at −1.19 V vs $Fc^{+/0}$, Figure 10. With a ΔE_p of 245 mV, this redox couple is virtually identical in appearance to that exhibited by the parent Rh(bpy). Therefore, it was also assigned as rhodium(III)/rhodium(I), again with associated loss of the chloride ligand. However, in addition to this primary redox event, a minor electrochemically quasi-reversible couple was observed at approximately −1.7 V vs $Fc^{+/0}$. This couple was tentatively assigned to be associated with redox cycling of a reduced chloride bridged dimer (i.e., $[Cp^*RhCl]_2$) based on past work by our group.[57] However, in light of the small currents associated with this process, further characterization may be needed in order to make a definitive assignment. Overall, the redox properties of **Rh(mcbpy)** appear similar to those of the parent Rh(bpy), but with an added degree of instability under strongly reducing conditions implied by the observation of the minor redox process associated with formation and redox cycling of $[Cp^*RhCl]_2$.

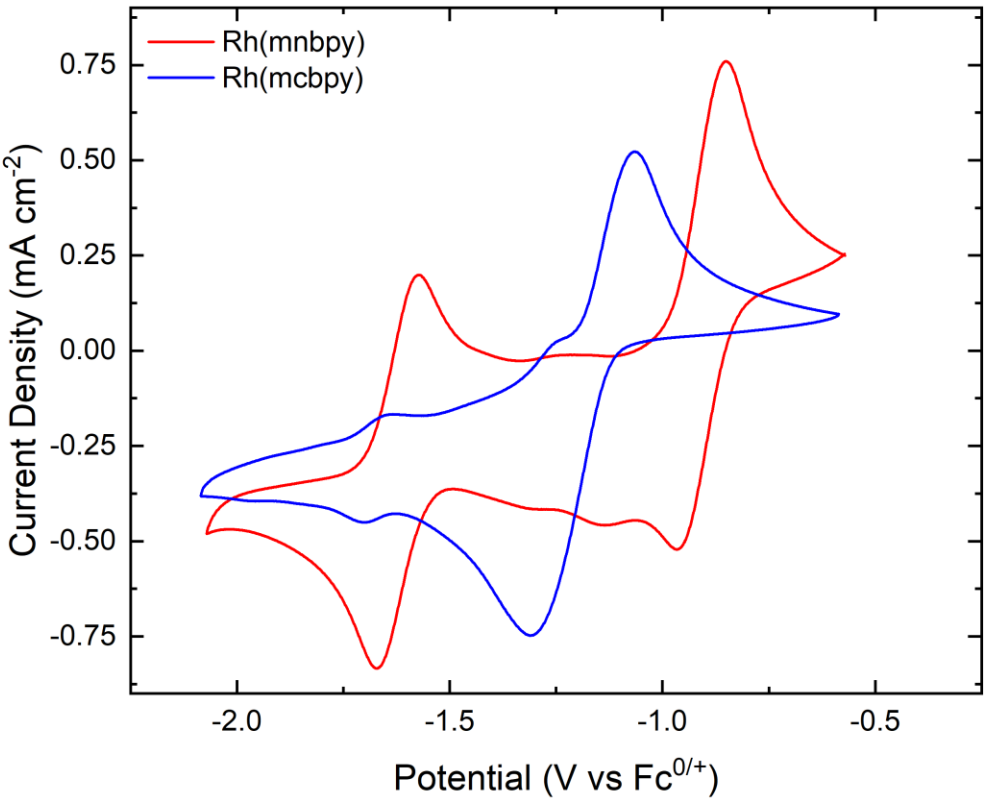

Figure 10. Overlayed cyclic voltammograms of **Rh(mnbpy)** and **Rh(mcbpy)**. **Rh(mcbpy)** has a single, $2e^-$ redox couple that is reminiscent of that of the parent bpy complex. **Rh(mnbpy)** has a $2e^-$ redox couple followed by a further, more unusual $1e^-$ redox couple.

The cyclic voltammogram of **Rh(mnbpy)** is distinct from both the parent Rh(bpy) and **Rh(mcbpy)**. Two primary redox couples were observed: a $2e^-$ couple centered at −0.91 V vs $Fc^{+/0}$ and a $1e^-$ couple centered at −1.62 V vs $Fc^{+/0}$. With ΔE_p values of 119 mV and 99 mV, respectively, both couples can be considered electrochemically quasi-reversible. The first couple is consistent with reduction from rhodium(III) to rhodium(I) as seen with the parent Rh(bpy) and **Rh(mcbpy)**. This reduction is shifted positively by 300 mV from the parent complex, ostensibly a result of the strong electron withdrawing properties of the nitro functional group. Interestingly, prior work by our group showed that in analogous complexes bearing 4,4′-di-substituted bpy ligands, electron

rich bpy derivatives were associated with smaller ΔE_p values and electron deficient derivates were associated with larger ΔE_p values.[61] Yet, **Rh(mnbpy)** with its electron deficient mnbpy ligand has a ΔE_p value that is half that of the parent Rh(bpy) complex. The result of this discrepancy is likely associated with faster electron transfer behavior in this complex or more closely spaced reduction potentials for the $1e^-$ transfer events spanned by the overall $2e^-$ wave.

The second **Rh(mnbpy)** reduction process, at −1.62 V vs $Fc^{+/0}$, was tentatively assigned as a ligand-centered reduction. This assignment was based on previous work by our group with the 4,4′-dinitrobipyridyl derivative, Rh(dnbpy).[62] Rh(dnbpy) is exceptional due to the presence of four unique $1e^-$ reductions in its cyclic voltammetric response. By completing the series formed by Rh(bpy), **Rh(mnbpy)**, and Rh(dnbpy), it can be noted that the addition of each nitro group to the bpy moiety enables an additional $1e^-$ ligand-centered reduction not observed in non-nitrated derivatives. Although this model would predict that Rh(dnbpy) would display a $2e^-$ metal-centered reduction followed by two $1e^-$ ligand-centered reductions, it is hypothesized that the extreme electron withdrawing strength of the dnbpy ligand is responsible for splitting the normally simultaneous first two reductions into distinct $1e^-$ reductions; double nitration may also shift the ligand-centered reduction significantly positive, such that the dnbpy core is reduced at a potential more positive than those associated with formal metal-centered reductions. This hypothesis is consistent with EPR data that suggests the first reduction of Rh(dnbpy) is ligand centered.[62]

Similar to **Rh(mcbpy)**, **Rh(mnbpy)** demonstrates a propensity to undergo unwanted chemical reactivity under reducing conditions. This is evident in the minor reductive peaks at −1.22 and −1.30 V vs $Fc^{+/0}$, as well as the small return oxidation peak at −1.13 V vs $Fc^{+/0}$. Due to this instability under reducing conditions, characterization of the reduction products of both compounds was performed by spectrochemical titrations rather than spectroelectrochemistry.

Spectrochemical titrations were performed in an inert atmosphere glovebox. A 1 mM solution of decamethylcobaltocene (Cp^*_2Co) was titrated into a cuvette filled with a ~70 μM solution of **Rh(mcbpy)** or **Rh(mnbpy)** while being monitored by UV-visible spectroscopy. The solution inside the cuvette was stirred with a magnetic stir bar to ensure homogeneity. The spectrum of unreduced **Rh(mcbpy)** displays a relatively sharp bifurcated absorption at 310 nm, Figure 11. The shape of this absorption is typical of analogous bpy complexes.[61] In contrast, the UV-visible spectrum of unreduced **Rh(mnbpy)** does not display this bifurcated fingerprint. Instead, there is a single broad absorption at 318 nm.

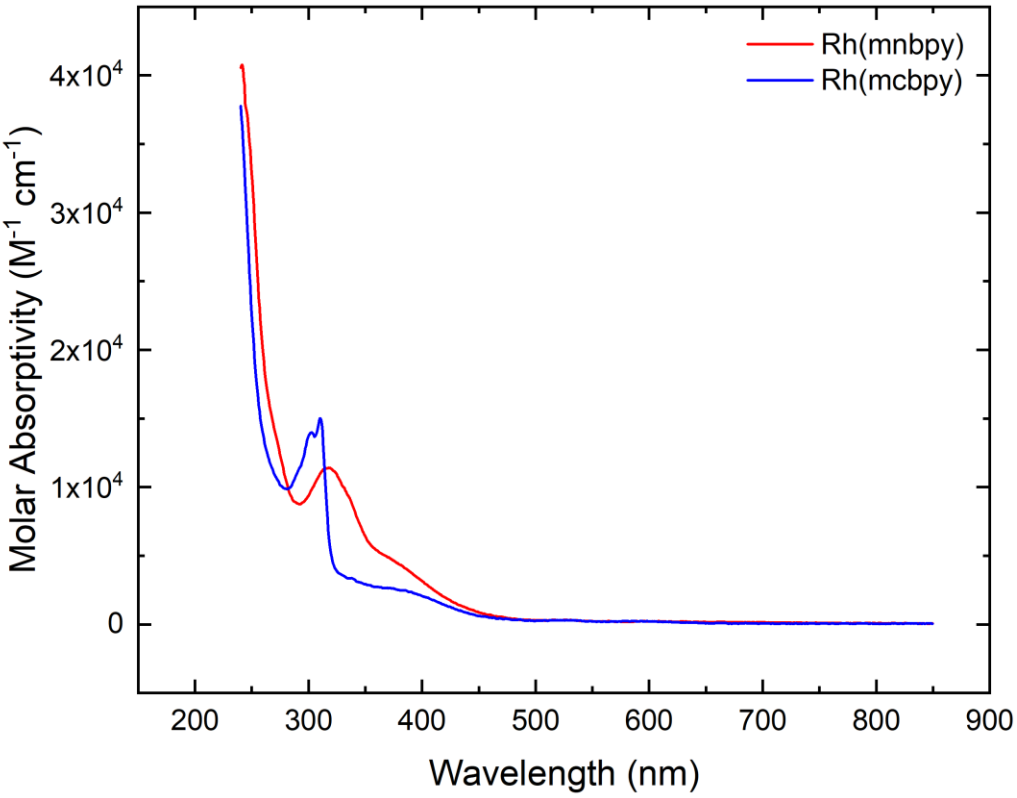

Figure 11. Wavelength dependent molar absorptivity data for both **Rh(mnbpy)** and **Rh(mcbpy)**.

Upon reduction of **Rh(mcbpy)** with Cp^*_2Co, new absorbances grow in at 298 nm and 525 nm, Figure 12. Isosbestic points at 230 nm and 247 nm are indicative of clean conversion of **Rh(mcbpy)** into its rhodium(I) analogue. Importantly, the spectrum stops evolving after the addition of two equivalents of reductant. Further additions of reductant do not lead to further spectral changes, confirming the assignment of the redox couple centered at −1.19 V vs $Fc^{+/0}$ as being a $2e^-$ couple leading to the formation of the rhodium(I) oxidation state. The spectrochemical data suggest that the rhodium(II) form of **Rh(mcbpy)** is a transient species formed upon one-electron reduction of the starting material which undergoes disproportionation to form the doubly reduced rhodium(I) complex even upon addition of substoichiometric quantities of Cp^*_2Co.

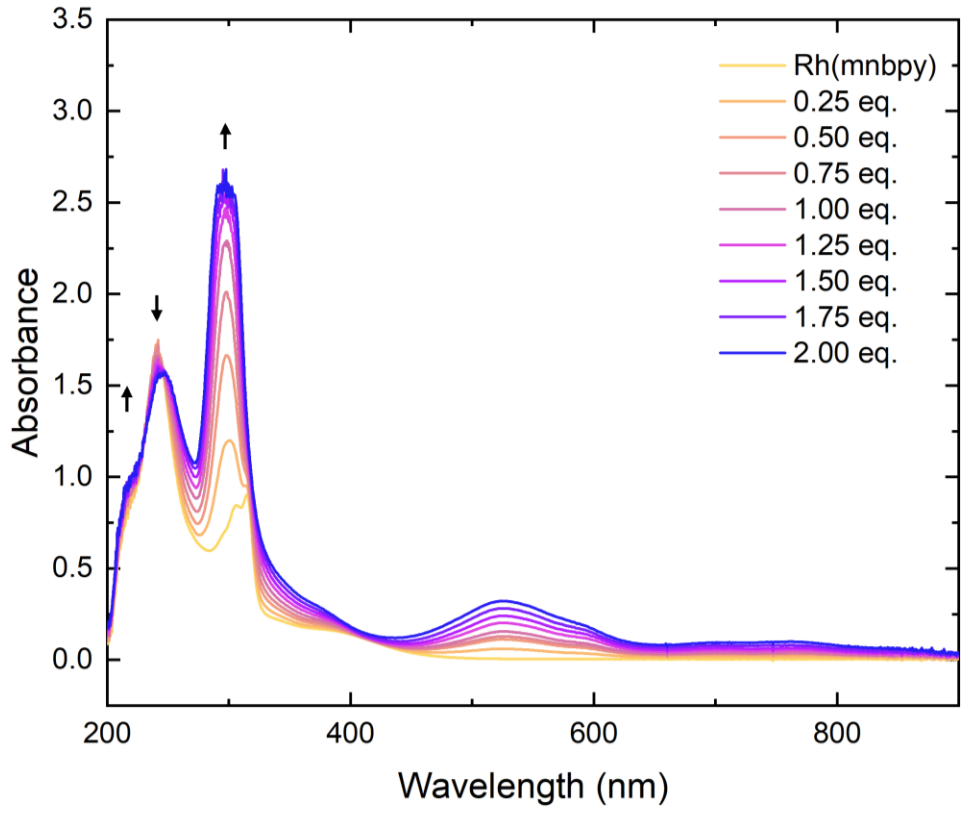

Figure 12. Spectrochemical titration of **Rh(mcbpy)** with Cp^*_2Co monitored by UV-visible spectroscopy.

Reduction of **Rh(mnbpy)** with Cp^*_2Co led to more complex spectral changes, Figure 13. To deconvolute these various changes, the spectra taken up to two equivalents of reductant added were analyzed independently from the spectra taken after the addition of two or more equivalents. Using this strategy, it was possible to separately examine the spectral changes occurring during the initial $2e^-$ reduction and those occurring during the separate $1e^-$ reduction.

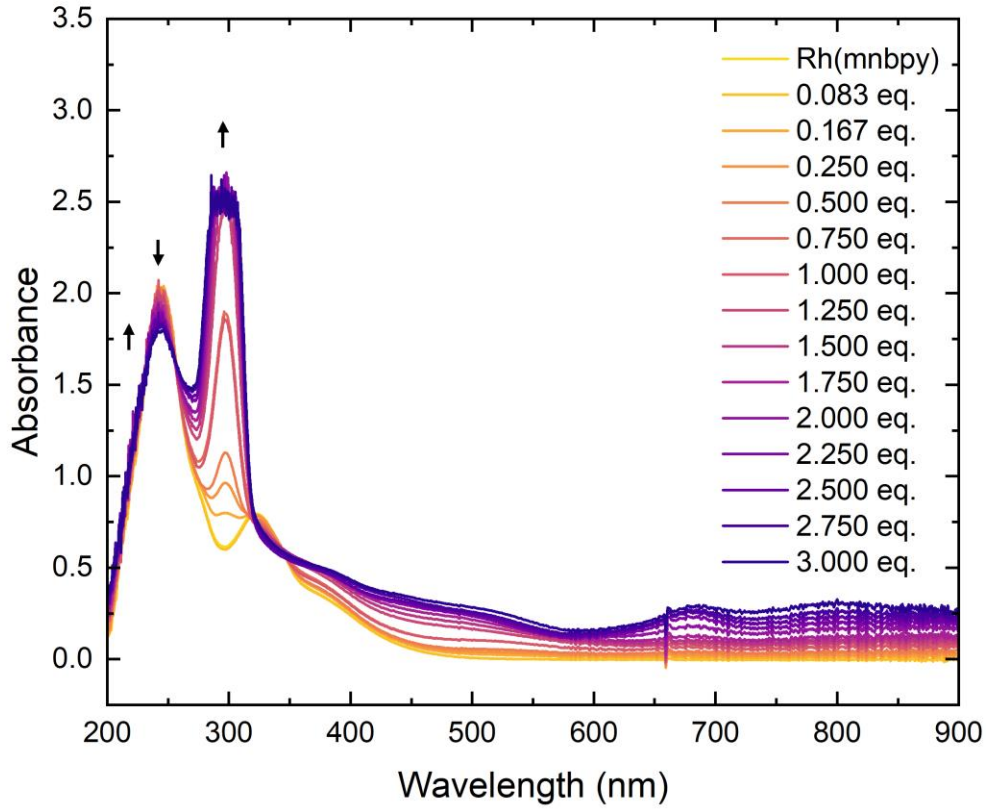

Figure 13. Full spectrochemical titration of **Rh(mnbpy)** with Cp^*_2Co monitored by UV-visible spectroscopy.

During the addition of the first two equivalents of reductant, Figure 14, new absorbances grow in at 297 nm, 370 nm, 460 nm, 685 nm, and 800 nm. Isosbestic points at 232 nm, 256 nm, and 344 nm once again indicate clean conversion of one chemical species into another. Further

additions of Cp^*_2Co up to three equivalents led to the growth of peaks at 520 nm, 685 nm, and 800 nm, Figure 15. The presence of a new set of virtually isosbestic points at 235 nm and 253 nm indicates that the triply reduced **Rh(mnbpy)** species can be generated reasonably cleanly and is stable on the timescale of this titration. Further addition of Cp^*_2Co after three equivalents led to no further spectral changes. These results confirm the assignment of the couple centered at −0.91 V vs $Fc^{+/0}$ as being a $2e^-$ redox event and the couple centered at −1.62 V vs $Fc^{+/0}$ as belonging to a $1e^-$ redox event.

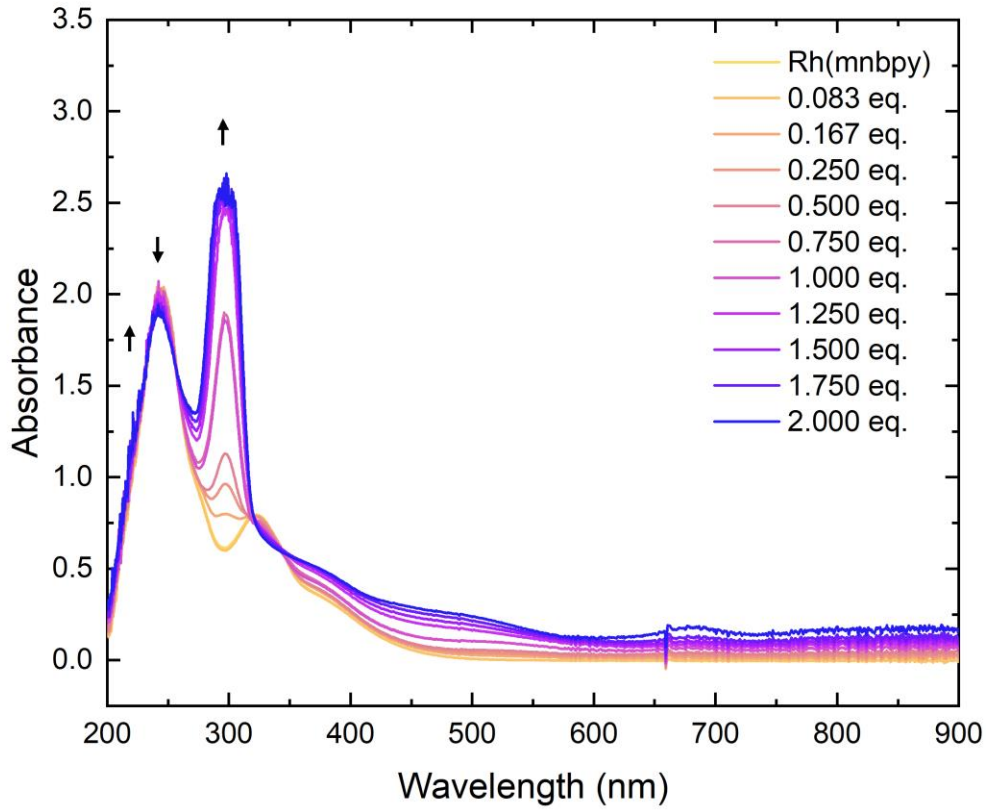

Figure 14. Spectrochemical titration of **Rh(mnbpy)** with Cp^*_2Co up to 2 equivalents of reductant.

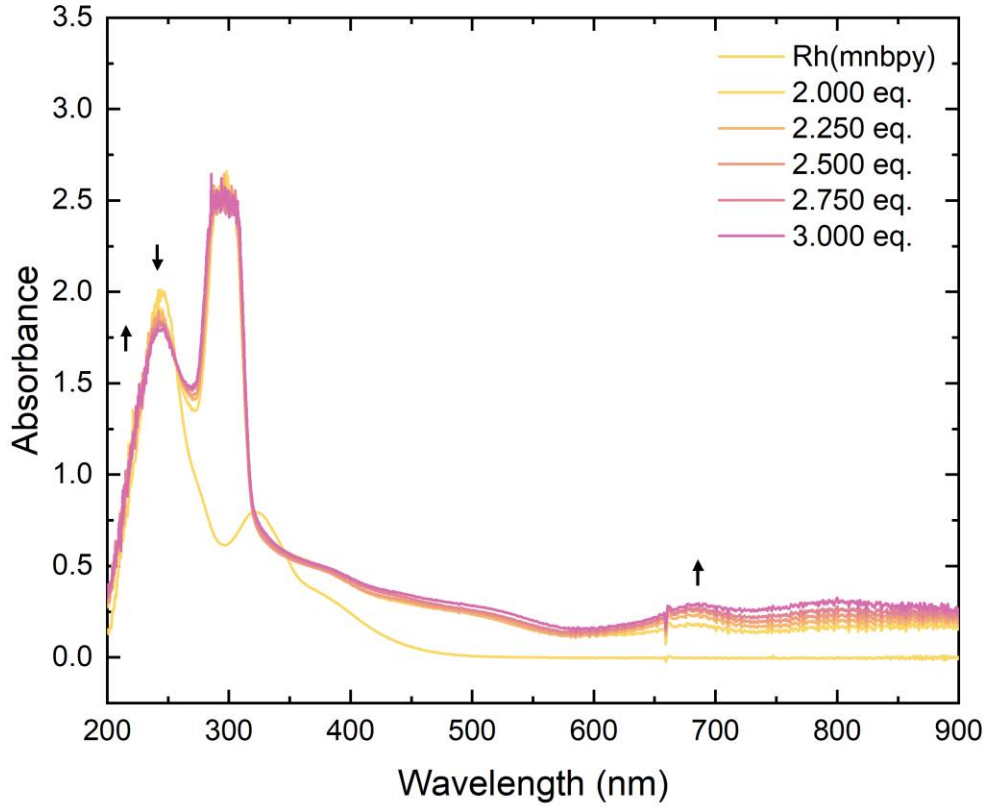

Figure 15. Spectrochemical titration of **Rh(mnbpy)** with Cp^*_2Co from 2-3 equivalents of reductant. Spectrum of **Rh(mnbpy)** with no reductant added included for comparison.

Characterization by Single Crystal X-Ray Diffraction

Single crystals suitable for X-ray diffraction analysis were grown by vapor diffusion methods in both cases. Crystals of **Rh(mcbpy)** were obtained by diffusion of diethyl ether into a solution of the complex in acetonitrile at 5 °C (see Figure 16). Suitable crystals of **Rh(mnbpy)** were obtained by diffusion of pentane into a solution of the complex in acetone at –20 °C (see Figure 17).

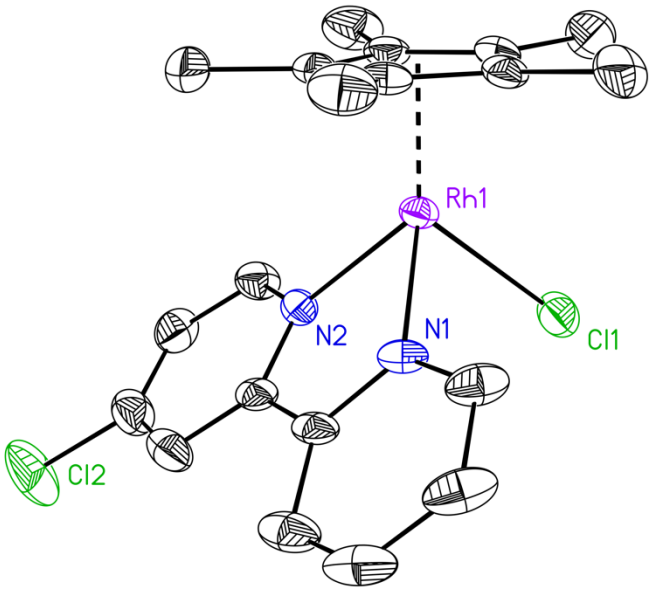

Figure 16. Solid-state structure (from XRD) of **Rh(mcbpy)**. Outer-sphere hexafluorophosphate counter-anion and all hydrogen atoms are omitted for clarity, and displacement ellipsoids are shown at the 50% probability level.

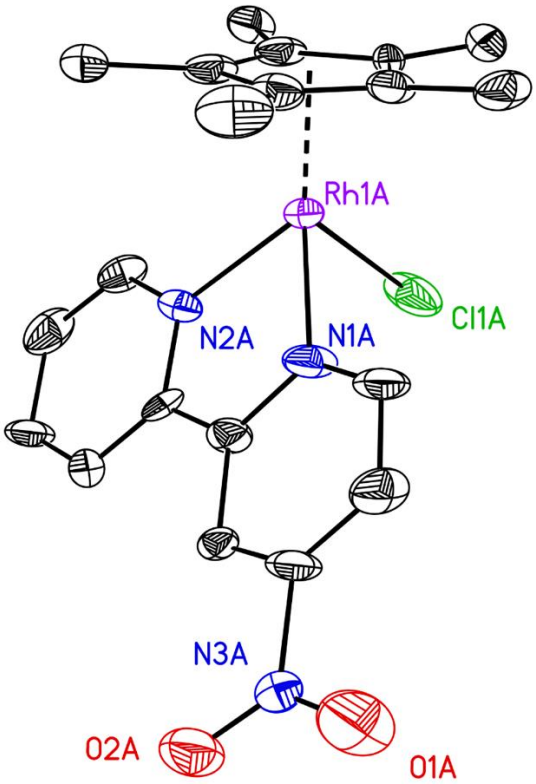

Figure 17. Solid state structure (from XRD) of **Rh(mnbpy)**. Outer-sphere hexafluorophosphate counter-anion and all hydrogen atoms are omitted for clarity, and displacement ellipsoids are shown at the 50% probability level.

Examination of bond lengths and angles from the XRD data, frequently used to characterize changes to the electronic structure of analogous complexes, shows that the new complexes fall within a similar range of values to those of the parent Rh(bpy) and Rh(dnbpy) previously characterized by our group (see Table 1).[61,62,63] This consistency with other derivatives demonstrates that non-symmetric mono-substitution of the bpy moiety has not radically altered the structure of the complex at the rhodium center. This establishes mono-substitution as a viable method of modifying the structures of such complexes, while enabling electronic tuning that is apparent from the distinctive electrochemical properties associated with the complexes studied here.

Compound	**Bond Length [Å]**					**Bond angle [°]**
	Rh–N1	Rh–N2	Rh–Cl1	d_{c-c}	Rh–Cp*$_{cent}$	∠N–Rh–N
[Cp*Rh(bpy)Cl]$^+$	2.140(7)	2.140(7)	2.379(3)	1.49(2)	1.774	75.3(4)
[Cp*Rh(mcbpy)Cl]$^+$	2.094(4)	2.117(4)	2.401(1)	1.469(7)	1.790	76.29(15)
[Cp*Rh(mnbpy)Cl]$^+$	2.09(1)	2.11(1)	2.393(4)	1.47(2)	1.777	76.9(4)
[Cp*Rh(dnbpy)Cl]$^+$	2.108(2)	2.120(1)	2.400(1)	1.473(3)	1.787	76.39(6)

Table 1. Relevant bong lengths and angles for **Rh(mnbpy)**, **Rh(mcbpy)**, the parent Rh(bpy),[63] and Rh(dnbpy).[62]

The similarities among the bond lengths and angles in this family of complexes are of particular note as they contrast with the rather dramatically varied redox properties displayed by

the complexes. While the parent Rh(bpy) and **Rh(mcbpy)** complexes have single, net $2e^-$ redox couples, **Rh(mnbpy)** displays a $2e^-$ redox couple followed by a $1e^-$ redox couple at more negative potentials, and Rh(dnbpy) has a series of four $1e^-$ redox couples. It must at first glance seem surprising to see such disparate redox behavior from a family of complexes with similar crystal structures. However, this highlights that solid-state structural data are often not reflective of subtle electronic changes in transition metal complexes, including half-sandwich rhodium complexes. While it may be tempting to predict the redox properties of such complexes solely on the basis of their solid-state structures, these data show such extrapolation could be ineffective, particularly in cases such as the one here in which inductive effects from peripheral substitution of ligand groups do not exert a dramatic *structural* influence over bonding around the metal-ligand core of the complexes under investigation.

As a final consideration, we also note here that the crystal structures of the complexes do not suggest or predict the thermal instability of the new complexes that was uncovered in the course of this work. **Rh(mcbpy)** and **Rh(mnbpy)** both have shorter Rh–N bond distances than either the parent Rh(bpy) complex or Rh(dnbpy), suggesting that these ligands might be more 'tightly bound' to the metal centers. Despite the association of shorter bond lengths with stronger bonds, **Rh(mcbpy)** and **Rh(mnbpy)** have been shown to decompose under even mildly elevated temperatures while Rh(bpy) does not. Therefore, we add that while single crystal X-ray crystallography is of great utility for demonstrating proof of synthesis of new complexes, it may be of only limited help in predicting chemical or electrochemical reactivity, particularly in a case where seemingly minor changes in ligand structure can exert major changes in solution-phase reactivity. However, as demonstrated by the work shown in this thesis, parallelizing chemical and electrochemical work is an exceptionally powerful strategy for understanding the redox properties

and oxidation-state-dependent reactivity of metal complexes. By considering chemical and electrochemical data in a common frame of reference, a coherent and often relatively complete understanding can often be obtained, as has been the case in the work described here.

Conclusion

We have described the synthesis, characterization, and electrochemical properties of the new half-sandwich rhodium complexes **Rh(mcbpy)** and **Rh(mnbpy)**. The new complexes were found to be structurally similar to the parent Rh(bpy)[63] and the previously described Rh(dnbpy)[62] complexes in the solid state, indicating that varying the electronic properties of the ligand substituents in this family of complexes does not lead to major changes in geometry or structure about the rhodium center. Yet, despite the structural similarity of this chemical series, there is a clear propensity for mono-substituted bpy derivatives to dramatically alter the redox properties of half-sandwich rhodium complexes. Indeed, the intermediate redox behavior of **Rh(mnbpy)** in comparison to the non-nitrated and doubly nitrated forms illustrates the utility of non-symmetric mono-substitution in enabling 'fine-tuning' of the redox properties of the complexes. Additionally, the ability for **Rh(mnbpy)** to undergo reduction by $3e^-$ underscores that nitro substituents are uniquely well suited for unlocking new reductive electrochemistry in organometallic complexes. Controlling the number of accessible reduction events is central to the study of redox management and is a major factor in determining what reaction pathways and products are accessible in catalytic systems. The series formed by Rh(bpy),[63] **Rh(mnbpy)**, and Rh(dnbpy),[62] with their respective abilities to be reduced by $2e^-$, $3e^-$, and $4e^-$, represents a model family of complexes that could be used in future work for the study of catalysis by metal complexes with tailored redox properties.

Taken together, these results demonstrate that half-sandwich rhodium complexes supported by non-symmetrically mono-substituted bpy derivatives are viable platforms for studying the impacts of distal ligand modification on redox behavior.

Acknowledgments

The authors thank Justin Douglas and Sarah Neuenswander for assistance with NMR spectroscopy, and Victor Day and Wade Henke for assistance with XRD analysis. This work was supported by the US National Science Foundation through award OIA-1833087. J.P.S. was supported by the Beckman Scholars Program at the University of Kansas, funded by the Arnold & Mabel Beckman Foundation.

Appendix 1

Synthetic Procedures

*Preparation of $Mn(CO)_3$(4,5-diazafluorene)Br (**2**)*

In the dark, to a 50 mL Schlenk flask equipped with a stir bar, was added 4,5-diazafluorene (0.064 g, 0.383 mmol) in 50 mL of diethyl ether. Then $Mn(CO)_5Br$ (0.100 g, 0.363 mmol) was added and the reaction was brought to reflux. The reaction was monitored by ^{1}H NMR until consumption of the starting material was observed to be complete, after approximately 3 hours. Once the reaction had reached completion, the Schlenk flask was placed into a refrigerator at –20 °C for 30 minutes. The resulting solid was then filtered off with a fritted glass funnel and washed with cold pentane to afford the title compound as a yellow solid. Yield: 0.088 g (62%). ^{1}H-NMR (CD_3CN, 500 MHz) δ 8.85 (d, $^3J_{H,H}$ = 5.3 Hz, 2H), 8.14 (d, $^3J_{H,H}$ = 7.6 Hz, 2H), 7.61-7.58 (dd, $^3J_{H,H}$ = 7.6 Hz, $^4J_{H,H}$ = 5.6 Hz, 2H), 4.29 (d, $^2J_{H,H}$ = 22.6 Hz, 2H) ppm. ^{13}C{^{1}H} NMR (176 MHz, CD3CN): δ 162.3, 151.3, 137.7, 136.5, 126.9, 37.6 ppm. ^{13}C{^{1}H}-DEPT-135 NMR δ 151.2, 136.4, 126.9, 37.5 ppm. Electronic absorption spectrum (MeCN): 230 (16000), 297 (9970), 301 (9910), 311 (10100), 320 (10400), 327 (10700), 410 nm (2200 M^{-1} cm^{-1}). IR (THF)): $\nu_{C=O}$ 2026 (m) (A'), $\nu_{C=O}$ 1938 (m) (A''), and $\nu_{C=O}$ 1917 (m) (A') cm^{-1}. ESI-MS (positive) m/z: 348.0 (98%)(**1**–Br^- +NCMe), 349.0 (18%), 350.0 (2%); 306.9 (29%) (**1**–Br^-), 307.9 (5%), 308.9 (0.5%); 305.0 (96%) (**1**–Br^-–3CO+2NCMe), 306.0 (18%); 264.0 (45%) (**1**–Br^-–3CO+NCMe), 265.0 (7%); 223.0 (100%) (**1**–Br^-–3CO), 224.0 (13%). Anal. Calcd. for $MnC_{14}H_8BrN_2O_3$: C, 43.44; H, 2.08; N, 7.24. Found: C, 43.38; H, 2.08; N, 7.14.

*Preparation of $Mn(CO)_3$(9,9´-dimethyl-4,5-diazafluorene)Br (**3**)*

In the dark, to a Schlenk flask equipped with a stir bar was added 9,9´-dimethyl-4,5-diazafluorene (0.075 g, 0.364 mmol) and 50 mL of diethyl ether. Then $Mn(CO)_5Br$ (0.100 g, 0.382 mmol) was added and the reaction was brought to reflux. The reaction was monitored by ^{1}H NMR until consumption of the starting material was observed to be complete, after approximately 3 hours. Once the reaction had reached completion the Schlenk flask was placed into a –20 °C refrigerator for 30 minutes. The resulting solid was then filtered off with a fritted glass funnel and washed with cold Et_2O to afford the title compound as a yellow solid. Yield: 0.110 g (73%). ^{1}H-NMR (CD_3CN, 500 MHz) δ 8.82 (d, $^3J_{H,H}$ = 5.3 Hz, 2H), 8.10 (d, $^3J_{H,H}$ = 7.7 Hz, 2H), 7.59 (dd, $^3J_{H,H}$ = 7.7 Hz, $^4J_{H,H}$ = 5.3 Hz, 2H), 1.66 (s, 3H), 1.58 (s, 3H) ppm. ^{13}C{^{1}H} NMR (176 MHz, CD_3CN): δ 160.3, 151.5, 147.2, 134.0, 127.5, 52.1, 25.3, 24.4 ppm. Electronic absorption spectrum (MeCN): 236 (15000), 301 (11000), 306 (11000), 316 (11600), 324 (12000), 332 (13000), 411 nm (3300 M^{-1} cm^{-1}). IR (THF): $\nu_{C=O}$ 2026 (m) (A'), $\nu_{C=O}$ 1938 (m) (A''), and $\nu_{C=O}$ 1915 (m) (A') cm^{-1}. ESI-MS (positive) m/z: 251.0 (100%)(**1**–Br^-–3CO), 252.0 (15%), 253.0 (1%). Anal. Calcd. for $MnC_{16}H_{12}BrN_2O_3$: C, 46.29; H, 2.91; N, 6.75. Found: C, 46.35; H, 3.03; N, 6.97.

*Preparation of [Tris(9,9´-dimethyl-4,5-diazafluorene)Ruthenium]$(PF_6)_2$ (**5**)*

In the dark, to a three-neck round bottom flask equipped with a stir bar was added 9,9´-dimethyl-4,5-diazafluorene (0.100 g, 0.509 mmol), $RuCl_3$ xH_2O (0.027 g, 0.128 mmol), and Zn^0 powder (0.042 g, 0.642 mmol). A 2:1 ethanol:water mixture was used as a solvent to suspend the material, the reaction mixture was brough to reflux, and was allowed to stir overnight. The resulting bright-orange solution was then filtered into a flask containing ammonium

hexafluorophosphate (0.044 g, 0.269 mmol), which resulted in immediate precipitation of the desired product. The precipitate was filtered, and then washed progressively with cold water and diethyl ether. The desired complex was purified by recrystallization from boiling methanol to afford an orange solid. Yield (0.021 g, 17%). ^{1}H-NMR (CD_3CN, 400 MHz) δ 8.06 (dd, $^{3}J_{H,H}$ = 7.8 Hz, $^{4}J_{H,H}$ = 0.9 Hz, 6H), 7.81 (dd, $^{3}J_{H,H}$ = 5.5 Hz, $^{4}J_{H,H}$ = 0.9 Hz, 6H), 7.44 (dd, $^{3}J_{H,H}$ = 7.8 Hz, $^{4}J_{H,H}$ = 5.5 Hz, 6H), 1.68 (s, 18H) ppm.^{13}C{^{1}H} NMR (176 MHz, CD3CN): δ 162.8, 152.9, 147.4, 133.4, 127.9, 53.2, 24.5 ppm. ^{19}F NMR (276 MHz, CD_3CN): δ -72.9 (d, 706.4 Hz) ppm.^{31}P NMR (162 MHz, CD_3CN): δ -144.7 (m, 706.4 Hz) ppm. Electronic absorption spectrum (MeCN): 231 (27000), 249 (14400), 256 (13500), 295 (75000), 445 nm (17000 M^{-1} cm^{-1}). Anal. Calcd. for $RuC_{29}H_{36}N_6F_{12}P_2$: C, 47.81; H, 3.70; N, 8.58. Found: C, 47.62; H, 3.70; N, 8.30.

*Preparation of 9,9´-dibenzyl-1-N-benzyl-4,5-diazafluorenium bromide (**Bn_3daf**)*

To a Schlenk flask equipped with a stir bar was added 4,5-diazafluorene (0.500 g, 2.973 mmol). The flask was then put under nitrogen and purged. The 4,5-diazafluorene was then dissolved in dry tetrahydrofuran, which was added by canula transfer. The solution was then cooled to –10 °C using an ice and acetone bath. Potassium *tert*-butoxide (1.001 g, 8.918 mmol) was added to the reaction flask and the mixture was allowed to stir for 30 minutes. Next, benzyl bromide (2.021 g, 11.891 mmol) was added to the reaction flask. The reaction was brought to room temperature and allowed to stir for 3 hours. The reaction mixture was then extracted with ethyl acetate and saturated sodium carbonate, dried with anhydrous magnesium sulfate, filtered, and the desired product dried *in vacuo* to yield a sizeable quantity of pure solid. ^{1}H-NMR (CD_3CN, 400 MHz) δ 9.53 (d, $^{3}J_{H,H}$ = 6.3 Hz, 1H), 8.81 (d, $^{3}J_{H,H}$ = 7.9 Hz, 1H), 8.71 (dd, $^{3}J_{H,H}$ = 4.7 Hz, $^{4}J_{H,H}$ =

1.5 Hz, 1H), 8.15 (m, 2H) 7.62 (dd, $^{3}J_{H,H}$ = 7.9 Hz, $^{4}J_{H,H}$ = 4.7 Hz, 1H), 7.23 (d, $^{3}J_{H,H}$ = 7.4 Hz, 1H), 7.16 (t, $^{3}J_{H,H}$ = 7.7 Hz, 2H), 7.06 (t, $^{3}J_{H,H}$ = 7.5 Hz, 2H), 6.95 (t, $^{3}J_{H,H}$ = 7.7 Hz, 4H), 6.88 (d, $^{3}J_{H,H}$ = 7.3 Hz, 2H), 6.81 (s, 2H), 6.59 (d, $^{3}J_{H,H}$ = 8.3 Hz, 4H), 3.72 (d, $^{3}J_{H,H}$ = 13.6 Hz, 2H), 3.59 (d, $^{3}J_{H,H}$ = 13.6 Hz, 2H). ESI-MS (positive) m/z: 439.2169 (100%), 440.2213 (37%), 441.2245 (7%).

NMR Spectra

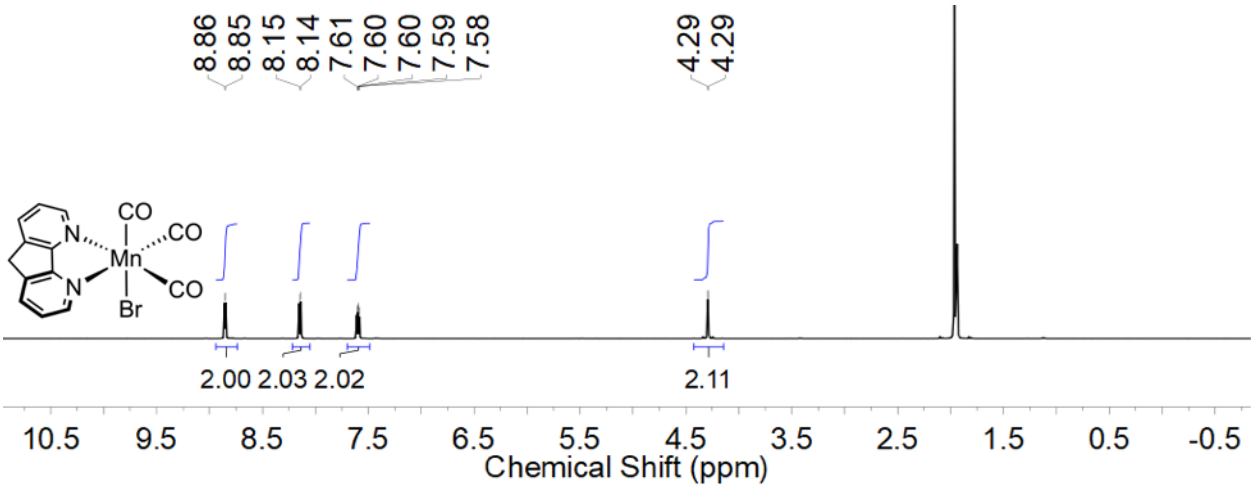

Figure S1: ^{1}H-NMR spectrum (500 MHz, CD_3CN) of **2**.

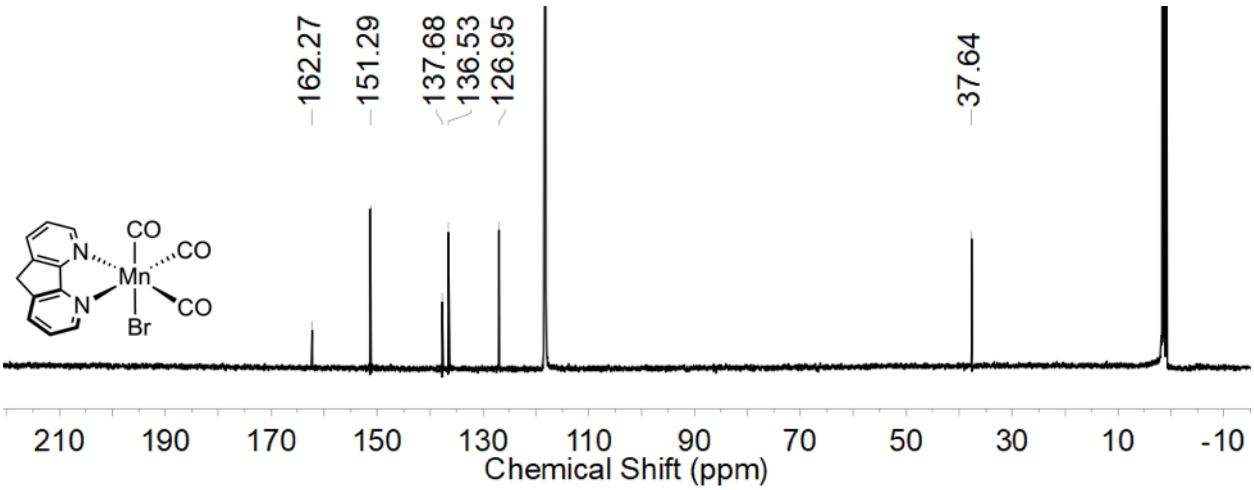

Figure S2: $^{13}C\{^{1}H\}$-NMR spectrum (126 MHz, CD_3CN) of **2**.

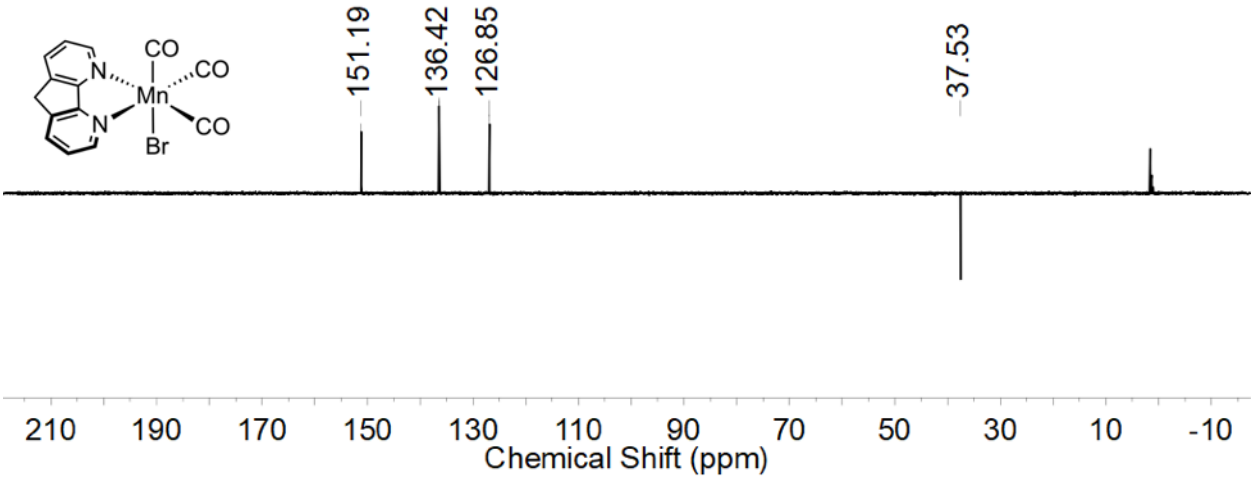

Figure S3: $^{13}C\{^{1}H\}$ DEPT-NMR spectrum (126 MHz, CD_3CN) of **2**.

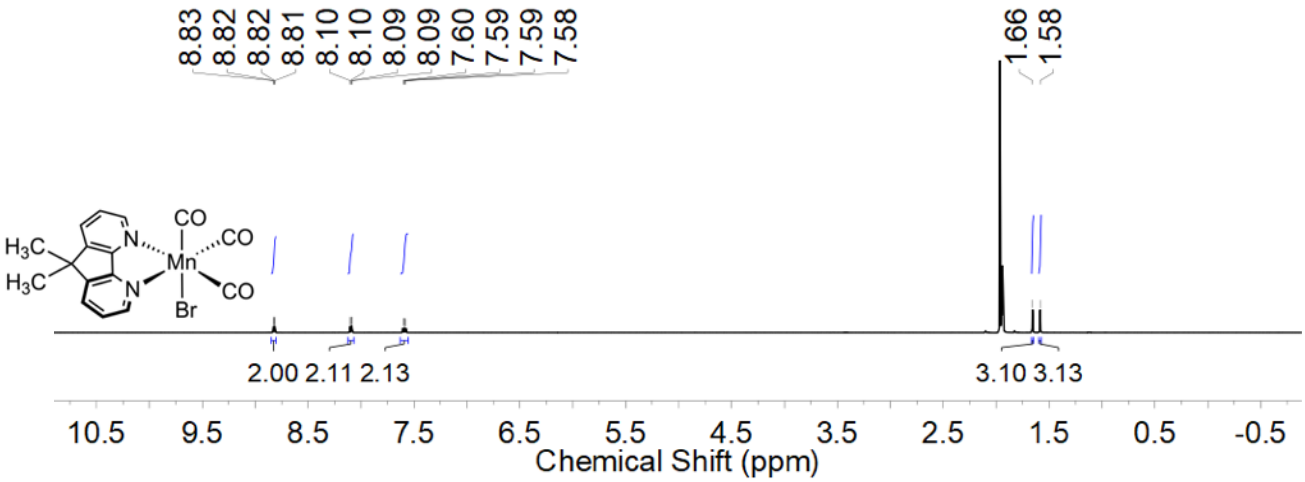

Figure S4: ^{1}H-NMR spectrum (400 MHz, CD_3CN) of **3**.

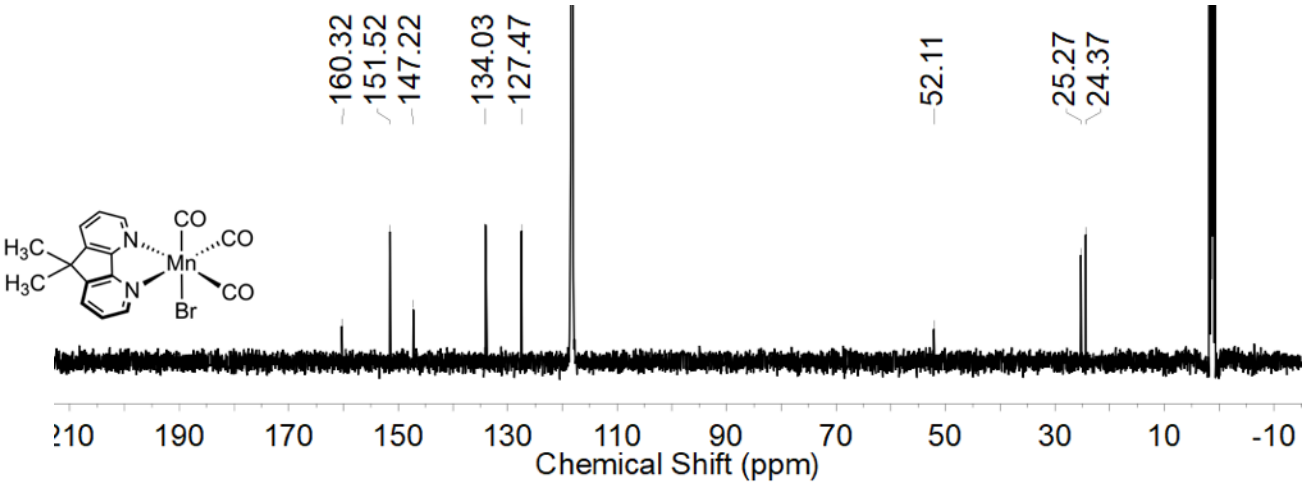

Figure S5: $^{13}C\{^{1}H\}$-NMR spectrum (126 MHz, CD_3CN) of **3**.

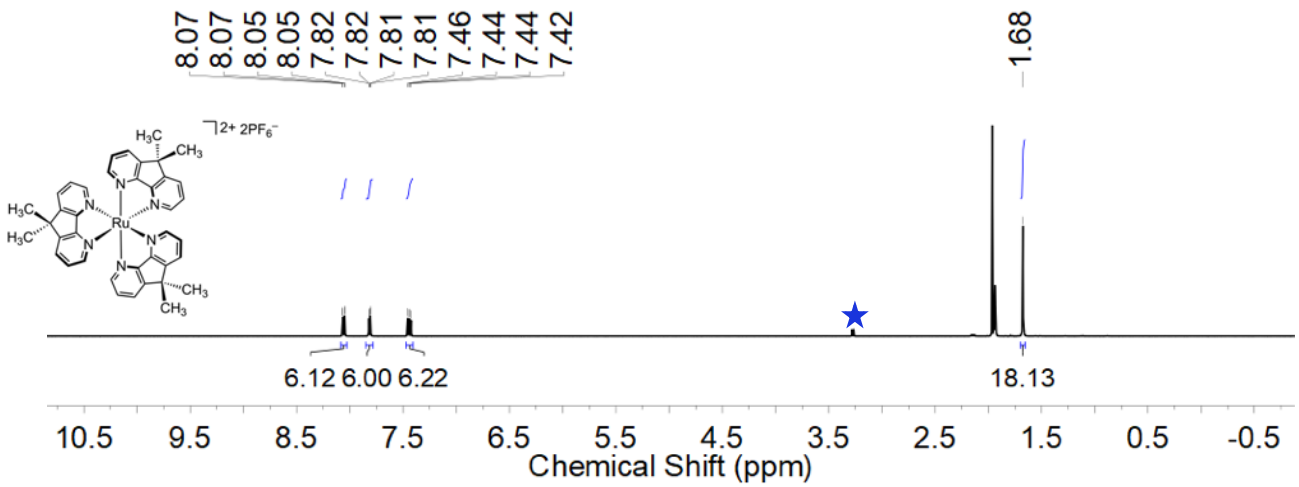

Figure S6: ^{1}H-NMR spectrum (500 MHz, CD_3CN) of **5**; The blue star (★) corresponds to adventitious methanol.

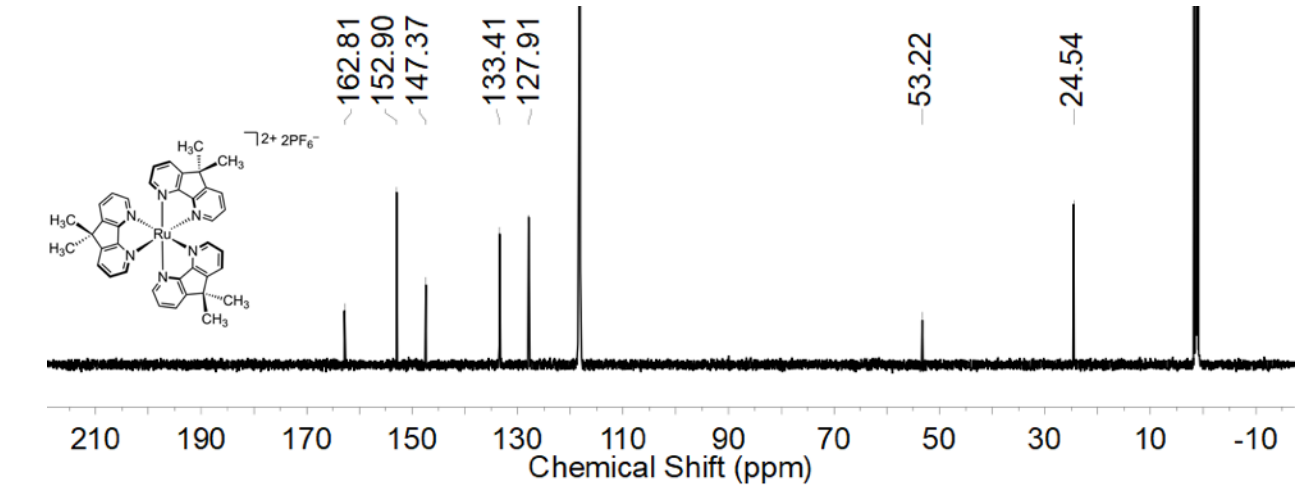

Figure S7: $^{13}C\{^{1}H\}$-NMR spectrum (126 MHz, CD_3CN) of **5**.

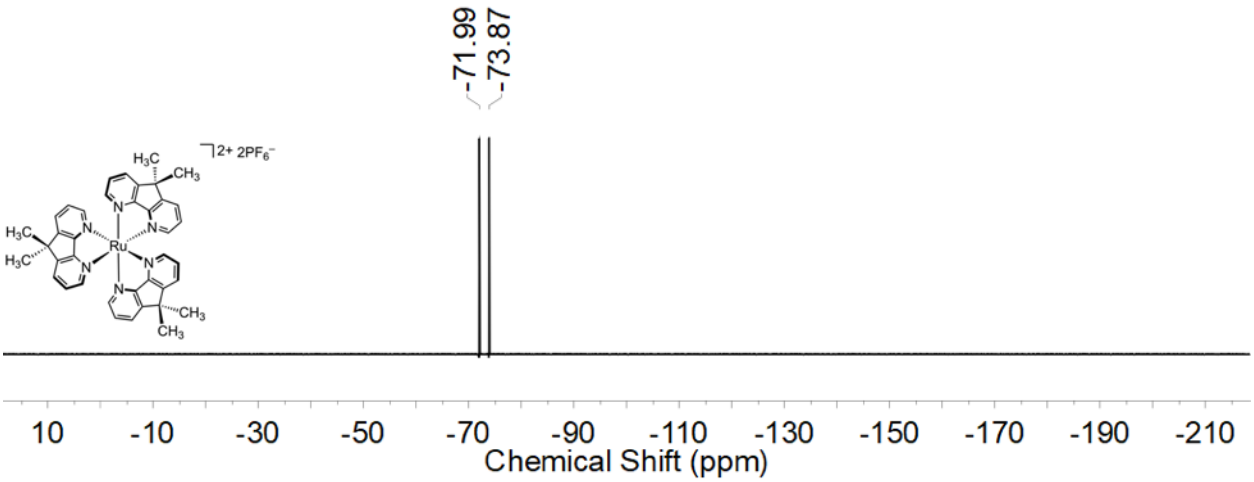

Figure S8: ^{19}F-NMR spectrum (376 MHz, CD_3CN) of **5**.

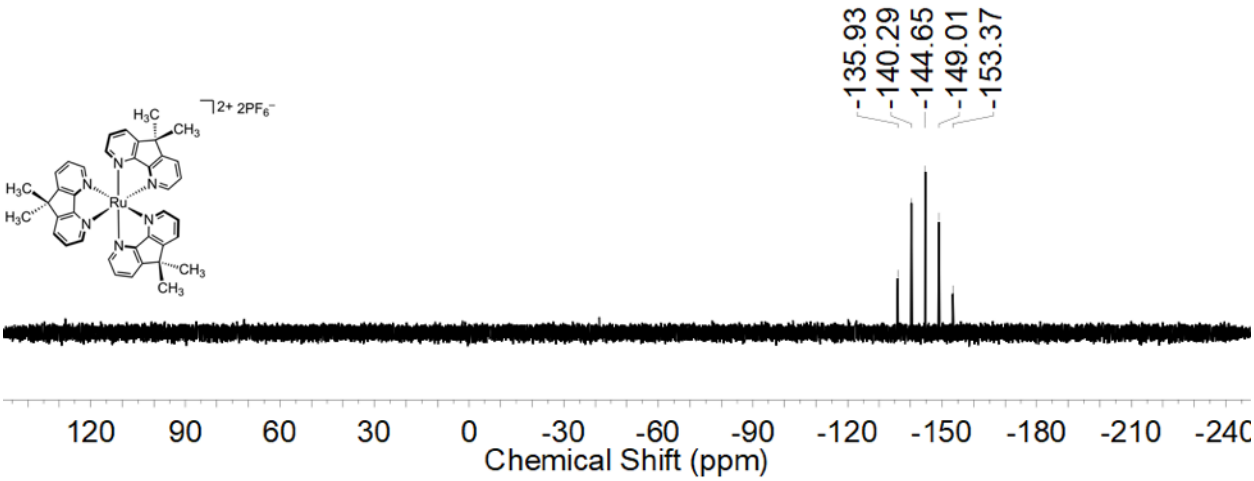

Figure S9: ^{31}P-NMR spectrum (162 MHz, CD_3CN) of **5**.

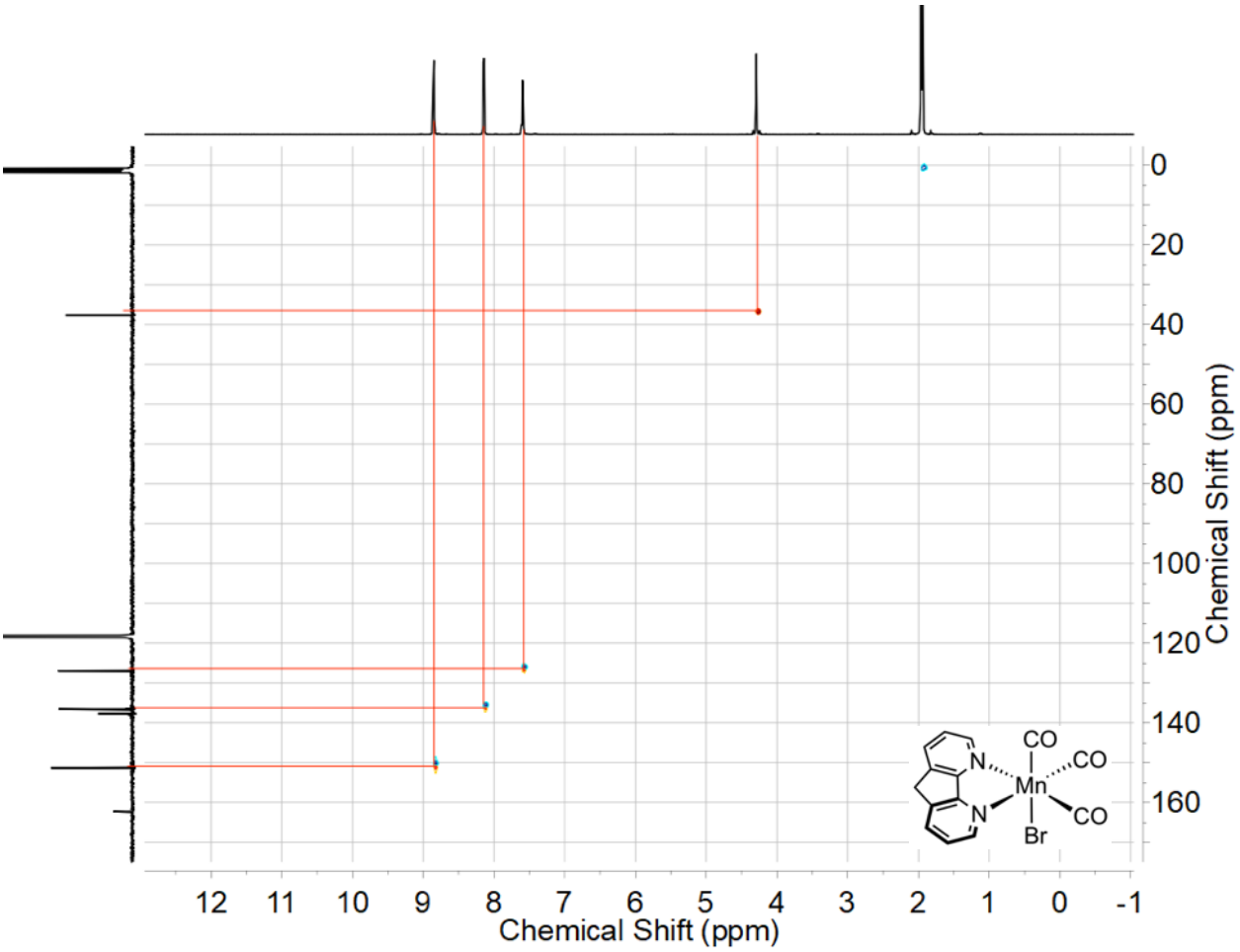

Figure S10: ^{1}H-^{13}C HSQC of complex **2** in CD_3CN depicting the methylene protons indicated by the opposite phasing (red) compared to the methyl and methine protons (blue).

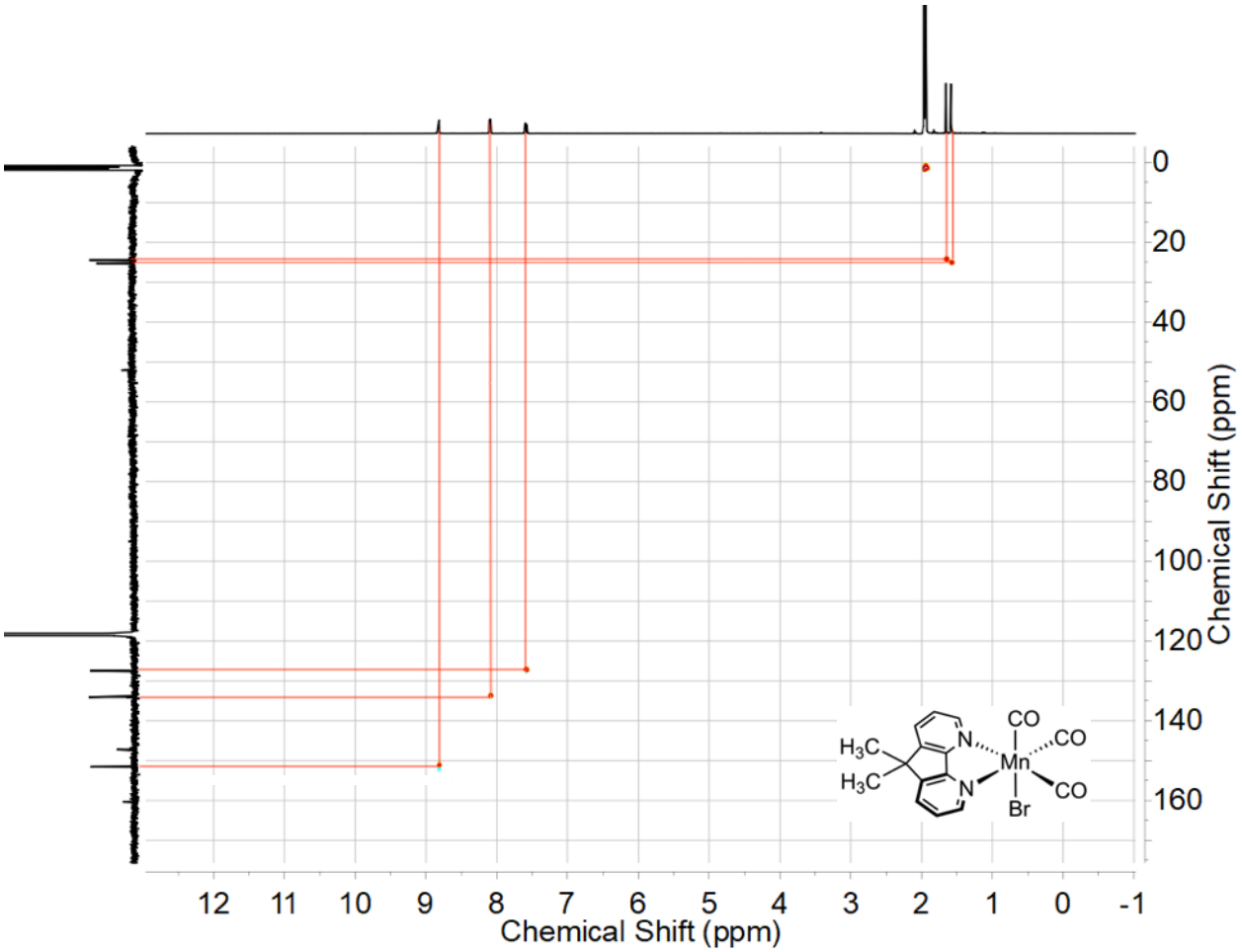

Figure S11: ^{1}H-^{13}C HSQC of complex **3** in CD_3CN depicting the diastereotopic methyl groups. Methyl and methine protons (red) and methylene protons (blue).

IR Spectra

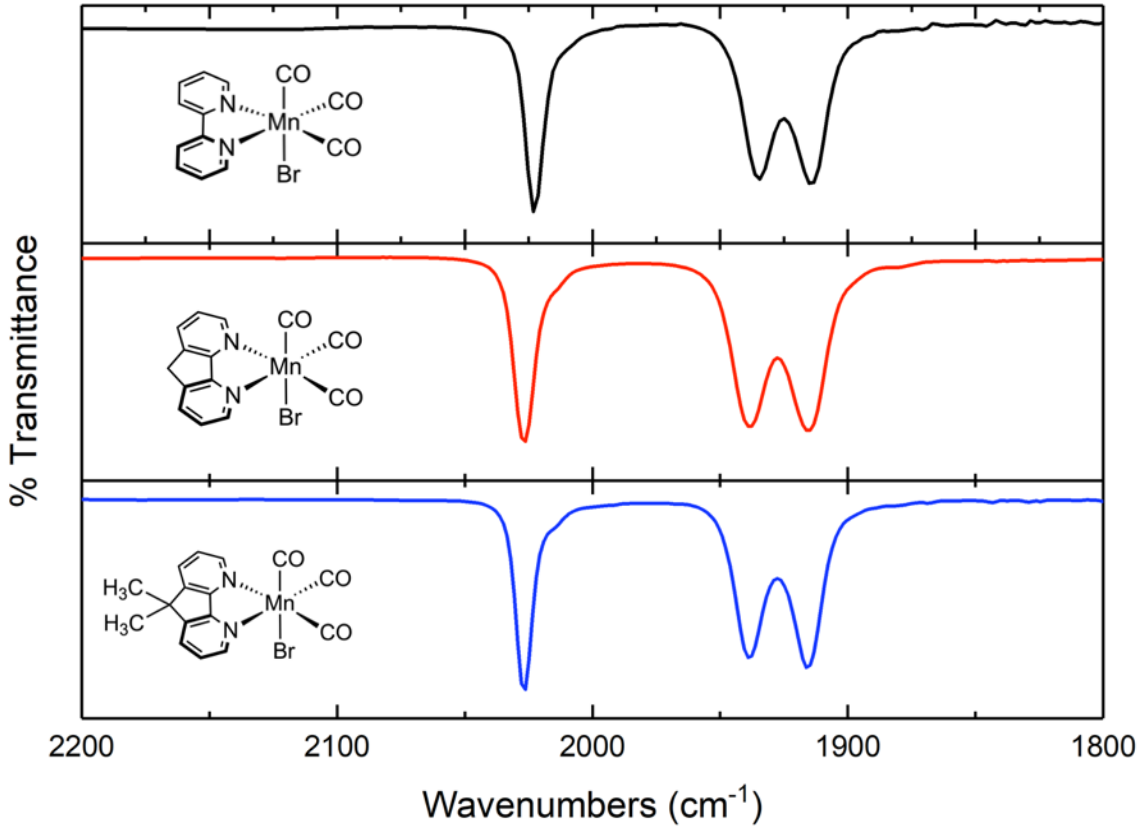

Figure S12: IR spectra of the carbonyl stretches for **1**, **2**, and **3** in THF solution; focusing on the CO stretching region. For a *fac*-tricarbonyl, C_s symmetric molecule, three CO stretches (Γ_{CO} = 2A′+A″) would be expected and are observed for complexes **1, 2,** and **3.**

Mass Spectra

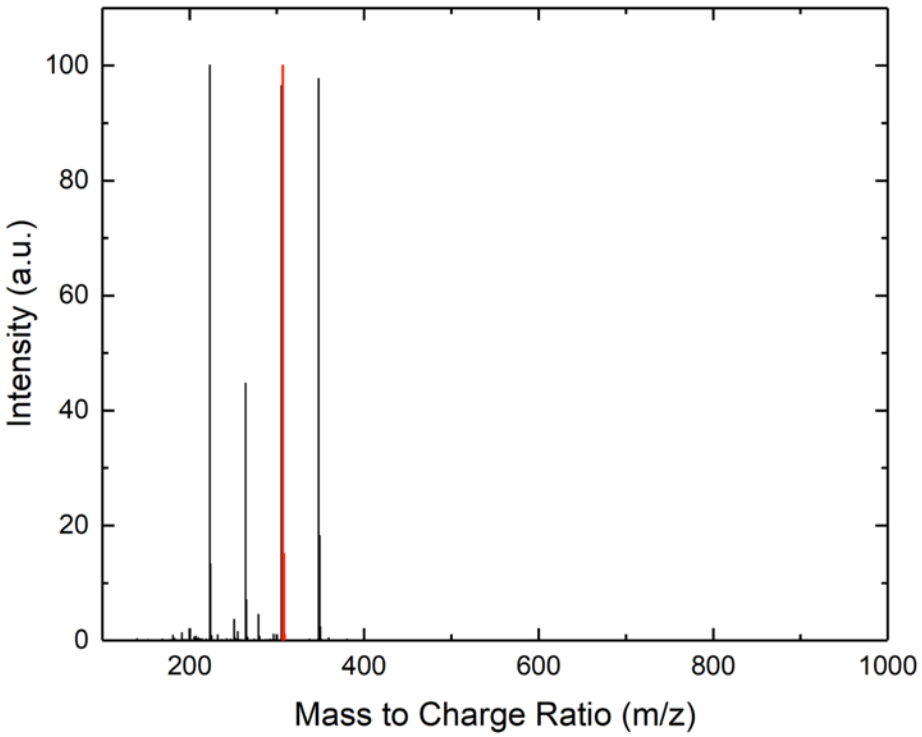

Figure S13: Full ESI-Mass spectrum of **2**. The experimental data is shown in **black** and the predicted data is shown in **red**. The other peaks in the spectrum correspond to fragments that are identified below.

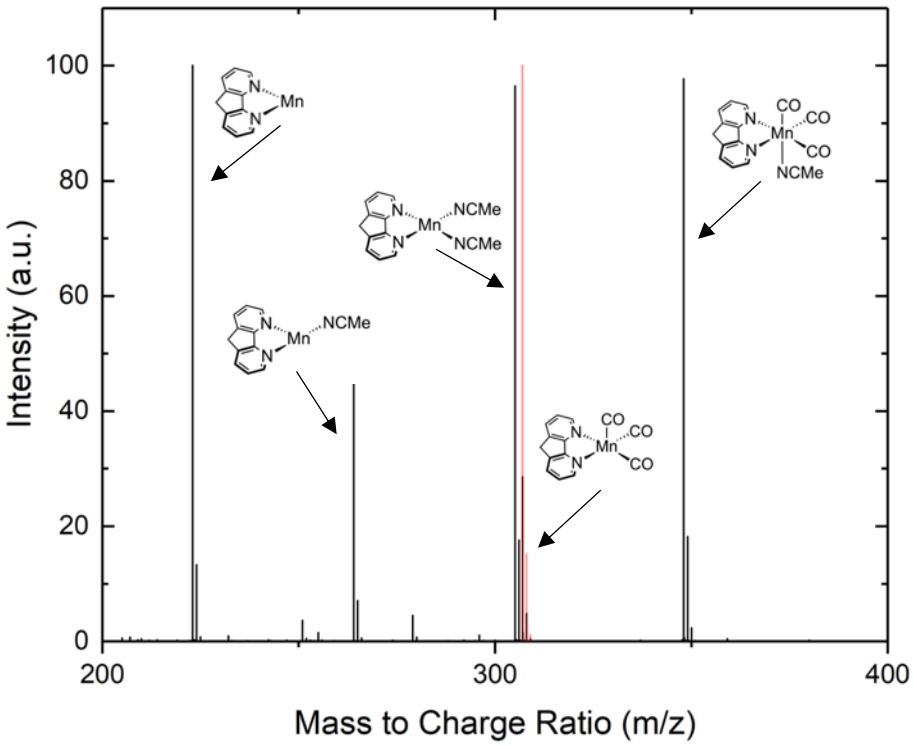

Figure S14: Zoomed in mass spectrum of **2** with fragment assignment. The experimental data is shown in **black** and the predicted data is shown in **red**.

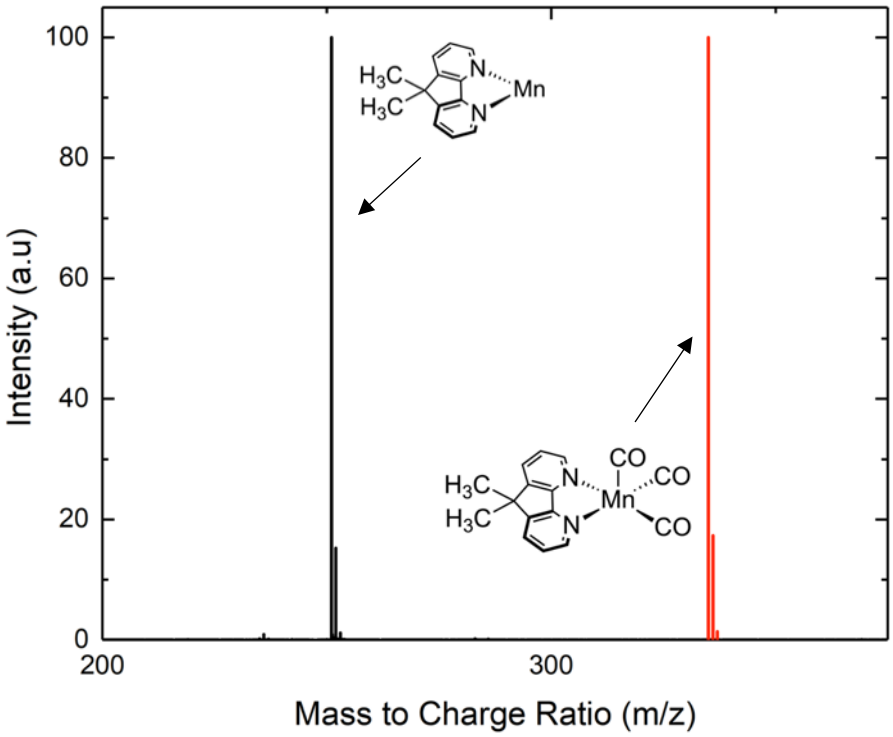

Figure S15: Full ESI-Mass spectrum of **3**. The experimental data is shown in **black** and the predicted data is shown in **red**. The expected parent peak was not present, but a corresponding fragment is identified in Figure S16.

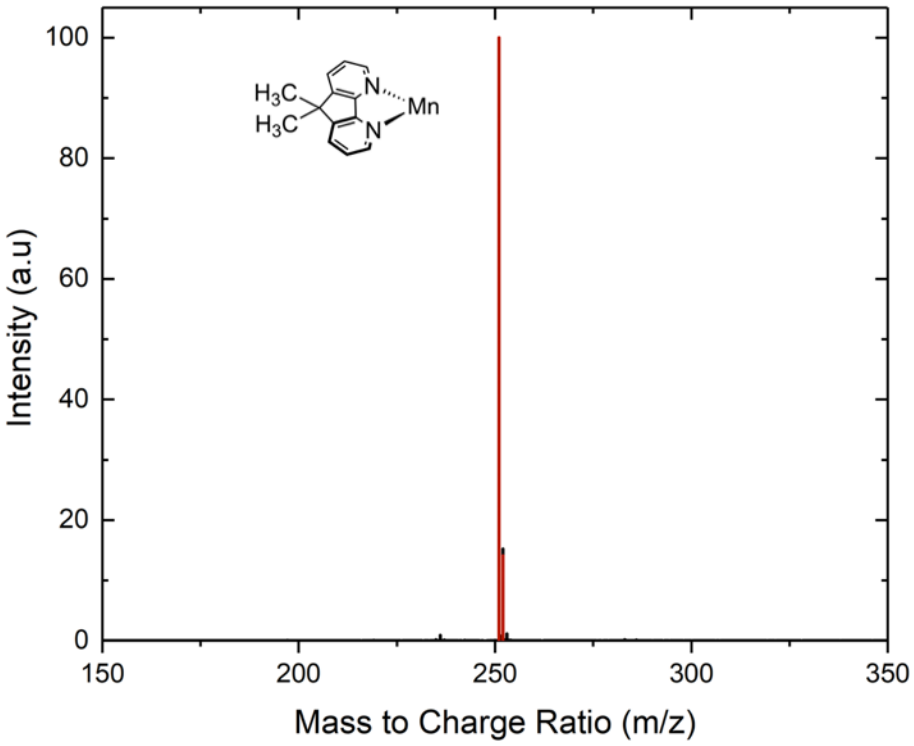

Figure S16: Zoomed in mass spectrum of **3** with fragment assignment. The experimental data is shown in **black** and the predicted data is shown in **red** for this specific fragment.

Electronic Absorption Spectra

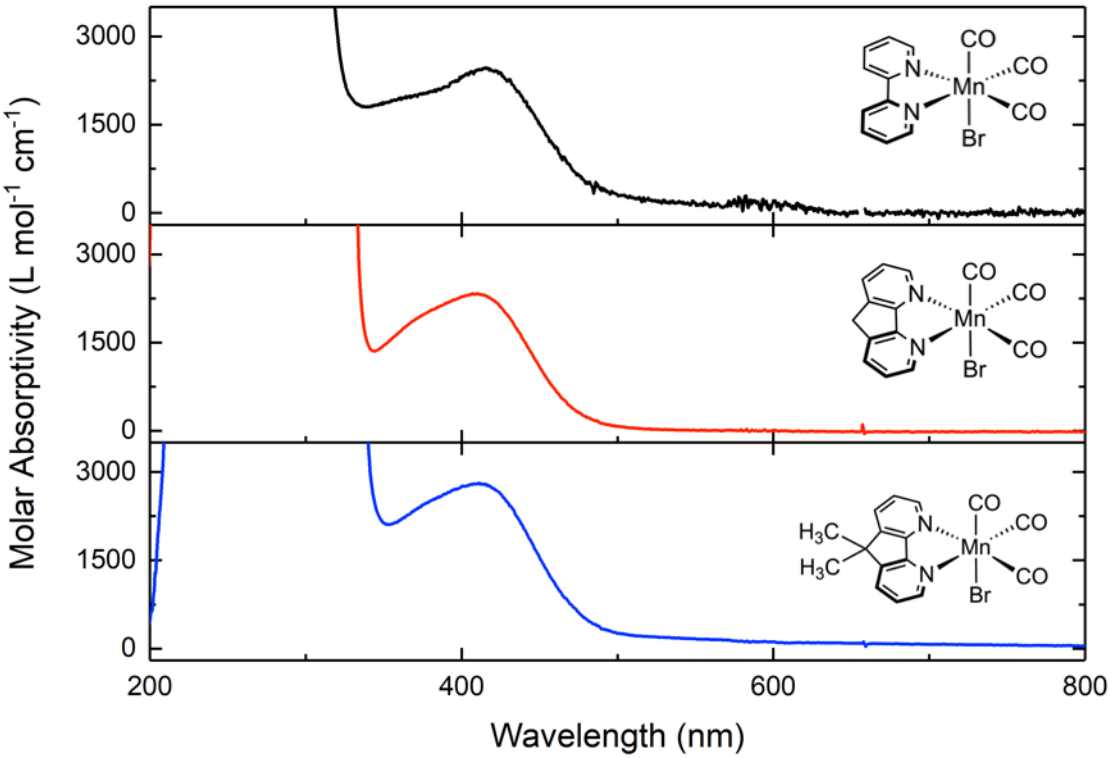

Figure S17: Stacked electronic absorption spectrum of **1**, **2**, and **3** featuring the MLCT transition in the visible region.

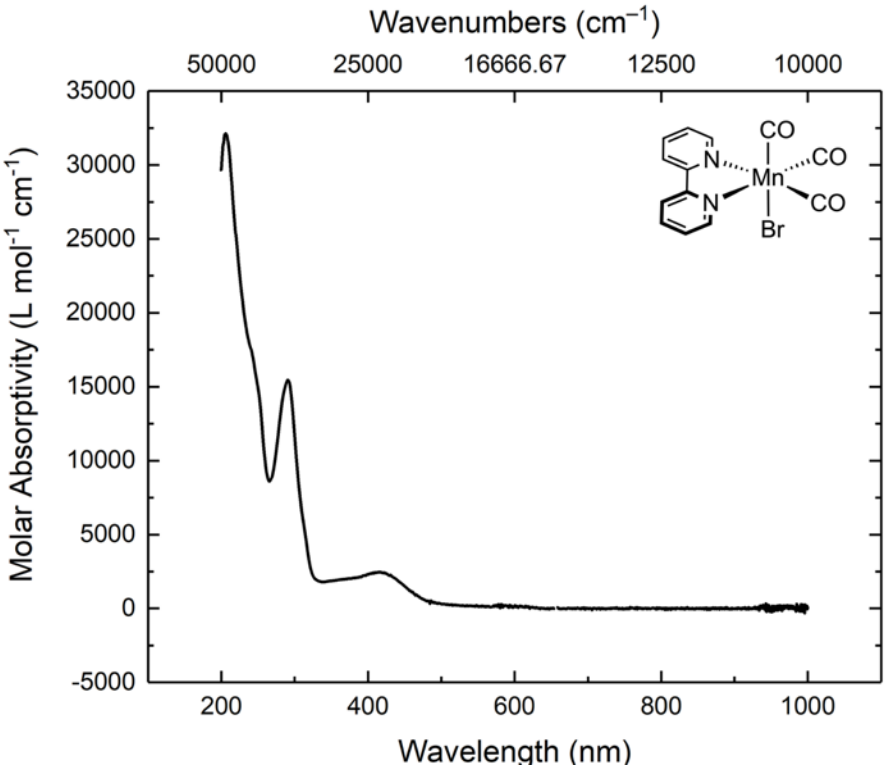

Figure S18: Electronic absorption spectrum of **1** in MeCN**.**

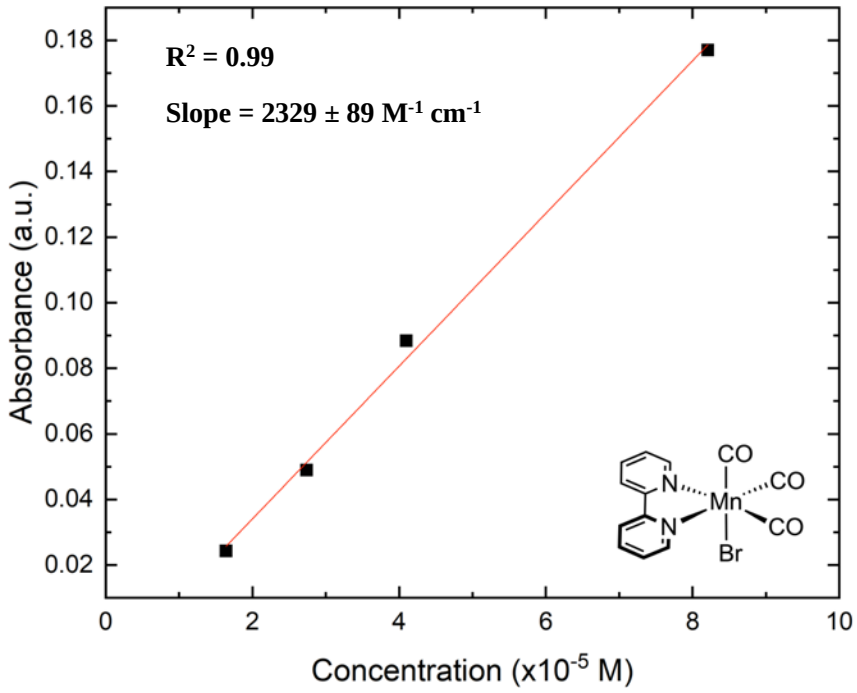

Figure S19: Absorbance vs. concentration plot of complex **1** in MeCN to obtain the molar absorptivity.

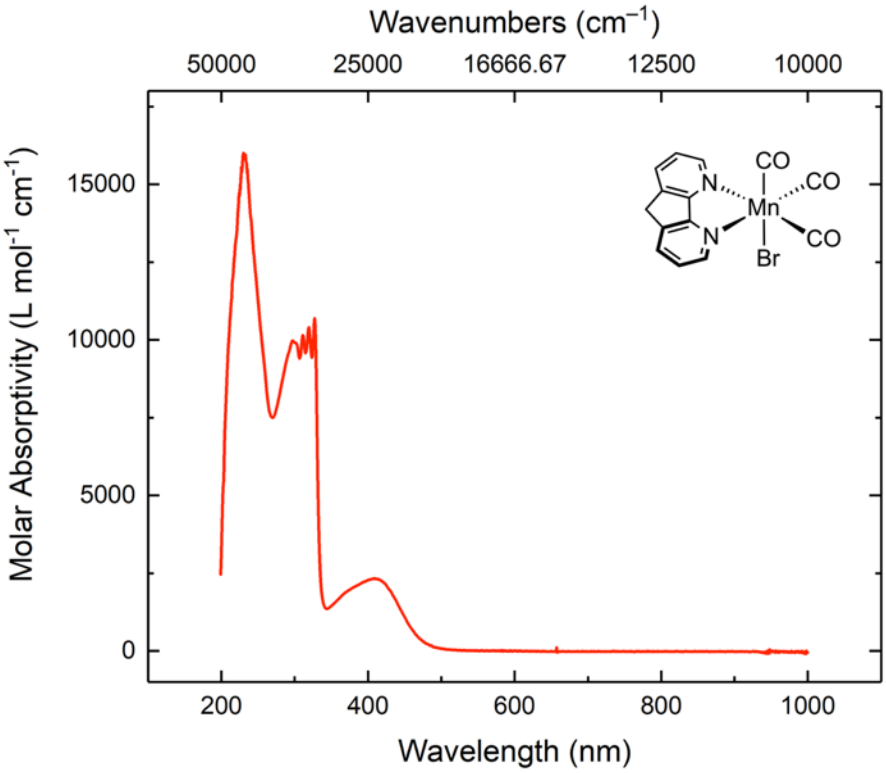

Figure S20: Electronic absorption spectrum of **2** in MeCN**.**

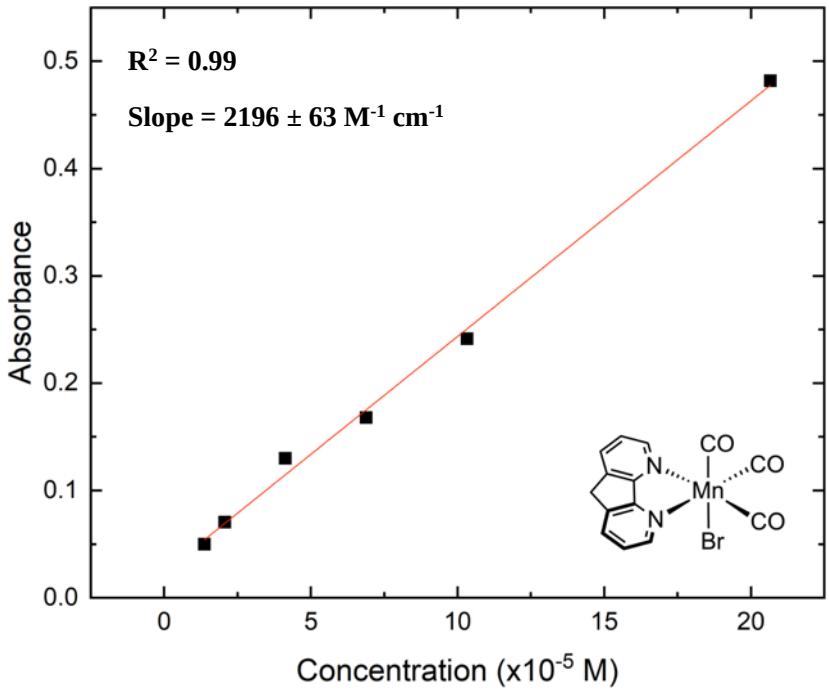

Figure S21: Absorbance vs. concentration plot of complex **2** in MeCN to obtain the molar absorptivity.

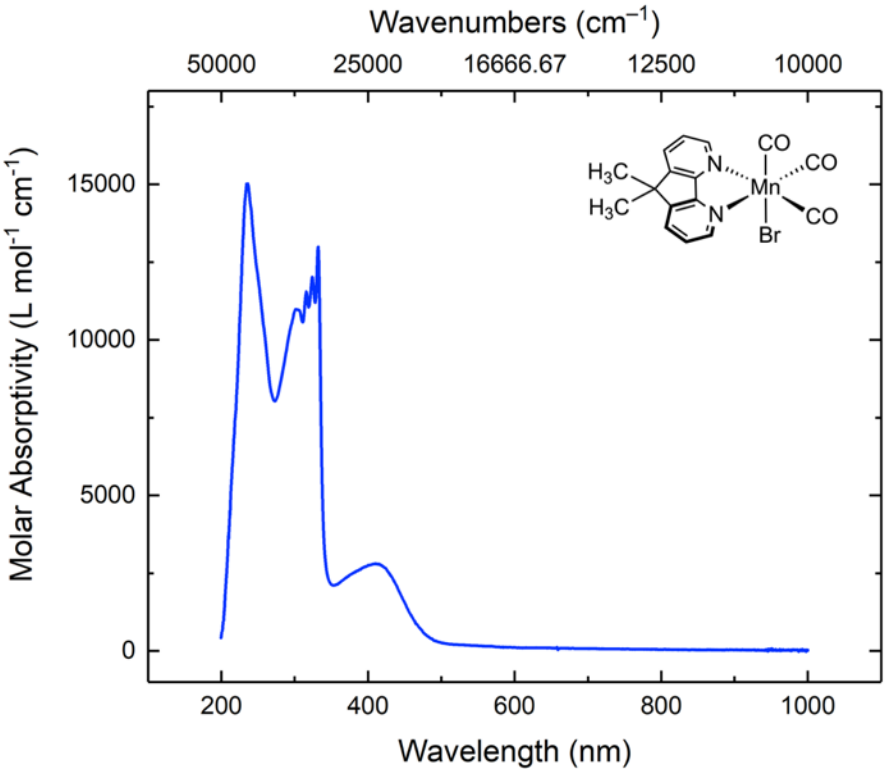

Figure S22: Electronic absorption spectrum of **3** in MeCN**.**

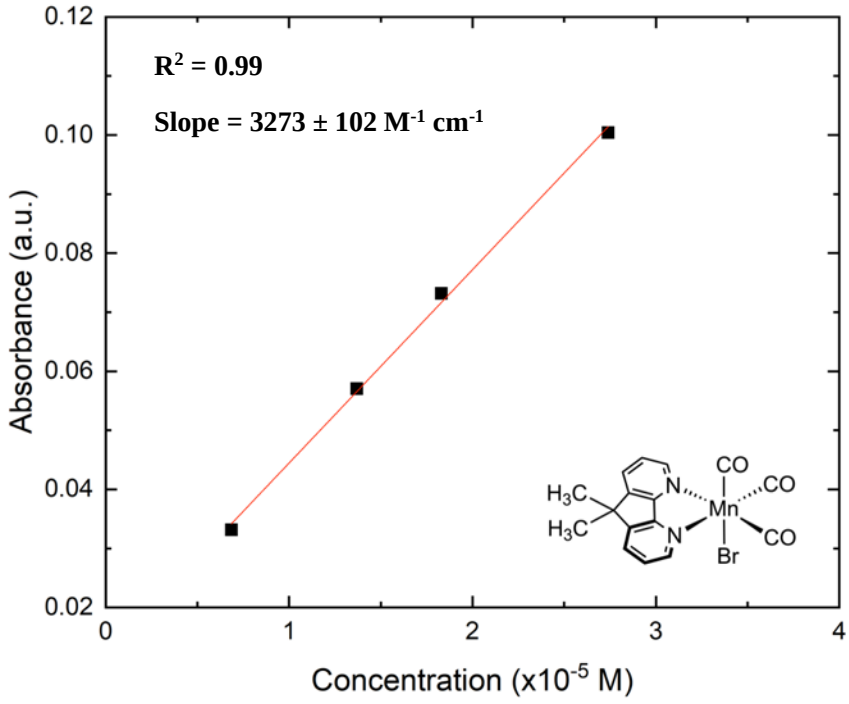

Figure S23: Absorbance vs. concentration plot of complex **3** in MeCN to obtain the molar absorptivity.

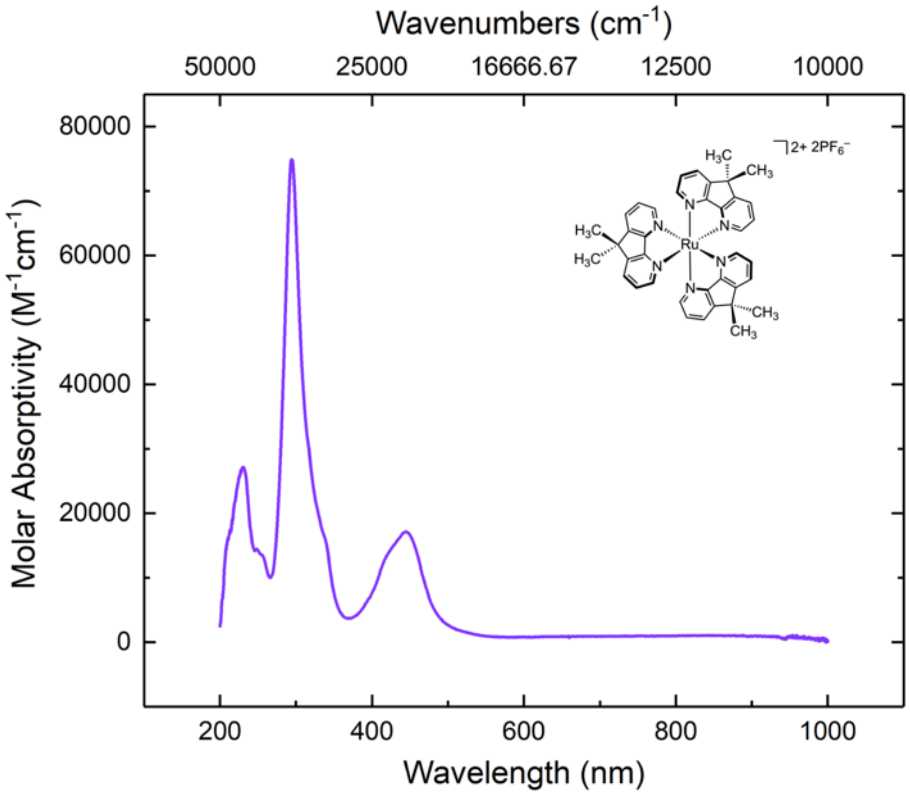

Figure S24: Electronic absorption spectrum of **5** in MeCN**.**

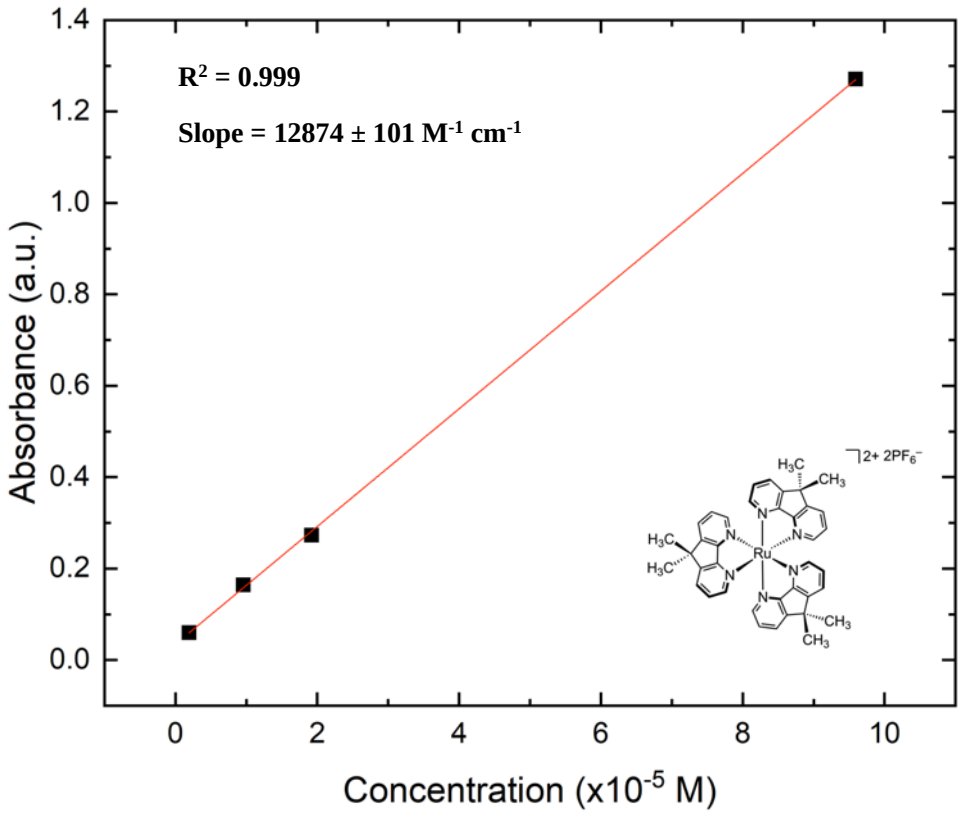

Figure S25: Absorbance vs. concentration plot of complex **5** in MeCN to obtain the molar absorptivity.

Cyclic Voltammetry Data

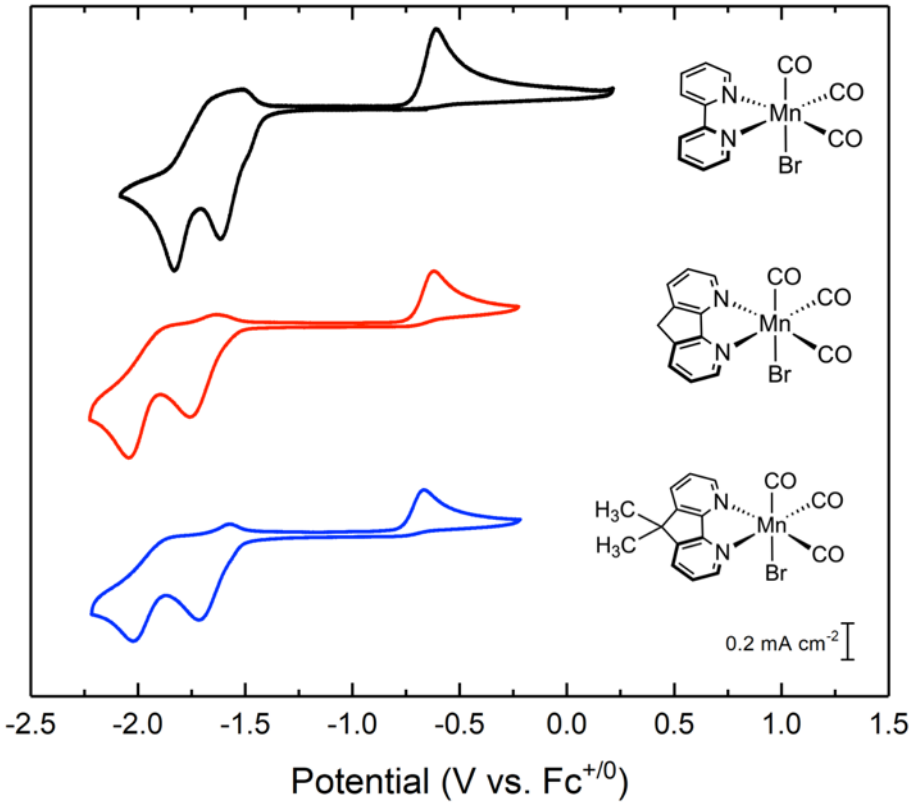

Figure S26: Stacked cyclic voltammograms of **1**, **2**, and **3** in 0.1 M $TBAPF_6$/MeCN solution.

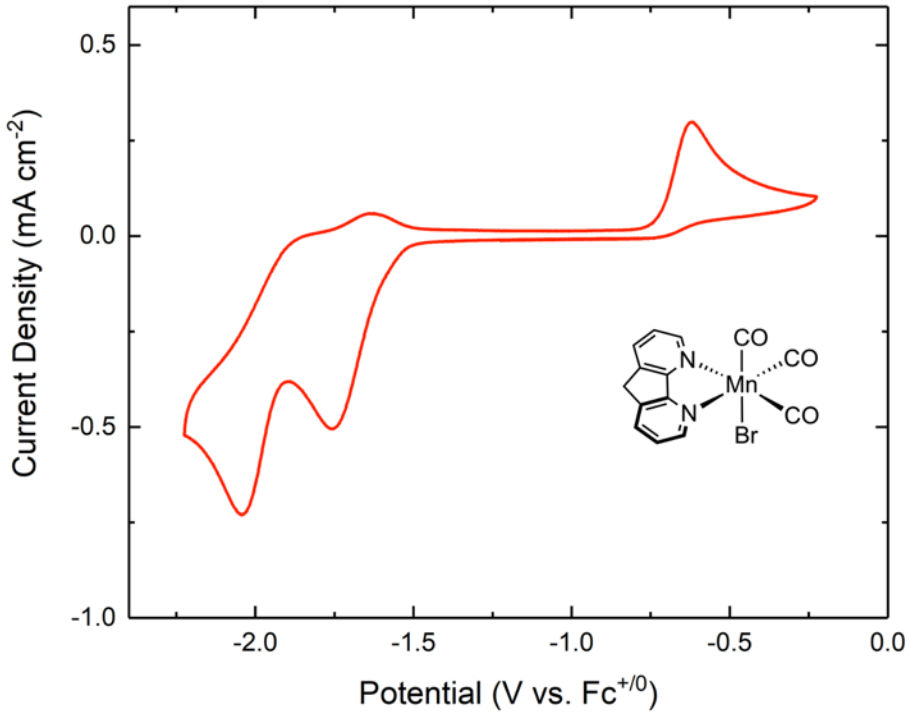

Figure S27: Cyclic voltammogram of **2** in 0.1M $TBAPF_6$/MeCN solution.

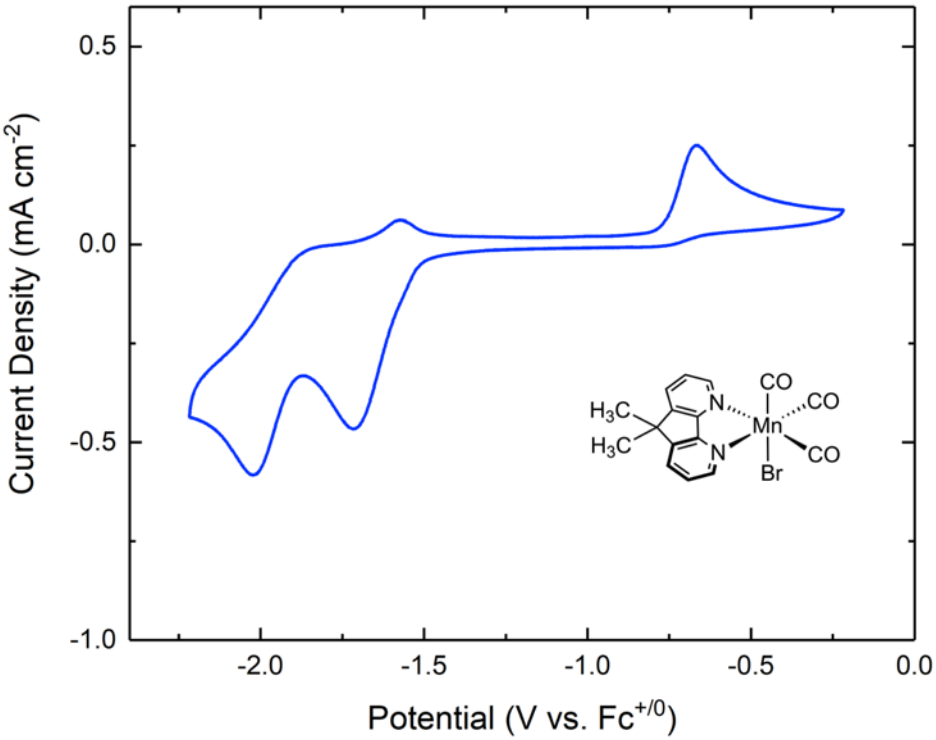

Figure S28: Cyclic voltammogram of **3** in 0.1M $TBAPF_6$/MeCN solution.

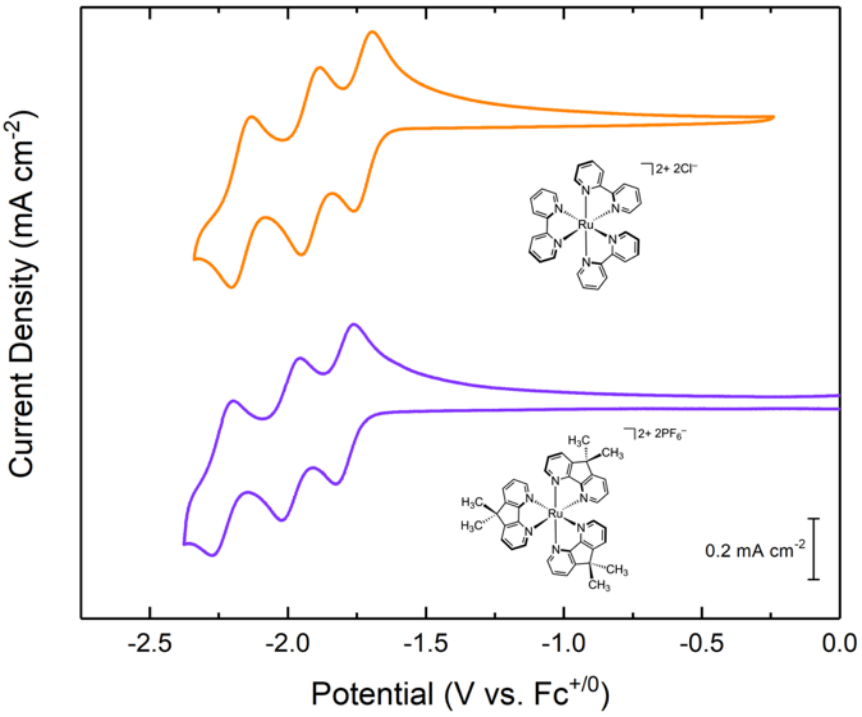

Figure S29: Stacked cyclic voltammograms of **4** and **5** in 0.1M $TBAPF_6$/MeCN solution.

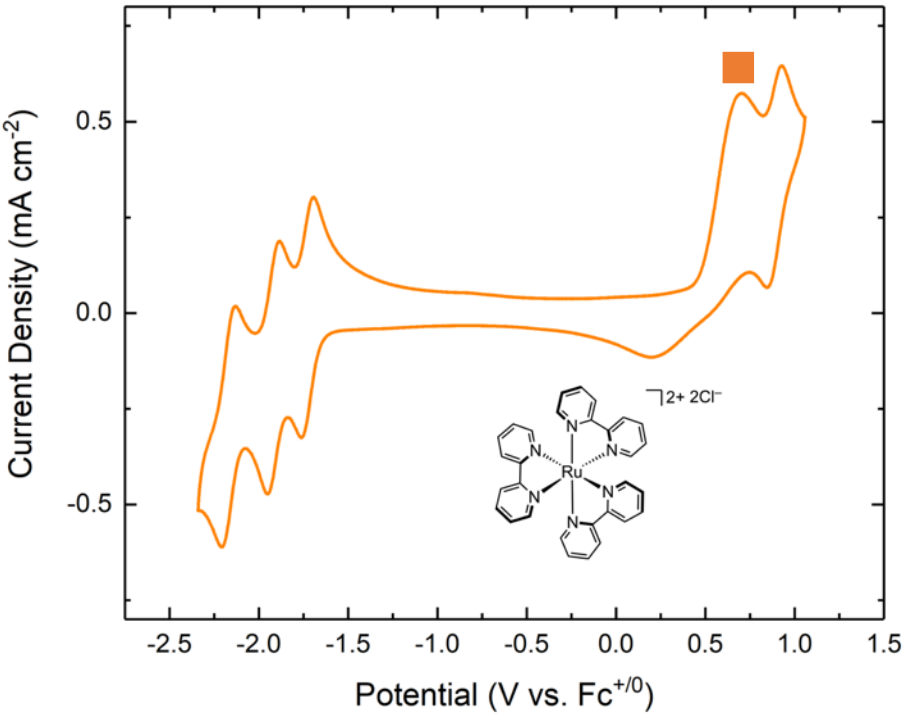

Figure S30: Cyclic voltammograms of **4** in 0.1M $TBAPF_6$/MeCN solution. The orange square (■) indicates chloride oxidation, which is a result of follow up chemical reactivity observed upon reduction.

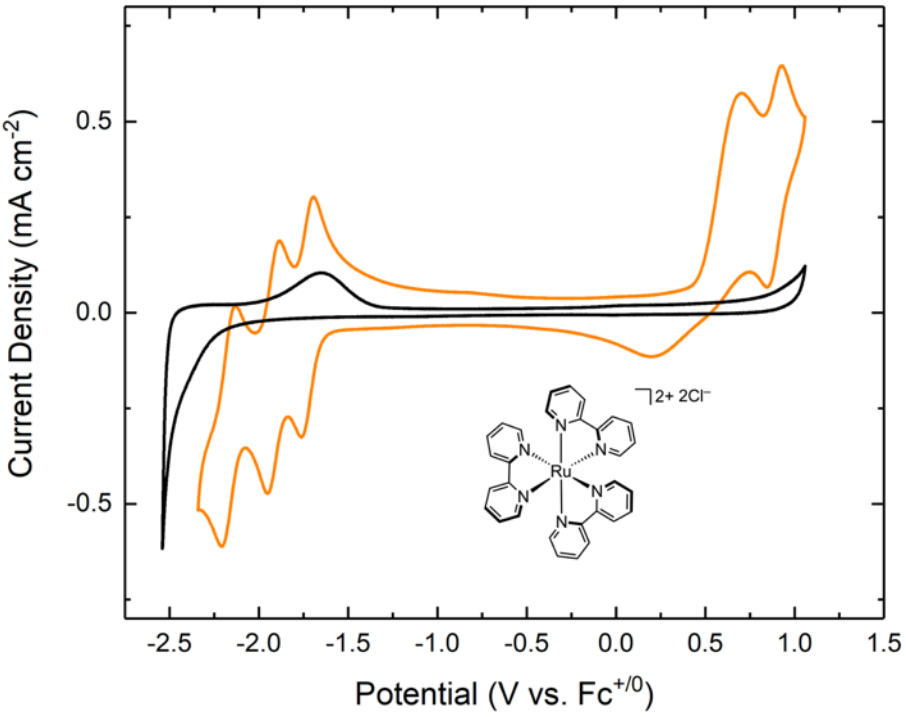

Figure S31: Cyclic voltammograms of **4** overlaid with **blank** in 0.1M $TBAPF_6$/MeCN solution.

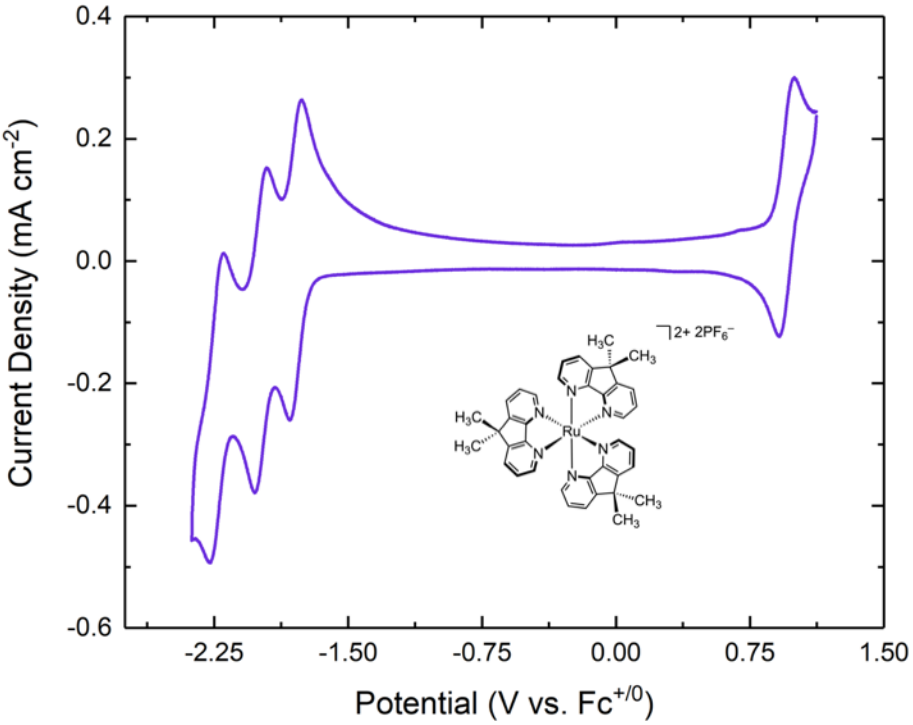

Figure S32: Cyclic voltammograms of **5** in 0.1M $TBAPF_6$/MeCN solution.

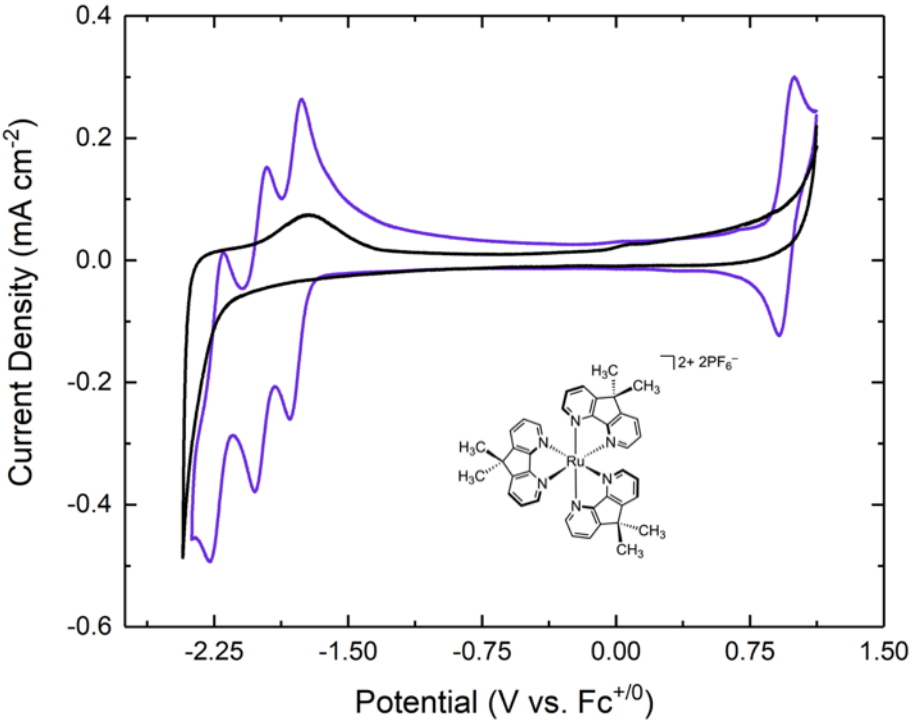

Figure S33: Cyclic voltammogram of **5** overlaid with a **blank** in 0.1M $TBAPF_6$/MeCN solution.

Cyclic Voltammetry with Acid Data

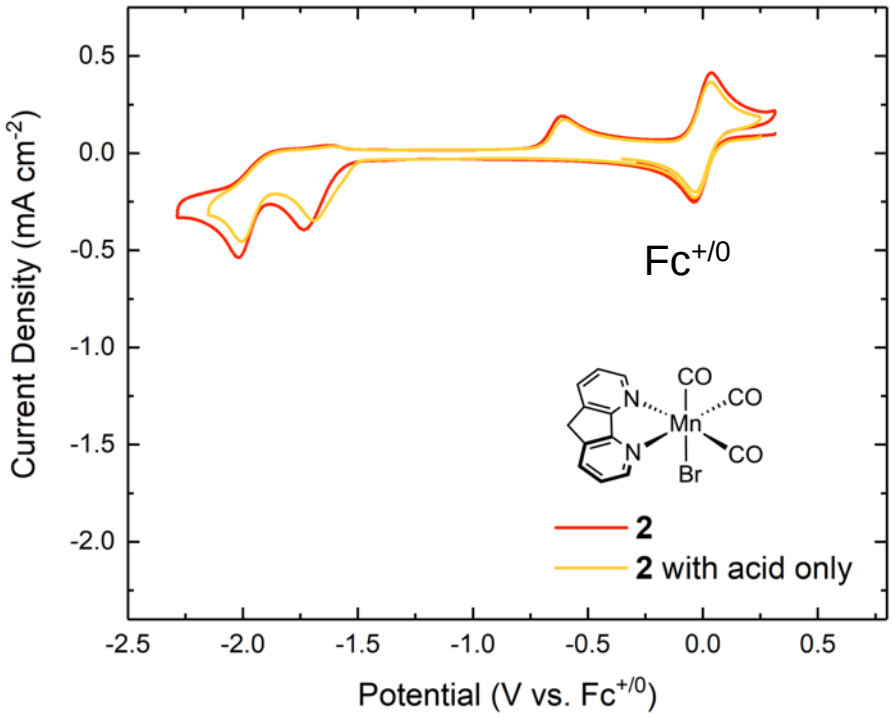

Figure S34: Cyclic voltammetry of **2** (red) in 0.1M $TBAPF_6$/MeCN solution followed by the addition of a 5% H_2O solution (yellow). The diminished current density is a result of dilution.

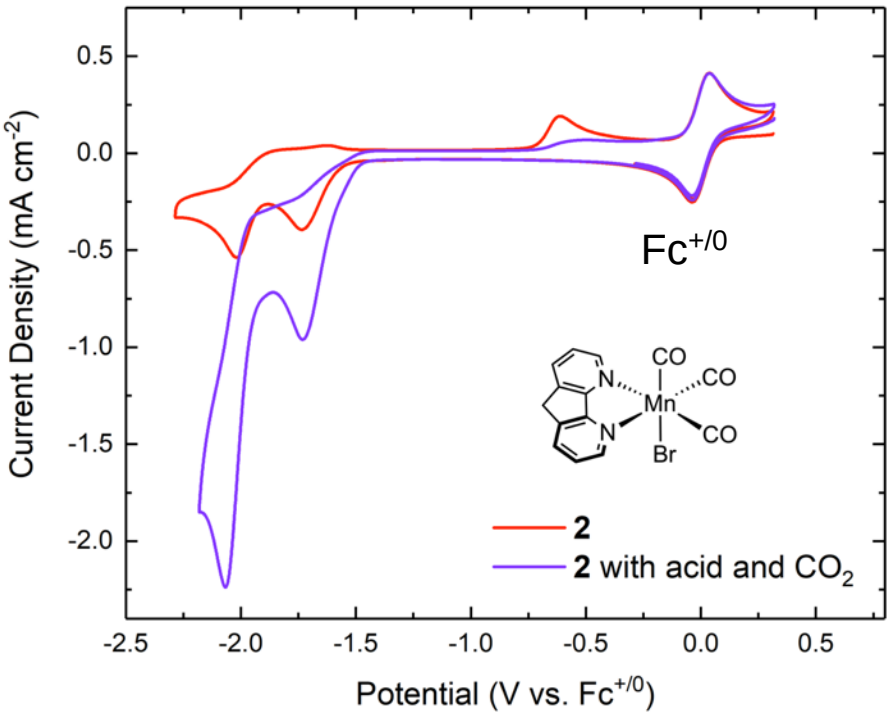

Figure S35: Cyclic voltammetry of **2** (red) in the presence of a 5% H_2O solution and a CO_2 atmosphere (purple).

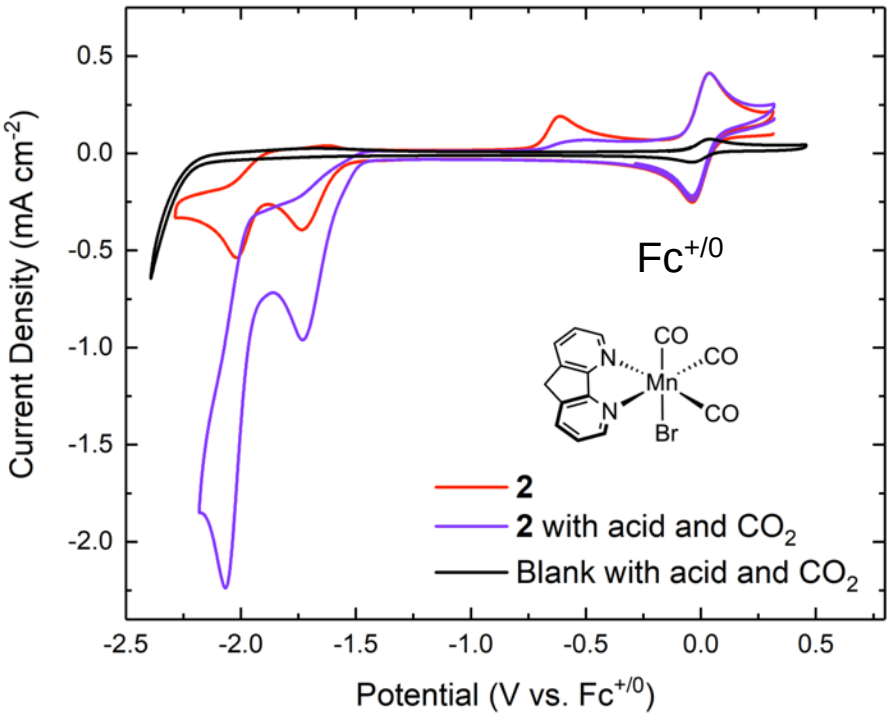

Figure S36: Cyclic voltammetry of **2** (red) and in the presence of a 5% H_2O solution and a CO_2 atmosphere (purple). The black trace illustrates a blank in the presence of a 5% H_2O solution and a CO_2 atmosphere.

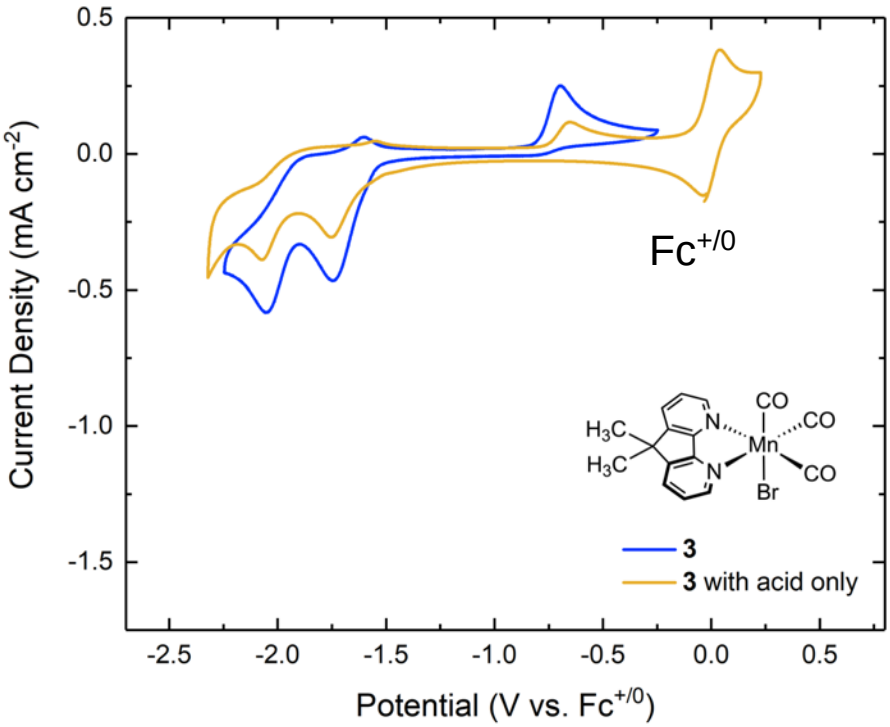

Figure S37: Cyclic voltammetry of **3** (blue) in 0.1M $TBAPF_6$/MeCN solution followed by the addition of a 5% H_2O solution (yellow). The diminished current density is a result of dilution.

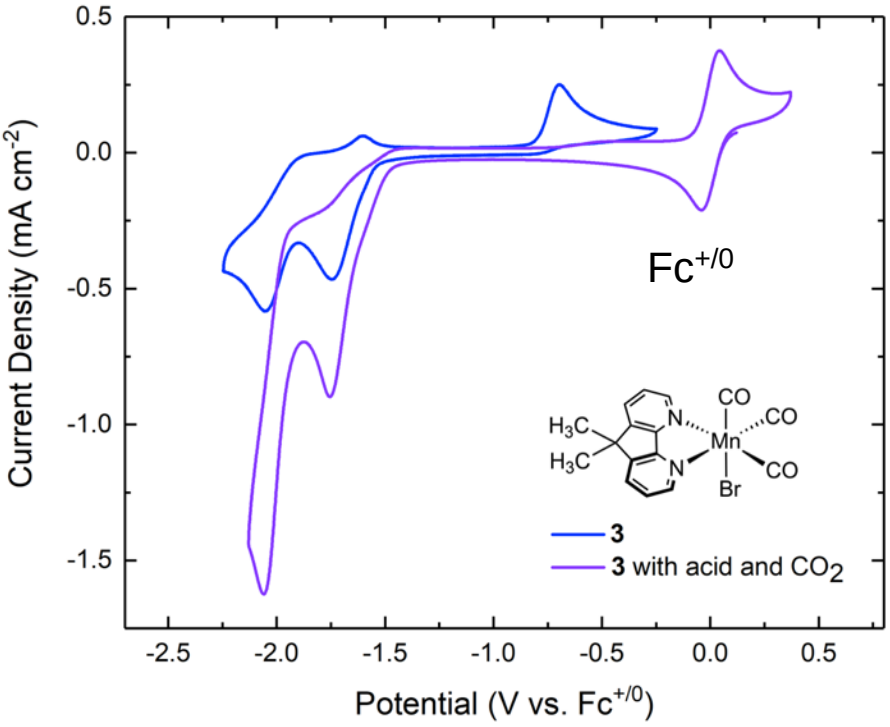

Figure S38: Cyclic voltammetry of **3** (blue) in the presence of a 5% H_2O solution and a CO_2 atmosphere (purple).

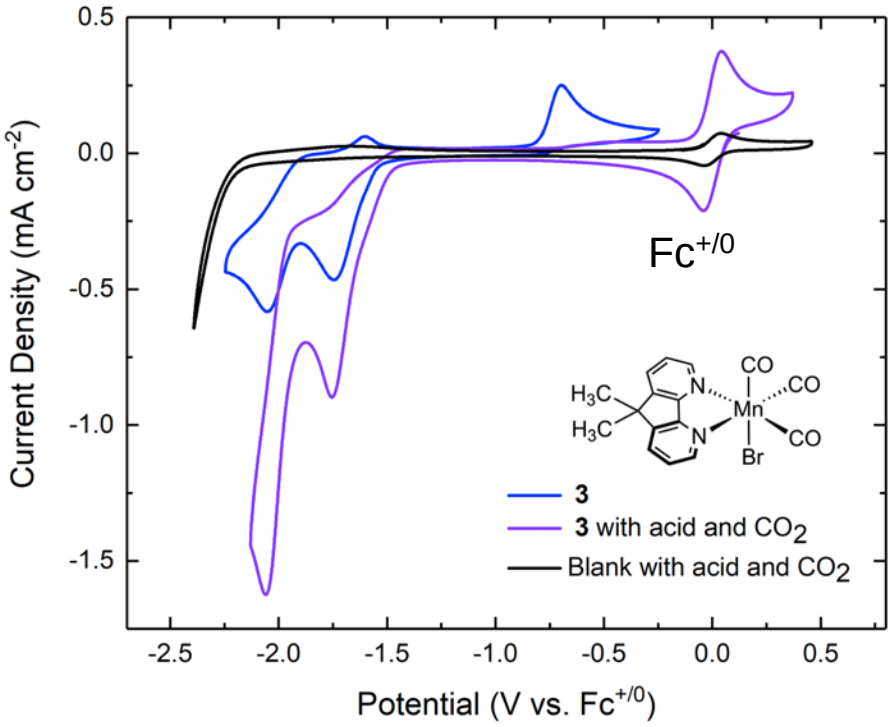

Figure S39: Cyclic voltammetry of **3** (blue) and in the presence of a 5% H_2O solution and a CO_2 atmosphere (purple). The black trace illustrates a blank in the presence of a 5% H_2O solution and a CO_2 atmosphere.

Bulk Electrolysis Data

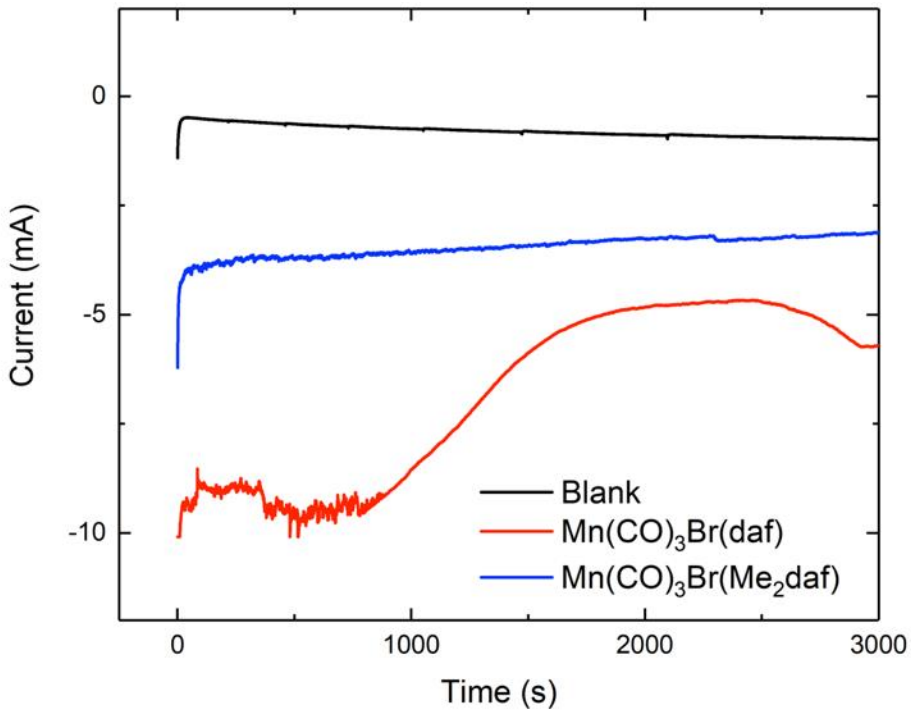

Figure S40: Chronoamperograms demonstrating current passed as a function of time for complexes **2**, **3**, and a **blank** polarized at –2.05 V vs $Fc^{+/0}$ in the presence of a 5% H_2O solution and a CO_2 atmosphere in 0.1M $TBAPF_6$/MeCN electrolyte.

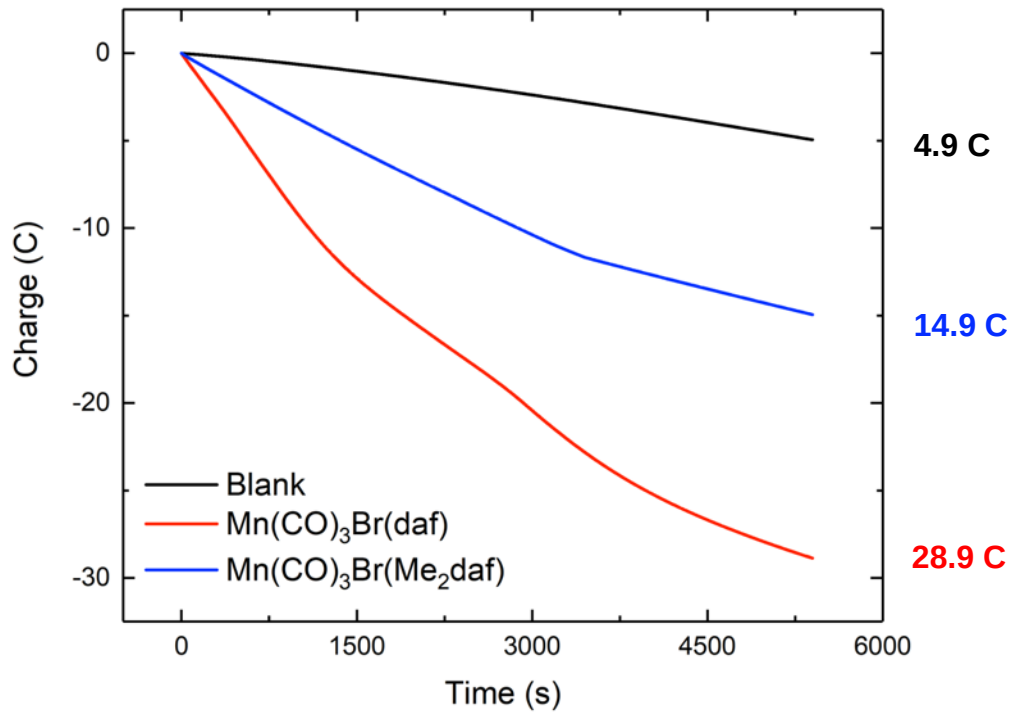

Figure S41: Charge passed as a function of time for complexes **2**, **3**, and a **blank** polarized at –2.05 V vs $Fc^{+/0}$ in the presence of a 5% H_2O solution and a CO_2 atmosphere in 0.1M $TBAPF_6$/MeCN electrolyte.

Complex	H_2 yield (ppm)	CO yield (ppm)	Faradaic efficiency for H_2 (%)	Faradaic efficiency for CO (%)	Faradaic Efficiency Total (%)	TON H_2	TON CO
Blank	1882	271	—	—	—	—	—
2	190	8271	1	27	28	0.02	0.82
3	137	5484	1	34	35	0.02	0.62

Table S1: Yield and Faradaic efficiencies for complexes **2** and **3** following a 90 minute controlled potential electrolysis polarized at -2.05 V vs. $Fc^{+/0}$ in in the presence of a 5% H_2O solution and a CO_2 atmosphere in 0.1M $TBAPF_6$/MeCN electrolyte. Water serves as the proton source and Fc is used as the sacrificial reductant.

Crystallographic Information

Refinement Details

X-ray Crystallographic Studies for (2, q51h), (3, q72j), (5, v74e), and (5, q36k).

Crystals of **2**, **3**, **5 (v74e)**, and **5 (q36k)** were mounted with Paratone N oil in MiteGen nylon loops under a cold nitrogen stream and placed on a Bruker Proteum diffractometer equipped with two CCD detectors (Apex II and Platinum 135) sharing a common MicroStar microfocus Cu rotating anode generator running at 45 mA and 60 kV (Cu Kα = 1.54178 A). Complete sets of low temperature (200 K) x-ray diffraction data were obtained for all three compounds using monochromated Cu radiation with the Apex II detector (**2**, **3, 5(q36k)**) positioned at 50.0 mm and equipped with Helios high brilliance multilayer mirror optics or the Platinum 135 detector (**5(v74e)**) positioned at 80.0 mm and equipped with Helios high- brilliance multilayer mirror optics. Totals of 7281 (**2**), 1958 (**3**), 2217 (**5(v74e**)), and 2291 (**5(q36k)**) 1.0°-wide ω- or ϕ-scan frames were collected with counting times of 5-8 seconds (**2**), 10-60 seconds (**3)** 8-30 seconds (**5(v74e)**), and 4-6 seconds (**5(q36k)**). Preliminary lattice constants were obtained with SMART in the Bruker Apex2 Software Suite. [1] Integrated reflection intensities for all three compounds were produced using SAINT in the Bruker Apex2 Software Suite.[1] Each data set was corrected empirically for variable absorption effects with SADABS[2] using equivalent reflections. The Bruker software package SHELXTL was used to solve each structure using intrinsic direct methods phasing. Final stages of weighted full-matrix least-squares refinement were conducted using Fo^2 data with SHELXTL[3] or the Olex software package equipped with XL [4]. The relevant crystallographic and structure refinement data for all three structures compounds are given in Table S-1.

The final structural model for each structure incorporated anisotropic thermal parameters for all full-occupancy nonhydrogen atoms. The final structural model for each structure incorporated anisotropic thermal parameters for all full-occupancy nonhydrogen atoms. Isotropic thermal parameters were used for all included hydrogen atoms as well as disordered partial-occupancy carbonyl atoms O1′ and C1′ in **3**. Nonmethyl hydrogen atoms were fixed at idealized riding model sp^2- or sp^3-hybridized positions with C-H bond lengths of 0.95 – 0.99 Å. Both methyl groups for the ligands in **3** were incorporated into the structural model as fixed sp^3-hybridized riding-model rigid groups with one methyl hydrogen in the crystallographic mirror plane and C-H bond lengths of 0.96 Å. The six methyl groups in the ligands of **5(v74e)** were refined as idealized riding model rigid rotors (with a C-H bond length of 0.98 Å) that were allowed to rotate freely about their C-C bonds in least-squares refinement cycles.

Table S2: Crystal Refinement Data

	2 (q51h)	**3 (q72j)**
CCDC accession code	1977431	1994285
Empirical formula	$C_{14}H_8BrMnN_2O_3$	$C_{16}H_{12}BrMnN_2O_3$
Formula weight	387.07	415.13
Temperature	200(2) K	200(2) K
Wavelength	1.54178 Å	1.54178 Å
Crystal system	Triclinic	Orthorhombic
Space group	$P\bar{1}$ - C_i^1 (No. 2)	Cmca - D_{2h}^{18} (No. 64)
a	7.1682(7) Å	11.2628(5) Å
b	10.0797(10) Å	19.4283(13) Å
c	10.5015(7) Å	15.0920(10) Å
a	77.757(6)°	90°
β	73.507(5)°	90°
γ	75.228(6)°	90°
Volume	695.47(11) $Å^3$	3302.4(3) $Å^3$
Z	2	8
Density (calculated)	1.848 g/cm^3	1.670g/cm^3
Absorption coefficient	11.193 mm^{-1}	9.473 mm^{-1}
F(000)	380	1648
Crystal size	0.04 x 0.04 x 0.04 mm^3	0.085 x 0.065 x 0.010 mm^3
Number of data frames/time	7281/5-8 seconds	1958/10-60 seconds
Theta range	4.44 to 70.32°	4.55 to 70.39°

Index ranges	$-8 \leq h \leq 8$, $-12 \leq k \leq 11$, $-12 \leq l \leq 11$	$-12 \leq h \leq 13$, $-23 \leq k \leq 20$, $-18 \leq l \leq 18$
Reflections collected	17866	10636
Independent reflections	2484 [$R_{int} = 0.035$]	1635 [$R_{int} = 0.073$]
Completeness/θ_{max}	99.2%/66.00°	99.9%/66.00°
Absorption correction	Multi-scan	Multi-scan
Max. and min. transmission	1.000 and 0.811	1.000 and 0.659
Refinement method	Full-matrix least-squares on F^2	Full-matrix least-squares on F^2
Data / restraints / parameters	2484 / 0 /190	1635 / 9 / 128
Goodness-of-fit on F^2	1.105	1.181
Final R indices [$I>2\sigma(I)$]	$R_1 = 0.030$, $wR_2 = 0.081$	$R_1 = 0.070$, $wR_2 = 0.179$
R indices (all data)	$R_1 = 0.032$, $wR_2 = 0.082$	$R_1 = 0.083$, $wR_2 = 0.187$
Largest diff. peak and hole	0.86 and -0.34 $e^-/Å^3$	1.13 and -1.01 $e^-/Å^3$

	5 (v74e)	5(q36k)
CCDC accession code	1982214	#####
Empirical formula	$C_{42.}41H_{36}F_{12}N_6O_4P_2Ru$	$C_{45}H_{45}F_{12}N_9O_{0.5}P_2Ru$
Formula weight	1084.70	1110.91
Temperature	200(2) K	200(2) K
Wavelength	1.54178 Å	1.54178 Å
Crystal system	Monoclinic	Monoclinic
Space group	$P2_1$ - C_2^2 (No. 4)	$P2_1$ - C_2^2 (No. 4)
a	11.7917(10) Å	11.7769(5) Å
b	19.7081(14) Å	19.6256(8) Å
c	12.3211(11) Å	12.3972(5) Å
a	90°	90°
β	110.665(5)°	110.8508(17)°
γ	90°	90°
Volume	2697.1(4) $Å^3$	2677.70(19) $Å^3$
Z	2	2
Density (calculated)	1.345 g/cm^3	1.398 g/cm^3
Absorption coefficient	3.682 mm^{-1}	3.661 mm^{-1}
F(000)	1093	1128
Crystal size	0.540 x 0.097 x 0.060 mm^3	0.204 x 0.051 x 0.027 mm^3
Number of data frames/time	2217/8-30 seconds	2291/4-6 seconds
Theta range	4.44 to 68.72°	3.82 to 70.23°
Index ranges	$-13\leq h\leq 13$, $-16\leq k\leq 23$, $-14\leq l\leq 14$	$-14\leq h\leq 13$, $-21\leq k\leq 23$, $-14\leq l\leq 14$
Reflections collected	17556	19973
Independent reflections	7199 [R_{int} = 0.069]	7988 [R_{int} = 0.053]
Completeness/θ_{max}	99.0%/66.00°	99.5%/66.00°

Absorption correction	Multi-scan	Numerical face-indexed
Max. and min. transmission	1.000 and 0.500	0.823 and 0.265
Refinement method	Full-matrix least-squares on F^2	Full-matrix least-squares on F^2
Data / restraints / parameters	7199 / 43 / 640	7988 / 1 / 641
Goodness-of-fit on F^2	1.057	1.072
Final R indices [I>2σ(I)]	$R_1 = 0.112$, $wR_2 = 0.294$	$R_1 = 0.053$, $wR_2 = 0.141$
R indices (all data)	$R_1 = 0.125$, $wR_2 = 0.309$	$R_1 = 0.055$, $wR_2 = 0.143$
Largest diff. peak and hole	1.84 and -1.05 $e^-/Å^3$	1.18 and -0.95 $e^-/Å^3$

Special Refinement Details for 2.

No special refinement was required

Full Solid-state Structure of 2.

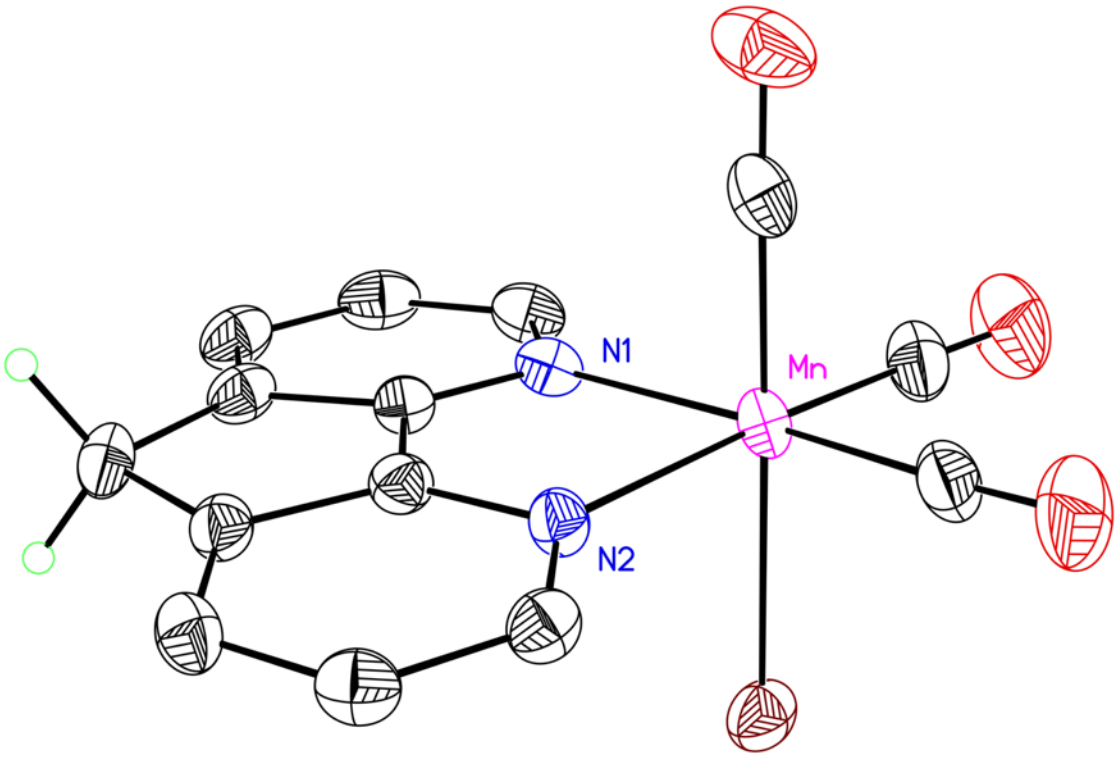

Figure S42: Full solid-state structure of **2**. Hydrogen atoms are omitted for clarity except on the methylene backbone. Displacement ellipsoids shown at the 50% probability level.

Special Refinement Details for 3.

Since Br and trans-coordinated CO ligands bonded to Mn have similar sizes and shapes, it is not surprising that the C_s- $Mn(CO)_3(N_2C_{13}H_{12})Br$ molecule (**3**) might pack in a disordered fashion with the Br and trans-coordinated CO ligands interchanged 31% of the time. This disorder necessitated mild bond length and angle restraints for this disordered group of atoms. The Mn-Br, Mn-Br′, Mn-O1, Mn-O1′, Mn-C1, Mn-C1′, C1-O1, C1′-O1′and C2-O2 bond lengths in **3** were all mildly restrained to have values which were appropriate multiples of the Mn-Br bond length that was included as a free variable in the least-squares refinement and refined to a final value of 2.406(7)Å. When the isotropic thermal parameter for C1′ refined to an unrealistically high value, it was fixed at a value equal to the average of Mn and O1′.

Solid-state Structure of 3.

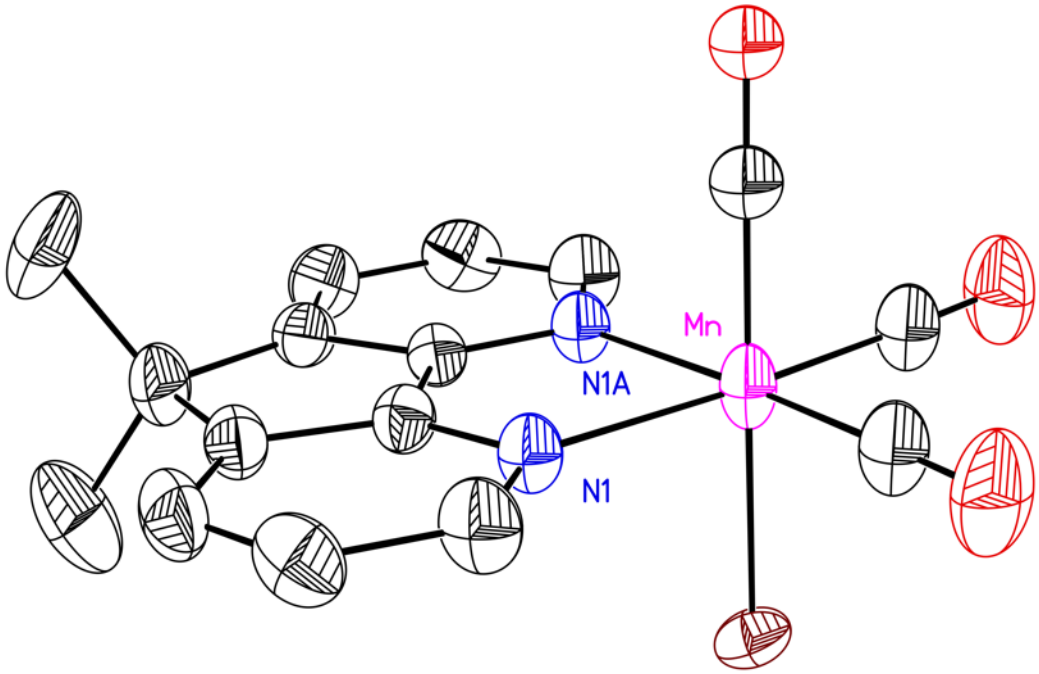

Figure S43: Solid-state structure of **3**. Hydrogen atoms, a second molecule of **3** is omitted for clarity. Displacement ellipsoids shown at the 50% probability level.

Full Solid-state Structure of 3.

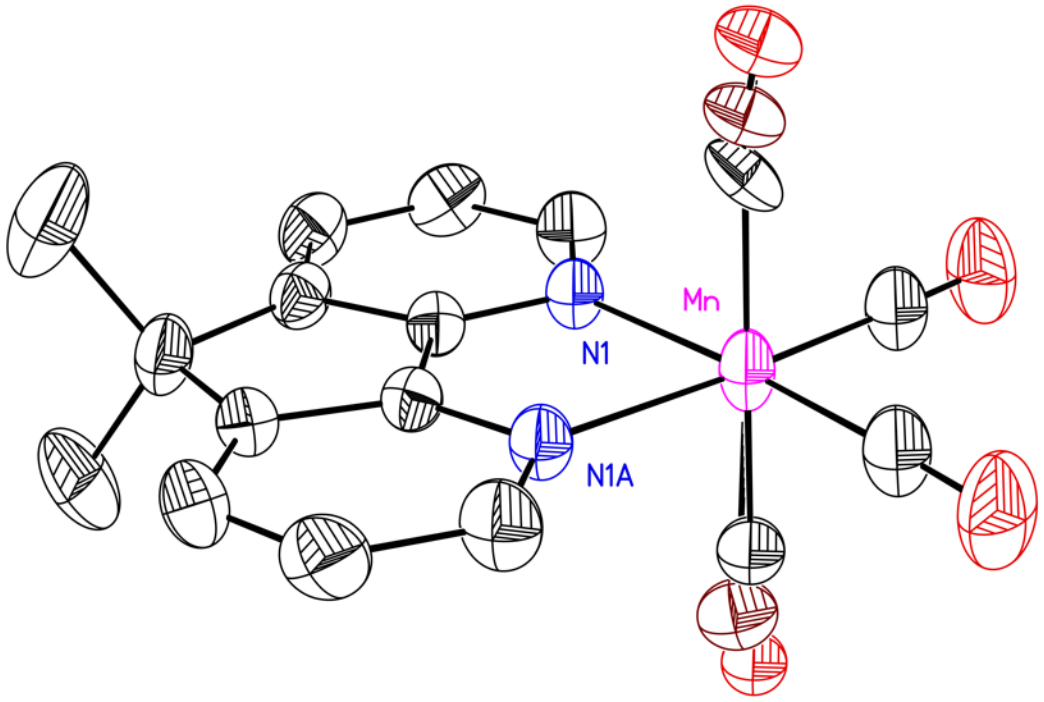

Figure S44: Full solid-state structure of **3**. Hydrogen atoms are omitted for clarity. Displacement ellipsoids shown at the 50% probability level.

Special Refinement Details for 5(v74e).

The solvent molecules of crystallization in **5(v74e)** are disordered and hydrogen atoms were not included for them in the structural model. A methanol molecule (atoms O3S and C4S) is present 41% of the time and a nearby water molecule (oxygen O1W) is present the remaining 59% of the time. A second water molecule is 77/23 disordered over two closely-spaced sites (oxygen atoms O2W and O2W'). We note explicitly here that no rigorous H-bonding scheme could be detected for these solvent molecules of crystallization, and thus the structural details of the solvent molecules of crystallization remain elusive. However, these details do not impact the assignment and structural details associated with the $[Ru(Me_2daf)_3]^{2+}$ core.

The structure of **5(v74e)** was refined as a 52/48 racemic twin.

Solid-state Structure of 5(v74e).

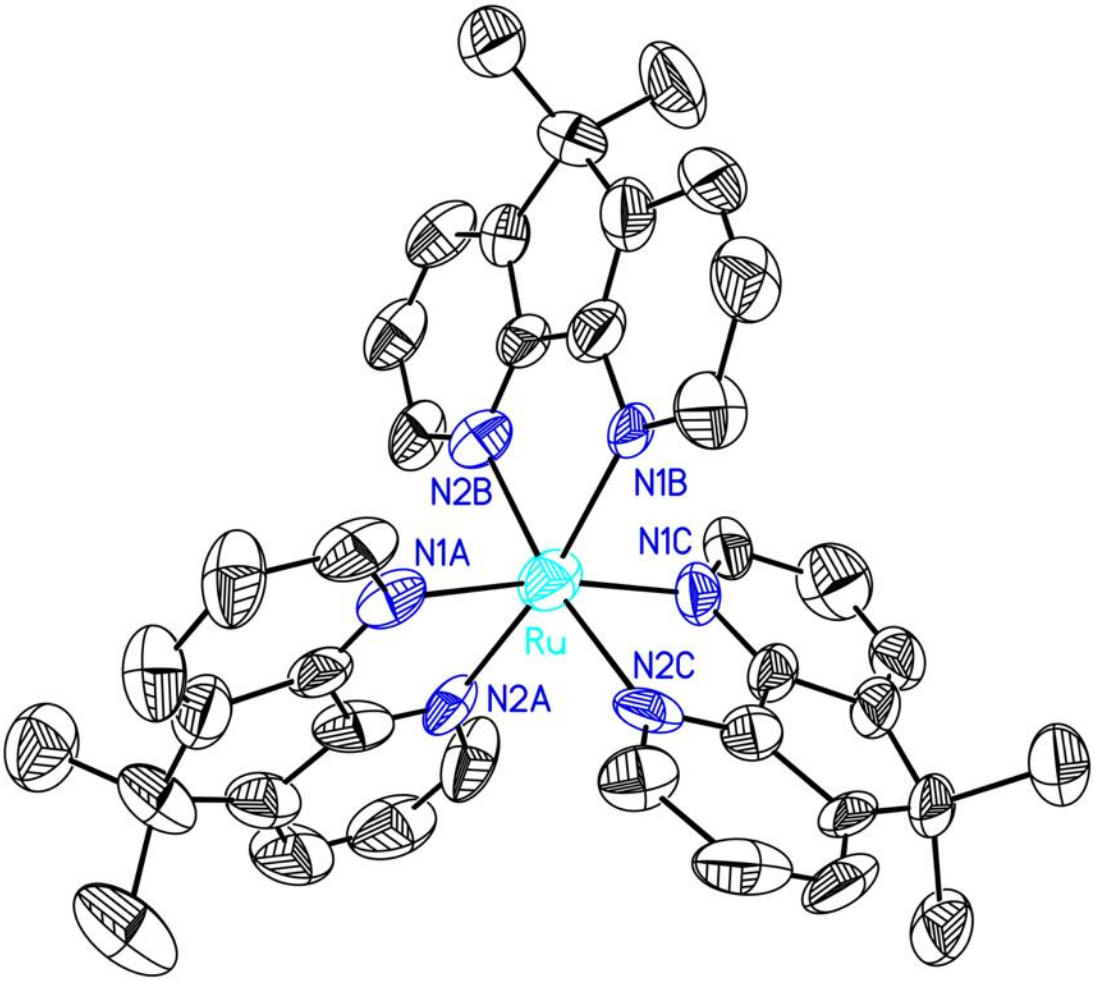

Figure S45: Solid-state structure of **5(v74e)**. Hydrogen atoms and co-crystalized water, methanol, and ethanol are omitted for clarity. Displacement ellipsoids shown at the 50% probability level.

Full Solid-state Structure of 5(v74e).

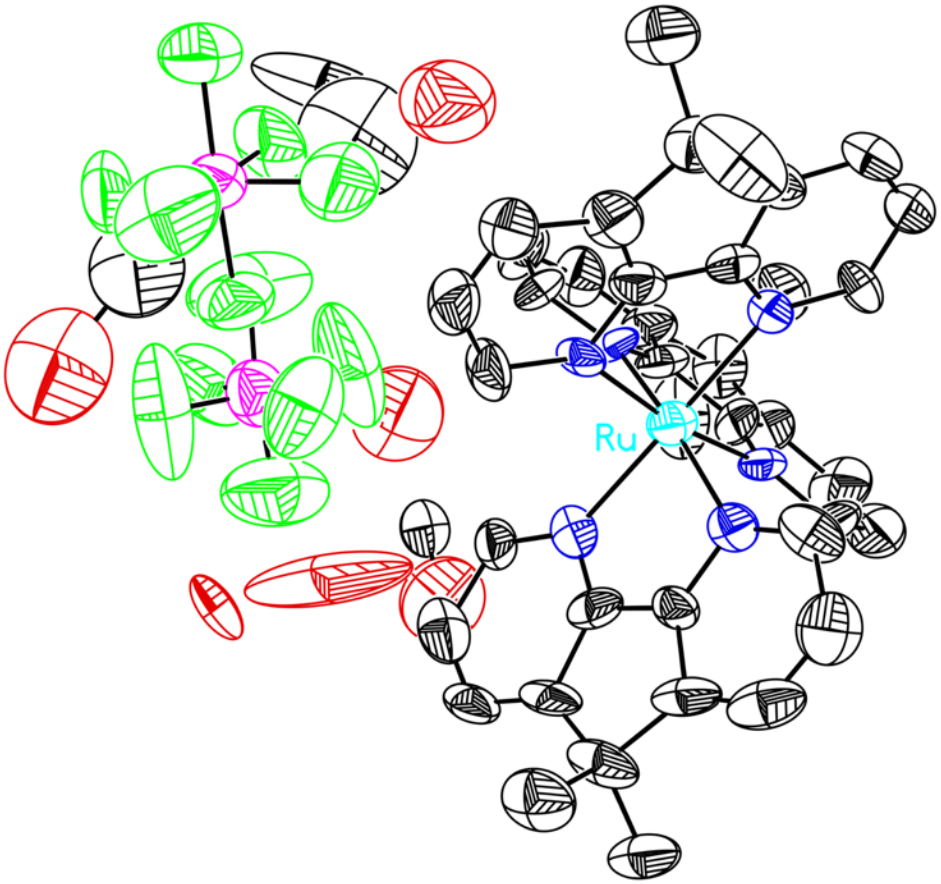

Figure S46: Full solid-state structure of **5(v74e)**. Hydrogen atoms omitted for clarity. Displacement ellipsoids shown at the 50% probability level. Atoms attributable to co-crystalized water, methanol, and ethanol are present.

Special Refinement Details for 5(q36k).

No special refinement was required

Solid-state Structure of 5(q36k).

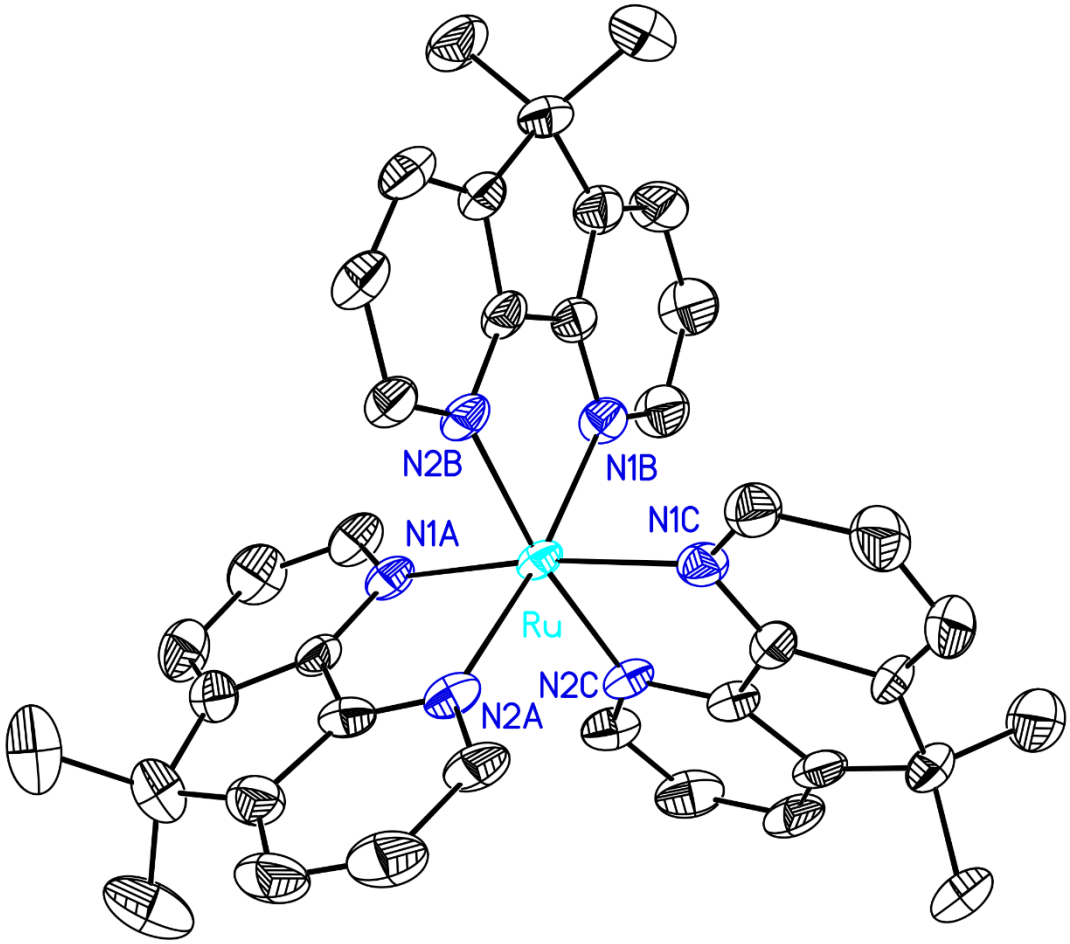

Figure S47: Solid-state structure of **5(q36k)**. Displacement ellipsoids shown at the 50% probability level. Hydrogen atoms, atoms attributable to three co-crystalized acetonitrile molecules, and a water molecule are omitted for clarity.

Full Solid-state Structure of 5(q36k).

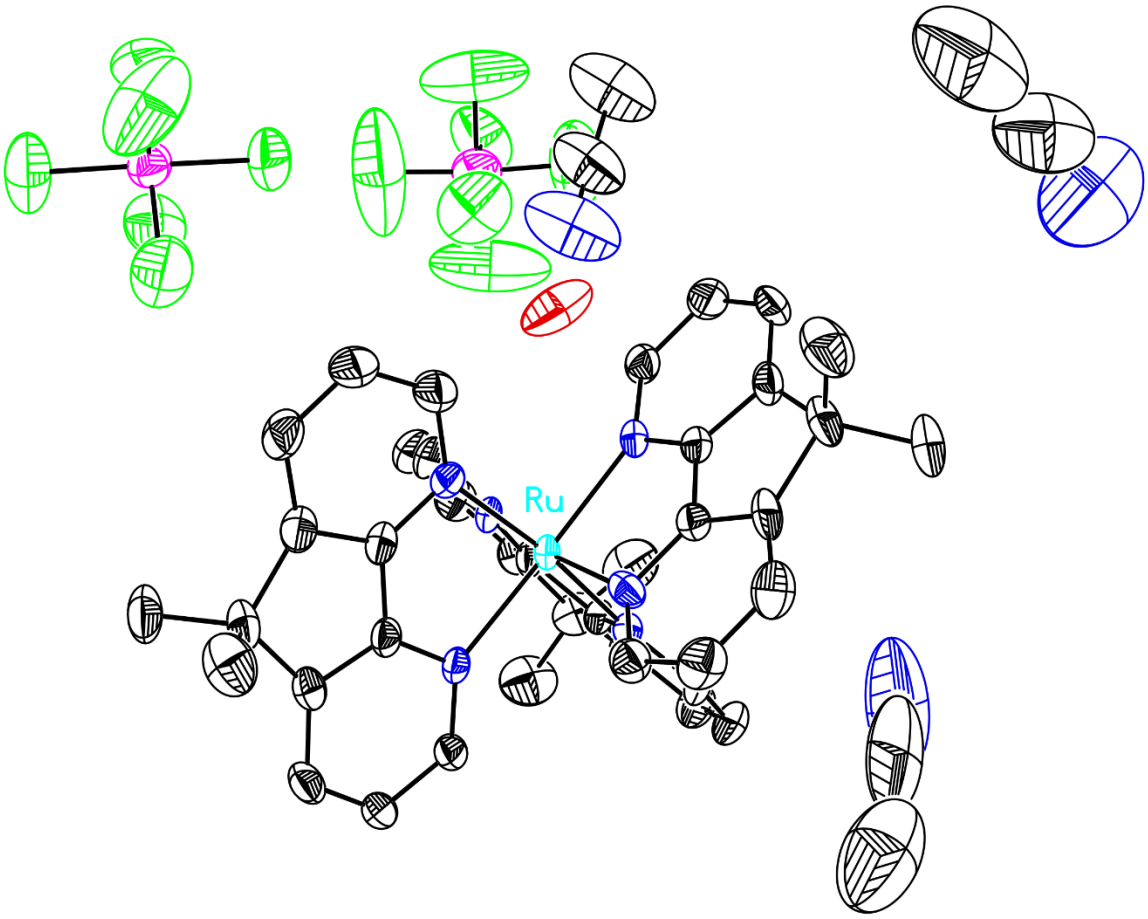

Figure S48: Full solid-state structure of **5(q36k)**. Hydrogen atoms omitted for clarity. Displacement ellipsoids shown at the 50% probability level. Atoms attributable to three co-crystalized acetonitrile molecules and a water molecule are also present.

Table S3: Selected bond lengths.

Bond Lengths	5(v74e)	5(q36k)
Ru–N	2.090(14)	2.104(5)
	2.143(15)	2.108(5)
	2.150(14)	2.114(6)
	2.154(14)	2.123(6)
	2.158(12)	2.125(5)
	2.159(15)	2.130(5)
Ru–N (avg.)	**2.142(34)**	**2.117(13)**
C5-C6	1.39(2)	1.416(9)
	1.40(3)	1.420(9)
	1.43(2)	1.425(9)
C5-C6 (avg.)	**1.41(4)**	**1.420(16)**

Table S4: Selected bond angles.

Bond Angles	5(v74e)	5(q36k)
N–Ru–N	79.5(5)	82.2(2)
	81.7(5)	83.1(2)
	82.1(6)	83.3(2)
N–Ru–N (avg.)	**81.1(9)**	**82.9(3)**
CH_3–C–CH_3	108(2)	109.4(7)
	112(2)	109.9(7)
	109.5(17)	111.9(8)
CH_3–C–CH_3 (avg.)	**110(3)**	**110.4(13)**

Characterization of Bn_3daf

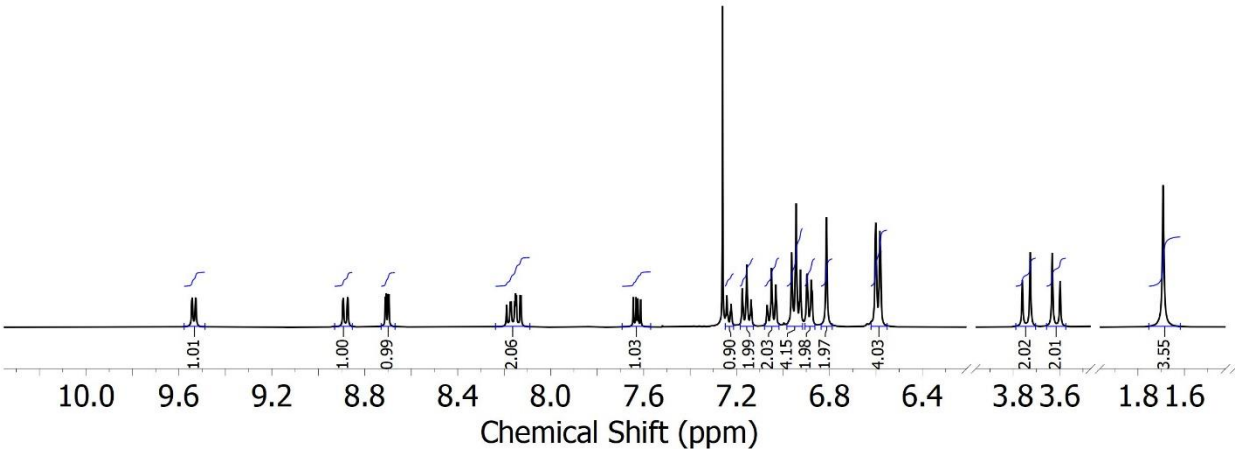

Figure S49: ^{1}H-NMR spectrum (400 MHz, $CDCl_3$) of **Bn_3daf**.

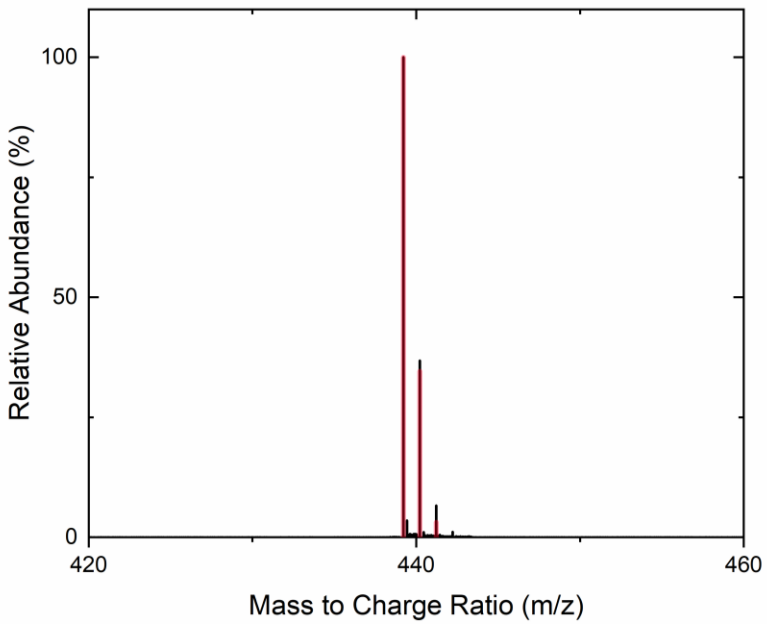

Figure S50: ESI-mass spectrum of **Bn$_3$daf**. The experimental data is shown in black and the predicted data is shown in red. The expected parent peak represents **Bn$_3$daf** –Br.

Special Refinement Details for Bn$_3$daf

All hydrogen atoms were located in a difference Fourier and initially refined as independent isotropic atoms in least-squares refinement cycles. Hydrogen atoms H17, H29, H31 and H32 were placed at idealized positions in the final refinement cycles with isotropic thermal parameters fixed at 1.2 times the equivalent isotropic thermal parameter of the carbon atom to which they are covalently bonded.

Full Solid-State Structure of Bn_3daf

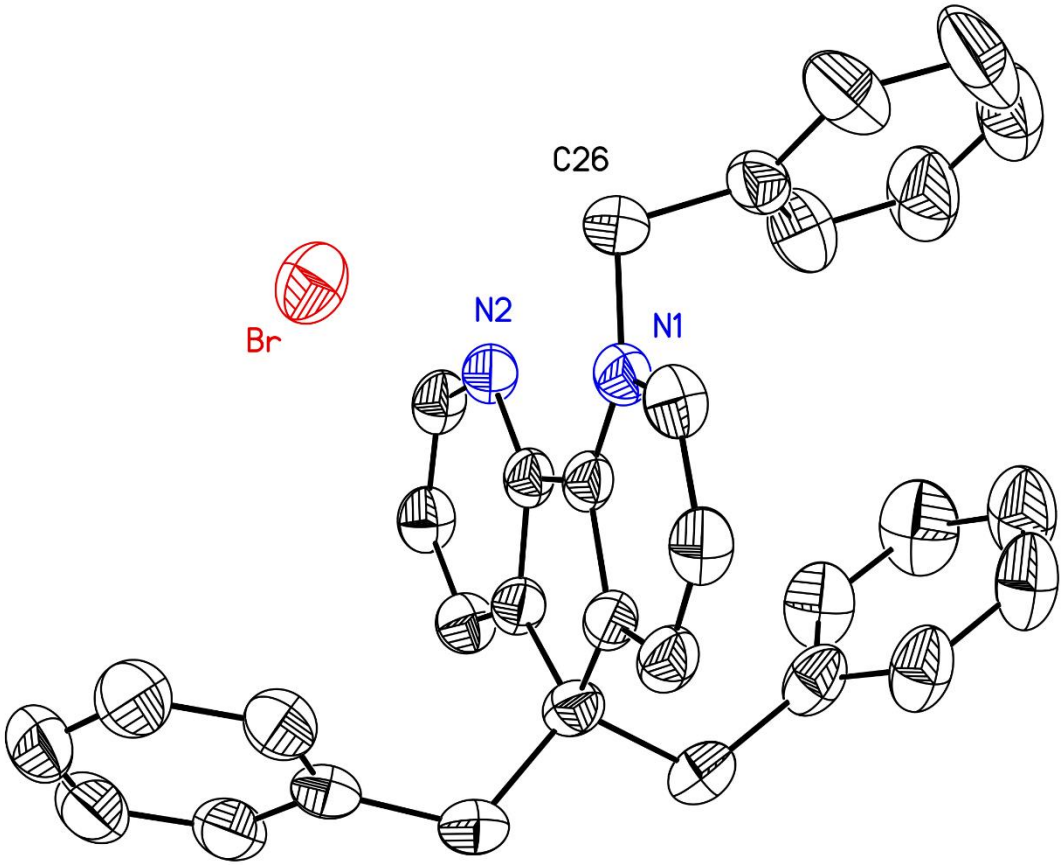

Figure S51: Full solid-state structure of the **Bn_3daf** asymmetric unit. Hydrogen atoms are omitted for clarity. Displacement ellipsoids are shown at the 50% probability level.

Appendix 2

Synthetic Procedures

*Synthesis of [Cp*Rh(mcbpy)Cl]PF_6*

To a suspension of $[Cp^*RhCl_2]_2$ (0.077 g, 0.125 mmol) in dichloromethane and acetonitrile was added $AgPF_6$ (0.063 g, 0.251 mmol). After 15 minutes the solution was filtered and mcbpy (0.050 g, 0.263 mmol) was added to the filtrate. The solution was allowed to stir for 2 hours. The volume was then reduced to ca. 5 mL and diethyl ether (ca. 15 mL) was added, leading to precipitation of an orange solid which was collected by filtration (0.135 g, 88% yield). ^{1}H NMR (400 MHz, CD_3CN) δ 8.89 (d, $^3J_{H,H}$ = 5.5 Hz, 1H), 8.77 (d, $^3J_{H,H}$ = 6.0 Hz, 1H), 8.47 (d, $^3J_{H,H}$ = 2.2 Hz, 1H), 8.38 (d, $^3J_{H,H}$ = 8.1 Hz, 1H), 8.24 (td, $^3J_{H,H}$ = 7.9 Hz, $^4J_{H,H}$ = 1.5 Hz, 1H), 7.84 (dq, $^3J_{H,H}$ = 6.2 Hz, $^4J_{H,H}$ = 2.9 Hz, 2H), 1.66 (s, 15H) ppm. ESI-MS (positive) *m/z*: expected: 463.0215; found: 463.0198 (mcbpy – PF_6^-). Anal. Calcd. for $RhC_{20}H_{22}N_2Cl_2PF_6$: C, 39.43; H, 3.64; N, 4.60. Found: C, 39.44; H, 3.81; N, 4.81.

*Synthesis of [Cp*Rh(mnbpy)Cl]PF_6*

To a suspension of $[Cp^*RhCl_2]_2$ (0.073 g, 0.118 mmol) in dichloromethane and acetonitrile was added $AgPF_6$ (0.060 g, 0.237 mmol). After 15 minutes the solution was filtered and mnbpy (0.050 g, 0.249 mmol) was added to the filtrate. The solution was allowed to stir for 2 hours. The volume was then reduced to ca. 5 mL and diethyl ether (ca. 15 mL) was added, leading to precipitation of a yellow solid which was collected by suction

filtration (0.129 g, 88% yield). ^{1}H NMR (400 MHz, CD_3CN) δ 9.15 (d, $^{3}J_{H,H}$ = 6.1 Hz, 1H), 9.02 (d, $^{3}J_{H,H}$ = 2.4 Hz, 1H), 8.92 (d, $^{3}J_{H,H}$ = 5.5 Hz, 1H), 8.60 (d, $^{3}J_{H,H}$ = 8.1 Hz, 1H), 8.41 (dd, $^{3}J_{H,H}$ = 6.1 Hz, $^{4}J_{H,H}$ = 2.4 Hz, 1H), 8.30 (td, $^{3}J_{H,H}$ = 7.9 Hz, $^{4}J_{H,H}$ = 1.5 Hz, 1H), 7.89 (ddd, $^{3}J_{H,H}$ = 7.5 Hz, $^{3}J_{H,H}$ = 5.6 Hz, $^{4}J_{H,H}$ = 1.3 Hz, 1H), 1.68 (s, 15H) ppm. ESI-MS (positive) *m/z*: expected: 474.0456; found: 474.0473 (mnbpy – PF_6^-). Anal. Calcd. for $RhC_{20}H_{22}N_3O_2ClPF_6 + H_2O$: C, 37.67; H, 3.79; N, 6.59. Found: C, 38.05; H, 3.79; N, 6.57.

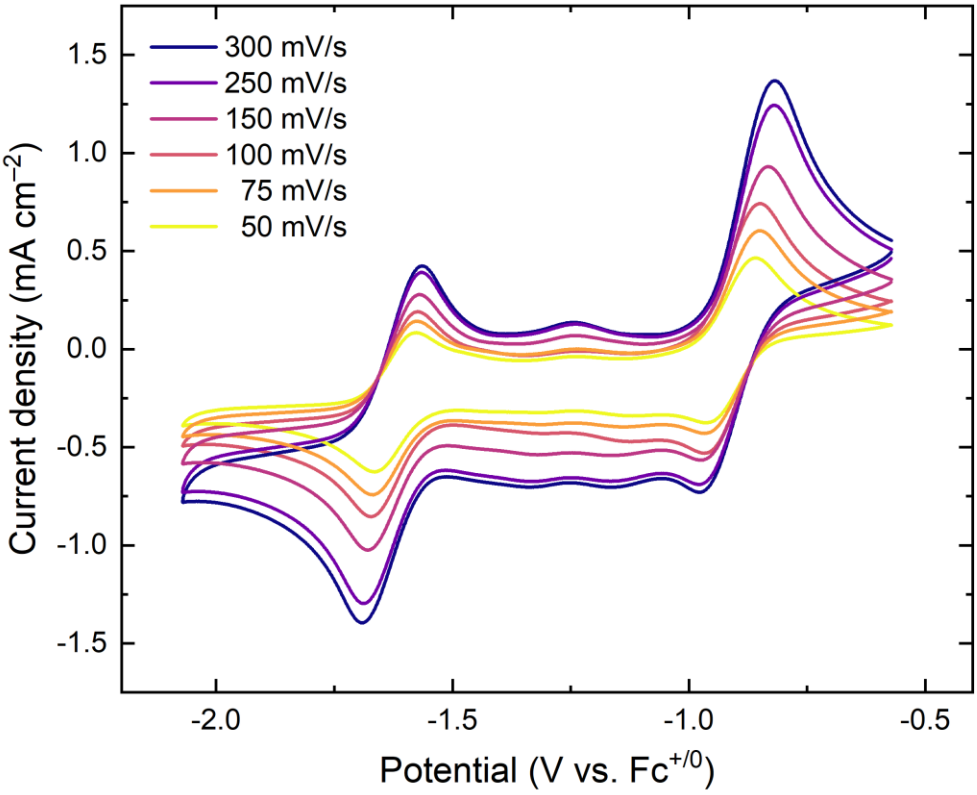

Figure S1. Scan rate dependence study of **Rh(mnbpy)**.

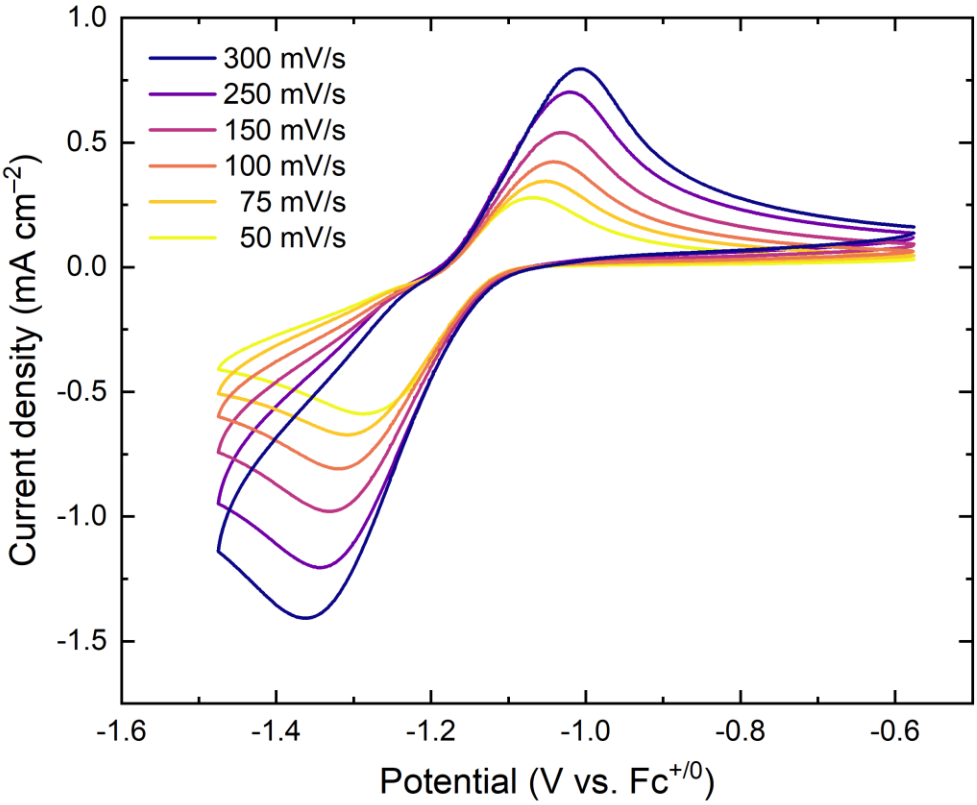

Figure S2. Scan rate dependence study of **Rh(mcbpy)**.

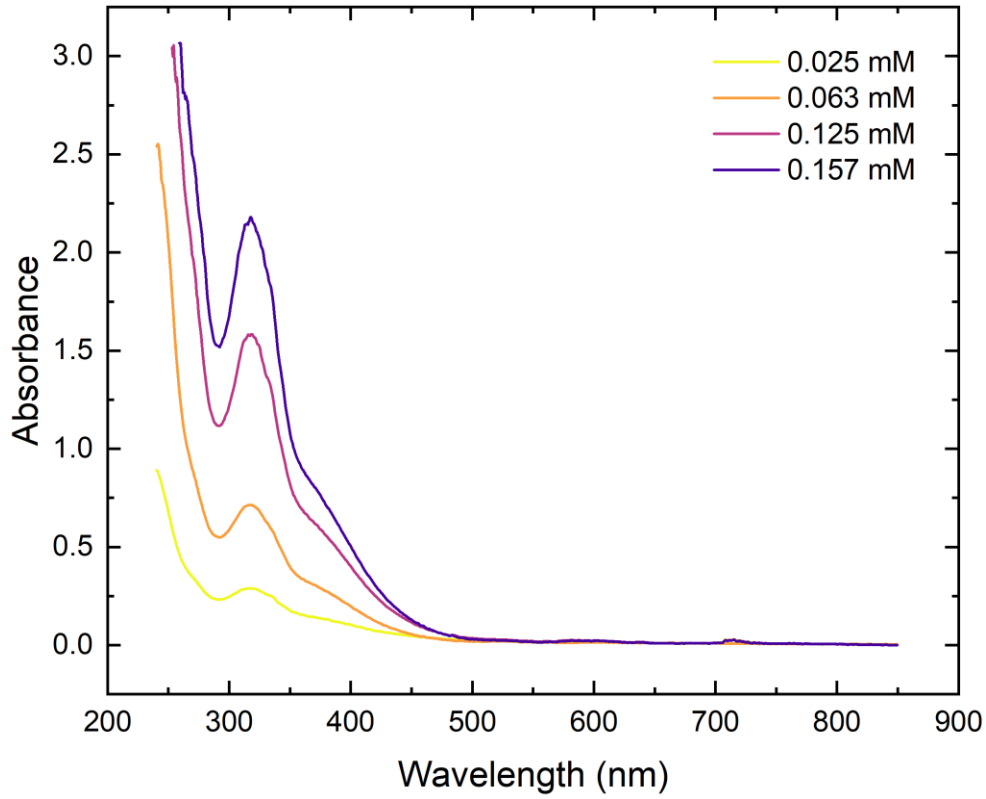

Figure S3. Concentration dependent absorbance study of **Rh(mnbpy)**.

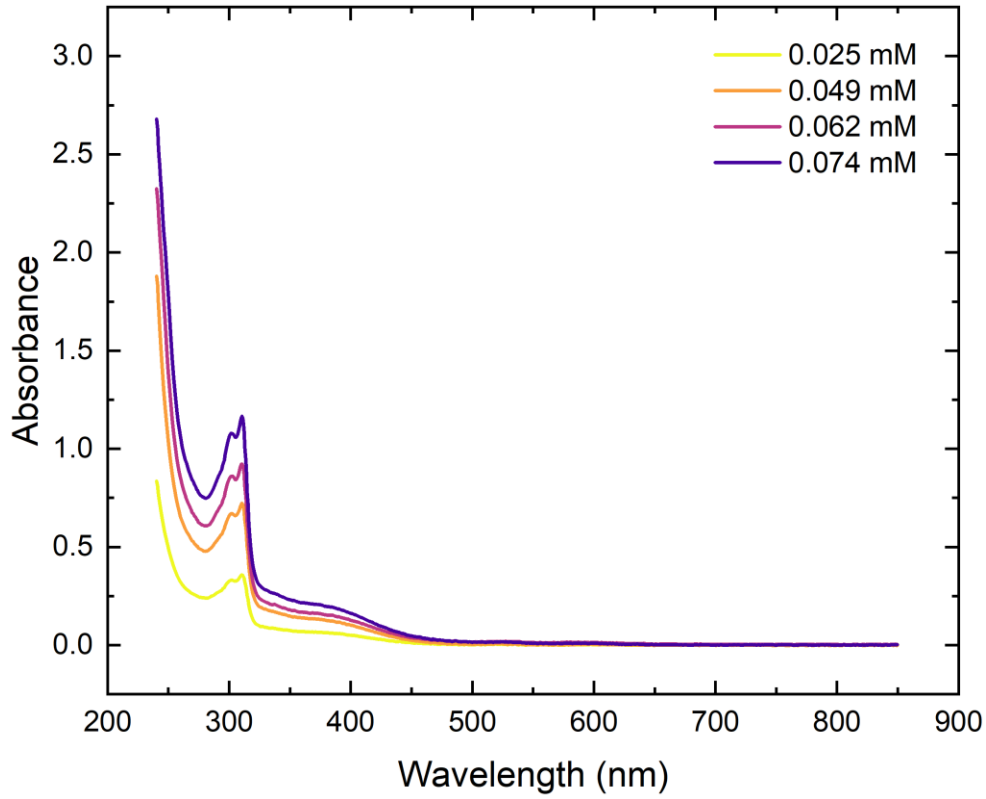

Figure S4. Concentration dependent absorbance study of **Rh(mcbpy)**.

References

1. Jackson, R. B.; Le Quéré, C.; Andrew, R. M.; Canadell, J. G.; Korsbakken, J. I.; Liu, Z.; Peters, G. P.; Zheng, B., Global energy growth is outpacing decarbonization. *Environ. Res. Lett.* **2018,** 13, 120401.

2. Peters, G. P.; Andrew, R. M.; Canadell, J. G.; Friedlingstein, P.; Jackson, R. B.; Korsbakken, J. I.; Le Quéré, C.; Peregon, A., Carbon dioxide emissions continue to grow amidst slowly emerging climate policies. *Nat. Clim. Change* **2020,** 10, 3-6.

3. Appel, A. M.; Bercaw, J. E.; Bocarsly, A. B.; Dobbek, H.; DuBois, D. L.; Dupuis, M.; Ferry, J. G.; Fujita, E.; Hille, R.; Kenis, P. J. A.; Kerfeld, C. A.; Morris, R. H.; Peden, C. H. F.; Portis, A. R.; Ragsdale, S. W.; Rauchfuss, T. B.; Reek, J. N. H.; Seefeldt, L. C.; Thauer, R. K.; Waldrop, G. L., Frontiers, Opportunities, and Challenges in Biochemical and Chemical Catalysis of CO2 Fixation. *Chem. Rev.* **2013,** 113, 6621-6658.

4. English, A. M.; DeLaive, P. J.; Gray, H. B.; Lum, V. R., Metalloprotein electron-transfer mechanisms. Quenching of electronically excited tris(2,2'-bipyridine)ruthenium(II) by reduced blue copper proteins. *J. Am. Chem. Soc.* **1982,** *104*, 870-871.

5. Brunschwig, B. S.; DeLaive, P. J.; English, A. M.; Goldberg, M.; Gray, H. B.; Mayo, S. L.; Sutin, N., Kinetics and mechanisms of electron transfer between blue copper proteins and electronically excited chromium and ruthenium polypyridine complexes. *Inorg. Chem.* **1985,** *24*, 3743-3749.

6. Sullivan, B. P.; Bolinger, C. M.; Conrad, D.; Vining, W. J.; Meyer, T. J., One- and two-electron pathways in the electrocatalytic reduction of CO_2 by fac-Re(bpy)$(CO)_3$Cl (bpy = 2,2´-bipyridine). *J. the Chem. Soc., Chem. Commun.* **1985**, 1414-1416.

7. Bourrez, M.; Molton, F.; Chardon-Noblat, S.; Deronzier, A., [Mn(bipyridyl)$(CO)_3$Br]: An abundant metal carbonyl complex as efficient electrocatalyst for CO2 reduction. *Angew. Chem. Int. Ed.* **2011,** *50*, 9903-9906.

8. Meyer, T. J., Electron Transfer Reactions Induced by Excited State Quenching. *Isr. J. Chem.* **1976,** *15*, 200-205.

9. Moyer, B. A.; Meyer, T. J., Properties of the oxo/aqua system $(bpy)_2(py)RuO^{2+}$/$(bpy)_2(py)Ru(OH_2)^{2+}$. *Inorg. Chem.* **1981,** *20*, 436-444.

10. Imayoshi, R.; Tanaka, H.; Matsuo, Y.; Yuki, M.; Nakajima, K.; Yoshizawa, K.; Nishibayashi, Y., Cobalt-catalyzed transformation of molecular dinitrogen into silylamine under ambient reaction conditions. *Chem–Eur. J.* **2015,** *21*, 8905-8909.

11. Henke, W. C.; Otolski, C. J.; Moore, W. N. G.; Elles, C. G.; Blakemore, J. D., Ultrafast spectroscopy of [Mn$(CO)_3$] complexes: tuning the kinetics of light-driven CO release and solvent binding. *Inorg. Chem.* **2020**, *59*, 2178-2187.

12. Henke, W. C.; Lionetti, D.; Moore, W. N. G.; Hopkins, J. A.; Day, V. W.; Blakemore, J. D., Ligand substituents govern the efficiency and mechanistic path of hydrogen production with [Cp*Rh] catalysts. *ChemSusChem* **2017,** *10*, 4589-4598.

13. Clark, M. L.; Cheung, P. L.; Lessio, M.; Carter, E. A.; Kubiak, C. P., Kinetic and mechanistic effects of bipyridine (bpy) substituent, labile ligand, and brønsted acid on electrocatalytic CO_2 reduction by Re(bpy) complexes. *ACS Catal.* **2018,** *8*, 2021-2029.

14. Tignor, S. E.; Kuo, H.-Y.; Lee, T. S.; Scholes, G. D.; Bocarsly, A. B., Manganese-based catalysts with varying ligand substituents for the electrochemical reduction of CO_2 to CO. *Organometallics* **2019,** *38*, 1292-1299.

15. Henderson, L. J.; Fronczek, F. R.; Cherry, W. R., Selective perturbation of ligand field excited states in polypyridine ruthenium(II) complexes *J. Am. Chem. Soc.* **1984,** *106*, 5876-5879.

16. Yam, V. W.-W.; Wang, K.-Z.; Wang, C.-R.; Yang, Y.; Cheung, K.-K., Synthesis, Characterization, and Second-Harmonic Generation Studies of Surfactant Rhenium(I) Diimine Complexes in Langmuir−Blodgett Films. X-ray Crystal Structure of fac-$ClRe(CO)_3L$ (L = 9-Heptylamino-4,5-diazafluorene). *Organometallics* **1998,** *17*, 2440-2446.

17. Sykora, M.; Kincaid, J. R., Synthetic Manipulation of Excited State Decay Pathways in a Series of Ruthenium(II) Complexes Containing Bipyrazine and Substituted Bipyridine Ligands. *Inorg. Chem.* **1995,** *34*, 5852-5856.

18. Annibale, V. T.; Song, D., Coordination chemistry and applications of versatile 4,5-diazafluorene derivatives. *Dalton Trans.* **2016,** *45*, 32-49.

19. Jiang, H.; Song, D., Syntheses, characterizations, and reactivities of 4,5-diazafluorenide complexes of palladium(II) and rhodium(I). *Organometallics* **2008,** *27*, 3587-3592.

20. Jiang, H.; Stepowska, E.; Song, D., Syntheses, structures and reactivities of rhodium 4,5-diazafluorene derivatives. *Eur. J. Inorg. Chem.* **2009,** 2083-2089.

21. Stepowska, E.; Jiang, H.; Song, D., Reversible H2 splitting between Ru(II) and a remote carbanion in a zwitterionic compound. *Chem. Commun.* **2010,** *46*, 556-558.

22. Annibale, V. T.; Batcup, R.; Bai, T.; Hughes, S. J.; Song, D., RuCp* Complexes of ambidentate 4,5-diazafluorene derivatives: from linkage isomers to coordination-driven self-assembly. *Organometallics* **2013,** *32*, 6511-6521.

23. Batcup, R.; Chiu, F. S. N.; Annibale, V. T.; Huh, J.-e. U.; Tan, R.; Song, D., Selective one-pot syntheses of Pt II Cu I heterobimetallic complexes of 4,5-diazafluorenide derivatives. *Dalton Trans.* **2013,** *42*, 16343-16350.

24. Campbell, A. N.; White, P. B.; Guzei, I. A.; Stahl, S. S., Allylic C−H acetoxylation with a 4,5-diazafluorenone-ligated palladium catalyst: a ligand-based strategy to achieve aerobic catalytic turnover. *J. Am. Chem. Soc.* **2010,** *132*, 15116-15119.

25. Campbell, A. N.; Meyer, E. B.; Stahl, S. S., Regiocontrolled aerobic oxidative coupling of indoles and benzene using Pd catalysts with 4,5-diazafluorene ligands. *Chem. Commun.* **2011,** *47*, 10257-10259.

26. White, P. B.; Jaworski, J. N.; Fry, C. G.; Dolinar, B. S.; Guzei, I. A.; Stahl, S. S., Structurally diverse diazafluorene-ligated palladium(II) complexes and their implications for aerobic oxidation reactions. *J. Am. Chem. Soc.* **2016,** *138*, 4869-4880.

27. Elsevier, C. J., Catalytic and stoichiometric C–C bond formation employing palladium compounds with nitrogen ligands. *Coord. Chem. Rev.* **1999,** *185-186*, 809-822.

28. Baran, M. F.; Durap, F.; Aydemir, M.; Baysal, A., Transfer hydrogenation of aryl ketones with homogeneous ruthenium catalysts containing diazafluorene ligands. *Appl. Organomet. Chem.* **2016,** *30*, 1030-1035.

29. Klein, R. A.; Witte, P.; van Belzen, R.; Fraanje, J.; Goubitz, K.; Numan, M.; Schenk, H.; Ernsting, J. M.; Elsevier, C. J., Monodentate and bridging coordination of 3,3′-Annelated 2,2′-Bipyridines in zerovalent palladium- and platinum-p-quinone complexes. *Eur. J. Inorg. Chem.* **1998,** *1998*, 319-330.

30. Druey, J.; Schmidt, P., Phenanthrolinchinone und diazafluorene. *Helv. Chim. Acta* **1950,** *33*, 1080-1087.

31. H. Ohrui, A. Senoo, K. Tetsuya, U.S. Pat. Appl. 0161574, **2008**.

32. Luong, J. C.; Faltynek, R. A.; Wrighton, M. S. Ground- and excited-state oxidation-reduction chemistry of (triphenyltin)- and (triphenylgermanium)tricarbonyl(1,10-phenanthroline)rhenium and related compounds. *J. Am. Chem. Soc.* **1980**, 102, 7892−7900.

33. Caspar, J. V.; Meyer, T. J. Application of the energy gap law to nonradiative, excited-state decay. *J. Phys. Chem.* **1983**, 87, 952−957.

34. Miguel, D.; Riera, V. Synthesis of manganese(I) carbonyls with σ-bonded alkynyl ligands. *J. Organomet. Chem.* **1985**, 293, 379−390.

35. H. Günther, NMR spectroscopy, John Wiley & Sons, New York, **1980**.

36. Türschmann, P.; Colell, J.; Theis, T.; Blümich, B.; Appelt, S., Analysis of parahydrogen polarized spin system in low magnetic fields. *Phys. Chem. Chem. Phys.* **2014,** *16*, 15411-15421.

37. Meyer, T.J., *Pure Appl. Chem.*, **1986**, *58*, 1193-1206.

38. Kalyanasundaram, K., Photophysics, photochemistry and solar energy conversion with tris(bipyridyl)ruthenium(II) and its analogues. *Coord. Chem. Rev.* **1982,** *46*, 159-244.

39. Witte, P. T.; Klein, R.; Kooijman, H.; Spek, A. L.; Polášek, M.; Varga, V.; Mach, K., Electron transfer in the reactions of titanocene-bis(trimethylsilyl) acetylene complexes with 2,2'-bipyridine and 4,5-diazafluorene. The crystal structure of (4,5-diazafluorenyl) bis(pentamethylcyclopentadienyl) titanium(III). *J. Organomet. Chem.* **1996,** *519*, 195-204.

40. Machan, C. W.; Sampson, M. D.; Chabolla, S. A.; Dang, T.; Kubiak, C. P., Developing a mechanistic understanding of molecular electrocatalysts for CO_2 reduction using infrared spectroelectrochemistry. *Organometallics* **2014,** *33*, 4550-4559.

41. Rillema, D. P.; Jones, D. S.; Levy, H. A., Structure of tris(2,2'-bipyridyl)ruthenium(II) hexafluorophosphate, $[Ru(bipy)_3][PF_6]_2$; x-ray crystallographic determination. *J. Chem. Soc., Chem. Commun.* **1979**, 849-851.

42. Rillema, D. P.; Jones, D. S.; Woods, C.; Levy, H. A., Comparison of the crystal structures of tris heterocyclic ligand complexes of ruthenium(II). *Inorg. Chem.* **1992,** *31*, 2935-2938.

43. Breu, J.; Domel, H.; Stoll, A., Racemic compound formation versus conglomerate formation with $[M(bpy)_3](PF_6)_2$ (M = Ni, Zn, Ru); molecular and crystal structures. *Eur. J. Inorg. Chem.* **2000,** 2401-2408.

44. Fronczek, F. R., CCDC 287572: Experimental Crystal Structure Determination, 2006, DOI: 10.5517/cc9n7jp

45. Constable, E. C., Homoleptic complexes of 2,2′-bipyridine. *Adv. Inorg. Chem.*, Sykes, A. G., Ed. Academic Press: 1989; Vol. 34, pp 1-63.

46. Kaim, W., The transition metal coordination chemistry of anion radicals. *Coord. Chem. Rev.* **1987,** *76*, 187-235.

47. England, J.; Scarborough, C. C.; Weyhermüller, T.; Sproules, S.; Wieghardt, K., Electronic Structures of the Electron Transfer Series $[M(bpy)_3]_n$, $[M(tpy)_2]_n$, and $[Fe(tbpy)_3]n$ (M = Fe, Ru; n = 3+, 2+, 1+, 0, 1–): A Mössbauer Spectroscopic and DFT Study. *Eur. J. Inorg. Chem.* **2012,** 4605-4621.

48. Lyaskovskyy, V.; de Bruin, B., Redox non-Innocent ligands: versatile new tools to control catalytic reactions. *ACS Catal.* **2012,** *2*, 270-279.

49. Corcos, A. R.; Villanueva, O.; Walroth, R. C.; Sharma, S. K.; Bacsa, J.; Lancaster, K. M.; MacBeth, C. E.; Berry, J. F., Oxygen activation by Co(II) and a redox non-innocent ligand: spectroscopic characterization of a radical–Co(II)–superoxide complex with divergent catalytic reactivity. *J. Am. Chem. Soc.* **2016,** *138*, 1796-1799.

50. Riplinger, C.; Sampson, M. D.; Ritzmann, A. M.; Kubiak, C. P.; Carter, E. A., Mechanistic contrasts between manganese and rhenium bipyridine electrocatalysts for the reduction of carbon dioxide. *J. Am. Chem. Soc.* **2014,** *136*, 16285-16298.

51. Grice, K. A.; Nganga, J. K.; Naing, M. D.; Angeles-Boza, A. M., 1.04 - Bipyridine Ligands. In *Comprehensive Coordination Chemistry III*, Constable, E. C.; Parkin, G.; Que Jr, L., Eds. Elsevier: Oxford, 2021; pp 60-77.

52. Boyd, E. A.; Lionetti, D.; Henke, W. C.; Day, V. W.; Blakemore, J. D., Preparation, Characterization, and Electrochemical Activation of a Model [Cp*Rh] Hydride. *Inorg. Chem.* **2019,** 58, 3606-3615.

53. Kodama, K.; Kobayashi, A.; Hirose, T., Synthesis and spectral properties of ruthenium(II) complexes based on 2,2′-bipyridines modified by a perylene chromophore. *Tetrahedron Lett.* **2013,** 54, 5514-5517.

54. Mizuno, T.; Takeuchi, M.; Hamachi, I.; Nakashima, K.; Shinkai, S., A boronic acid–diol interaction is useful for chiroselective transcription of the sugar structure to the Δ- versus Λ-$[Co^{III}(bpy)_3]^{3+}$ ratio. *J. Chem. Soc., Perkin Trans. 2* **1998**, 2281-2288.

55. Schwartz, K. R.; Chitta, R.; Bohnsack, J. N.; Ceckanowicz, D. J.; Miró, P.; Cramer, C. J.; Mann, K. R., Effect of Axially Projected Oligothiophene Pendants and Nitro-Functionalized Diimine Ligands on the Lowest Excited State in Cationic Ir(III) bis-Cyclometalates. *Inorg. Chem.* **2012,** 51, 5082-5094.

56. Baron, A.; Herrero, C.; Quaranta, A.; Charlot, M.-F.; Leibl, W.; Vauzeilles, B.; Aukauloo, A., Efficient electron transfer through a triazole link in ruthenium(II) polypyridine type complexes. *Chem. Commun.* **2011,** 47, 11011-11013.

57. Lionetti, D.; Day, V. W.; Lassalle-Kaiser, B.; Blakemore, J. D., Multiple binding modes of an unconjugated bis(pyridine) ligand stabilize low-valent [Cp*Rh] complexes. *Chem. Commun.* **2018,** 54, 1694-1697.

58. White, C.; Yates, A.; Maitlis, P. M.; Heinekey, D. M., (η^5-Pentamethylcyclopentadienyl) Rhodium and -Iridium Compounds. In *Inorganic Syntheses*, 1992; pp 228-234.

59. Mantell, M. A.; Kampf, J. W.; Sanford, M., Improved Synthesis of $[Cp^RRhCl_2]_2$ Complexes. *Organometallics* **2018,** 37, 3240-3242.

60. Zhang, J.; Tian, B.; Wang, L.; Xing, M.; Lei, J., Syntheses and Applications of Silver Halide-Based Photocatalysts. In *Photocatalysis: Fundamentals, Materials and Applications*, Zhang, J.; Tian, B.; Wang, L.; Xing, M.; Lei, J., Eds. Springer Singapore: Singapore, 2018; pp 307-343.

61. Henke, W. C.; Lionetti, D.; Moore, W. N. G.; Hopkins, J. A.; Day, V. W.; Blakemore, J. D., Ligand Substituents Govern the Efficiency and Mechanistic Path of Hydrogen Production with [Cp*Rh] Catalysts. *ChemSusChem* **2017,** 10, 4589-4598.

62. Moore, W. N. G.; Henke, W. C.; Lionetti, D.; Day, V. W.; Blakemore, J. D., Single-Electron Redox Chemistry on the [Cp*Rh] Platform Enabled by a Nitrated Bipyridyl Ligand. *Molecules* **2018,** 23, 2857.

63. Scharwitz, M. A.; Ott, I.; Geldmacher, Y.; Gust, R.; Sheldrick, W. S., Cytotoxic half-sandwich rhodium(III) complexes: Polypyridyl ligand influence on their DNA binding properties and cellular uptake. *J. Organomet. Chem.* **2008,** 693, 2299-2309.